The Pennsylvania State University

The Graduate School

MICRO-WIRELESS POWER TRANSFER WITH APPLICATIONS TO THE NON-METALLIC CONNECTOR

A Thesis in

Electrical Engineering

by

Joshua Benjestorf

Submitted in Partial Fulfillment

of the Requirements

for the Degree of

Master of Science

August 2021

The thesis of Joshua Benjestorf was reviewed and approved by the following:

Aldo W. Morales
Professor of Electrical Engineering
IEEE Senior Member
Co-Director, Center for Signal Integrity
Thesis Co-Advisor

Sedig S. Agili
Professor of Electrical Engineering
IEEE Senior Member
Co-Director, Center for Signal Integrity
Thesis Co-Adviser

Nashwa Elaraby
Associate Teaching Professor of Electrical Engineering
IEEE Senior Member

Thang Bui
Associate Director, School of Science, Engineering and Technology
Head of the Department

ABSTRACT

The concept of Wireless Power Transfer (WPT) was first introduced during Industrial Revolution by Nikola Tesla. For most of the 20th century there were very few practical applications for it. It was not until the late 1990's early 2000's when the demand for WPT systems and technology started to explode as the result of other new emerging technologies that found useful applications for it. Some of these useful applications are wireless chargers for cells phones, Apple watches, earbuds, and wireless EV chargers for cars only to name a few.

There is, however, an area that has been largely overlooked that could also greatly benefit from WPT technology and that area is the connector industry. This is an industry that faces many challenges with exposed metallic electrical contacts that physically connect two sub-systems together in the form of receptacles and plugs. These challenges with connectors are ongoing due to contacts being contaminated by environmental exposure and continuous insertion cycles. WPT systems are introduced in this thesis as potentially a way to solve these performance problems. This is done by physically reducing inductor coil sizes for connector receptacles and plugs giving rise to the terms micro-Wireless Power Transfer (μWPT) and the Non-Metallic Connector (NMC).

This thesis identifies other critical performance parameters that impact power transfer efficiency that can be optimized in order to compensate for the physical reduction in inductor size and still give a practical and usable separation distance margin needed for connector applications. This thesis also identifies where on the WPT classification chart μWPT systems might fall. Extensive mathematical derivations for each of the four network topologies is presented with expressions for power transfer efficiency for each one. Comparisons are made between them and the topology best suited for μWPT is identified. An approach for how to predict the separation distance between the two inductors in a μWPT system from the simulated coupling coefficient using the Neumann formula is presented as well as the reverse approach with a measured separation distance that can accurately predict the coupling coefficient. A novel and repeatable experimental setup is also presented for taking S-parameter measurements using a VNA and obtaining distance measurements. The thesis concludes with a demonstration of a μWPT system being used in an actual NMC prototype that further validates the overall thesis proposal for a new type of connector technology.

Table of Contents

List of Figures

List of Tables

List of Abbreviations

WPT: Wireless Power Transfer

μWPT: Micro-Wireless Power Transfer

NMC: Non-Metallic Connector

USB: Universal Serial Bus

EIA: Electronic Industries Alliance

IEC: International Electrotechnical Commission

UL: Underwriter Laboratories

IEEE: Institute for Electrical and Electronics Engineers

GEM: Global E-waste Monitor

CPT: Contactless Power Transfer

IPT: Inductive Power Transfer

IoT: Internet of Things

AI: Artificial Intelligence

SS-Topology: Series-Series-Topology

SP-Topology: Series-Parallel-Topology

PS-Topology: Parallel-Series-Topology

PP-Topology: Parallel-Parallel-Topology

ADS: Advanced Design System

S-Parameters: Scatter-Parameters

DUT: Device Under Test

VNA: Vector Network Analyzer

SMA: Sub Miniature A

PCB: Printed Circuit Board

DMM: Digital Multi Meter

Acknowledgements

This thesis would not have been possible without the inspiration of those people who defied the odds of success and kept going; that despite the public criticism and pressure of being different, they persevered and ran after their original idea with everything they had. To that end, it would not be fitting to ignore some key people that inspired this journey from the beginning. The late John Forbes Nash III whose extraordinary life story of defying all odds against him and his relentless determination to find his original idea in order to make the most impact on the world is what has inspired me to strive and do the same. It is posthumous that I dedicate this thesis to his memory.

This thesis is most of all dedicated to my mother, Paula Benjestorf. The environment she created at home growing up, her educating me in every subject at home all the way up until university, and her investment in the very early years was the source that sparked a curiosity about the natural world that would later turn into a passion for science and for a love of learning. Part of that gave rise to the will power that resulted in this thesis, and because of that, my gratitude is unending.

A special thanks goes to my academic advisors Prof. Aldo Morales and Prof. Sedig Agili whose mentorship, guidance, and teachings though the years at the University have introduced me to the unending and exciting world of science and engineering research where there exists no limit for the imagination. The many hours of discussion, debate, problem-solving and study eventually lead to the completion of this thesis, and to that I am grateful.

I would also like to acknowledge and thank Frank Johns, Principle Designer and Engineer at Non-Metallic Connectors, Inc., for his contributions in the creation of the many figures, illustrations, and diagrams within this thesis which would not be even close to the quality that they are without his skill and talent. And finally, a special thanks is extended to Vince Pascucci, Fellow at TE Connectivity and director of the failure analysis lab who is a recognized industry expert in connector reliability, for reviewing and providing much valuable feedback on Chapters 1 of this manuscript.

CHAPTER 1
Wireless Power Transfer (WPT) Systems

1.1 Introduction to WPT Systems and Applications

What is Wireless Power Transfer (WPT)? As the name implies, WPT can be defined as the transfer of power wirelessly using magnetic and/or electric fields. In literature, it has been described as a process of transferring electric power between two or more physically unconnected systems by electromagnetic induction [1] governed by Maxwell's equations. In the context of this thesis, it is defined as energy or power transferred over an air "gap" (g) from one sub-system that transmits it (Coil TX) to another receiving sub-system (Coil RX) to do something useful with the energy on the other end. This concept is illustrated in Figure 1.1.

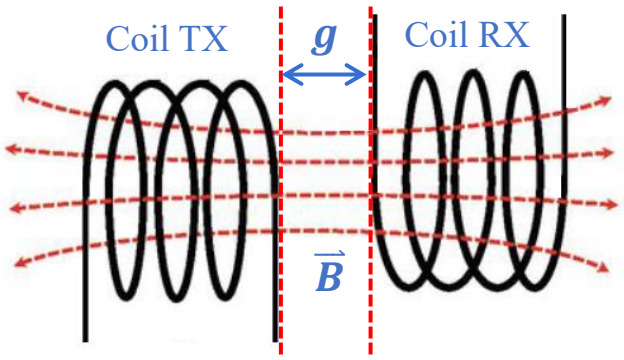

Figure 1.1: Illustration of WPT transferring energy over an air gap between two coils

In certain literature terms such as Contactless Power Transfer (CPT) or Inductive Power Transfer (IPT) have also been used interchangeably with WPT with some minor differences. The idea of wireless power came about in the mid to late 19th century when James Clerk Maxwell first combined Ampere's circuital law and Faraday's law of induction along with his groundbreaking experiments on the matter. Maxwell formulated the governing dynamics that now form the foundation of all WPT theory and applications that use it. The four foundational equations are the

Maxwell's equations (1.1)-(1.4) as they define and describe physically the nature and interactions between electric and magnetic fields. Later in the late 19th century, attempts were first made at contactless energy transfer in John Henry Poynting's presentation on mathematical models on it in 1884 followed by the discovery of radio waves by Heinrich Rudolf Hertz in 1888 where he showed that an electromagnetic wave could be sent by one coil and received by another with useful energy on the receiving end [2]. This inspired Nikola Tesla in the early 20th century in his experiments with inductive coupling which eventually gave rise to Tesla Coils. With this idea he used to wirelessly power light bulbs from a large distance.

$$\nabla \cdot \vec{\boldsymbol{E}} = \frac{\rho}{\epsilon_0} \tag{1.1}$$

$$\nabla \times \vec{\boldsymbol{E}} = -\frac{\partial \vec{\boldsymbol{B}}}{\partial t} \tag{1.2}$$

$$\nabla \cdot \vec{\boldsymbol{B}} = 0 \tag{1.3}$$

$$\nabla \times \vec{\boldsymbol{B}} = \mu_0 \vec{\boldsymbol{J}} + \mu_0 \epsilon_0 \frac{\partial \vec{\boldsymbol{E}}}{\partial t} \tag{1.4}$$

It was Tesla's dream to create a society where wireless power was ubiquitous [3], however, Tesla was limited by the technology of his time. For decades after, attempts at utilizing WPT in new applications were made, but very few of them were forthcoming that had practical use until the 1960s. WPT systems of this time still found no traction due to limited resources and very poor power transfer efficiency leading to a dead end for any commercial application. Through the years as technology advanced, better resources were created and new frontiers began opening up for WPT applications that started showing commercial potential especially as industry demand for them began to accelerate. It was not until the late 1990s and early 2000s that WPT started showing

potential at solving certain power delivery problems more effectively [4]. Figure 1.2 shows some examples of WPT applications that are systems currently on the market today.

(a) (b) (c)

Figure 1.2: iPhone charger (a), Apple watch charger (b) and wireless earbuds charger (c) [5]

Chargers for smartphones, smartwatches, earbuds, etc. are all very common in today's market. The goal is for consumer convenience and part of that convenience is not having to deal with using charging cables that would otherwise be used. As new battery technologies have emerged that have resulted in higher charge density, consumer electronics devices are now able to last longer between charge cycles. Consumer convenience also has been a driving force. Rather than plugging something in, it is much easier to simply set the device on a charging pad. Notice every one of these devices in Figure 1.2 still needs a power cable. They are all examples of what is classified as near field technology and are based off a concept of magnetic induction which applies to applications with 1/6 wavelength of the transmission frequency and apply to separation distances between $1\ cm \leq g < 2.5\ cm$, where g is the air gap between the device and the charging pad [6]. WPT applications are also extensive in the medical field and fall under this category but these along with the applications in Figure 1.2 are classified as low power applications.

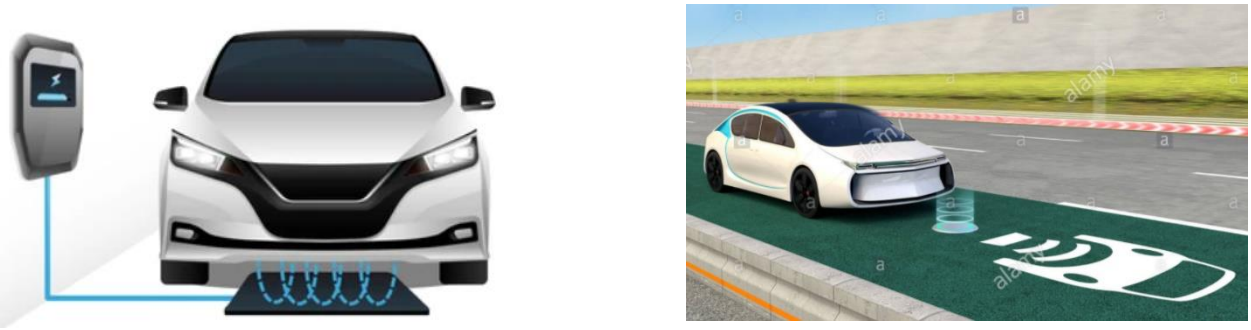

(a) (b)

Figure 1.3: High-power EV stationary charging (a) and dynamic charging (b) [7]

Higher power applications that also fall under the same category, specifically in the electric vehicle (EV) space where bi-directional inductive power transfer systems [1], [8], [9] are used as shown in Figure 1.3. Similar applications are being developed for railroads [10] and in longer distance power transfer applications – called magnetic resonance coupling – that are within a few meters distance, designed to power basic appliances [11], [12].

In the advent of new technological horizons that have revolutionized the world since the turn of the century such as social media, miniaturization and creation of smart mobile devices, sensor-based Internet of Things (IoT), AI, etc., consumer demand has continued on the trend of smaller, thinner, and faster devices. Along those lines and part of that trend has been an effort to eliminate the need to plug things in and to also eliminate the clutter that goes alone with it as demonstrated in Figures 1.2 and 1.3. Along these same lines, Figure 1.4 shows a vision of future WPT systems that is currently being developed by a spin off company at MIT called The Wireless Power or WiTricity for short. WiTricity is a method that is based on strongly coupled magnetic resonators capable of transferring large amounts of power – greater than 60W – over distances of up to 2 meters with good efficiency [13], [14], [15]. The ultimate mission and goal of WiTricity is to eliminate the need for all cables and wire connections while improving the quality of life for humanity. It is a very ambitions vision, but it is questionable on whether it is feasible. Can power

of this magnitude be transferred wirelessly at higher frequencies to every device within proximity and not pose a potential risk to human health as studies suggest that it could [16], [17]? Can such a setup as displayed in Figure 1.4 be standardized? Suffice it to say the proliferation of WiTricity will remain limited until such questions can be objectively answered. The vision and goal of WiTricity, however, would be one step closer to the realization of Nikola Tesla's dream: a world ran on wireless power. Before that could even be possible companies and OEMs across every industry would have to transition and modify their product lines in order to accommodate it.

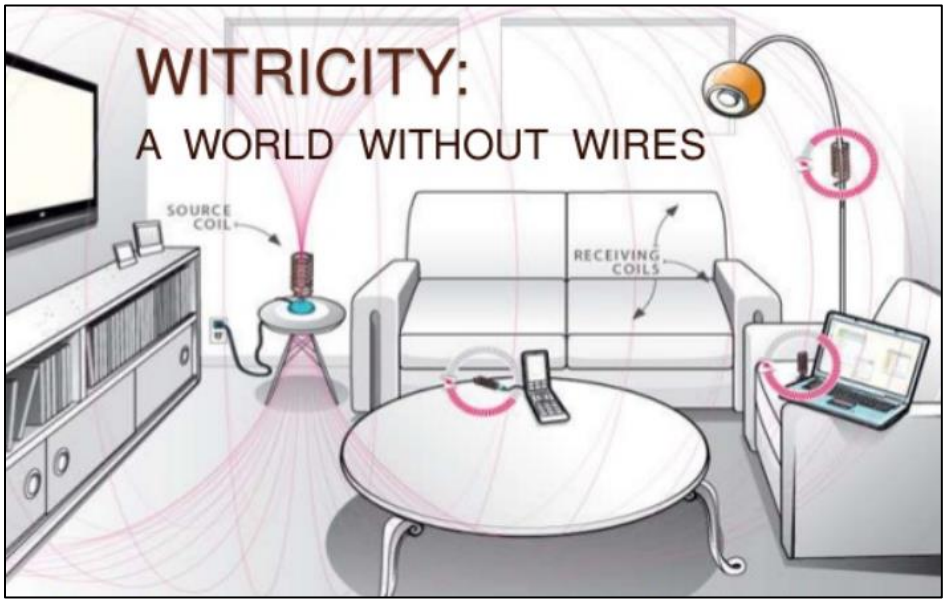

Figure 1.4: Magnetic resonance WPT supplying power to everything [18]

Indeed, since the turn of the century WPT systems have become an emerging technology that is exploding with potential as new applications for it continue to be developed. There is, however, another area that has largely been overlooked that can also greatly benefit from WPT and that area is the connector industry. This is the motivation behind this thesis which is to expand and apply the concepts of WPT to the connector industry and by doing so solve some common and ubiquitous problems that the industry continues to face.

1.2 Standard Connectors and Micro-WPT (µWPT)

How can the concepts of WPT be applied to the connector industry and what benefits can it bring to this industry? To sufficiently answer these questions, it is fitting to formally define what a connector is and describe some of the problems facing this industry.

Formally defined, a standard connector is an electromechanical system that provides a separable interface between two subsystems of an electronic system without an unacceptable effect on performance of the system [19], [20]. The two attributes about this definition is that a connector is a physical connection and an interface between electrical systems that allows them to become "separated" – similar to WPT systems described earlier. But when it is not separated and when the connector is part of an electrical circuit conducting current, the system performance must not be "unacceptable". In the connector world, electrical performance normally is measured by its contact resistance which becomes larger with time by continuous use and multiple insertion cycles. The connector must have the ability to perform many of these insertion cycles over its life such that towards the end, and when the two connector halves are inserted, the connector still has the ability to perform well electrically. What defines acceptable performance in most cases is described in detail within industry standards across multiple industries such as EIA, IEC, UL, IEEE, etc. Both mechanisms of the connector concept – separable interface and acceptable performance – ultimately fail over time; a fact that has concerned the connector industry ever since the first connectors were made.

Figure 1.5: Examples of standard connectors within multiple industries [21], [22], [23]

The connectors in Figure 1.5 are all examples of standard connectors and so when the term "connector" is used throughout the remainder of this thesis, these are examples of what is being referred to. Connectors pass signal and/or power via electric, metallic contacts, sometimes referred to in literature as "Ohmic" contacts, by utilizing conduction current. Metallic contacts normally get seated in some form of insulating housing mold – usually a plug and receptacle – and when both the plug and receptacle are inserted effectively joining the two systems together, metallic contacts form a mated pair to allow current flow between subsystems. The two electrical contacts inside the mated pair are held in place using mechanical latches either on an EMI shield or on a housing mold. Mechanical latches are critical for sustaining the necessary physical downforce needed for adequate current flow and are subjected to a spring constant that also eventually wears out over time just like the metallic contacts. Therefore, there are many factors that can contribute to an increase in electrical contact resistance over time.

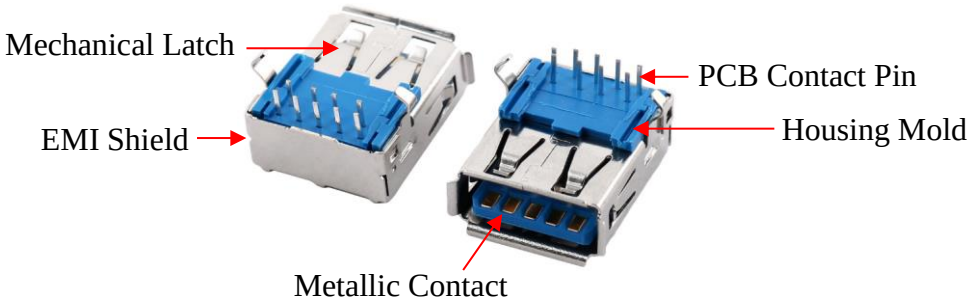

Figure 1.6: Basic Connector Parts on USB 3.0 Type-A Receptacle [24]

An illustration of the basic connector building blocks is given above in Figure 1.6 showing a front and back view of a USB 3.0 Type-A receptacle. Standard connectors today have a lot of variety, but the basic two attributes of a separable interface with good electrical performance is maintained. However, maintaining these two attributes is the ongoing challenge due to the exposure of electrical contacts. Environmental exposure of contacts has caused great pains for the industry and how to reduce the impacts of such exposure. This will briefly be discussed next.

1.2.1 Common Problems with Standard Connectors

Standard connectors face a variety of problems. Through the years there have been improvements on how to combat these problems, but these problems nonetheless still persist due to a single reason: electrical contacts that are open and exposed to the environment. Some of these problems are delamination of electrical contacts, dust particles debris buildup, chemical corrosion due to moisture and water, fatigue wear and loss of surface material just to name a few [25], [26], [27]. Some examples of these problems are illustrated in Figure 1.7.

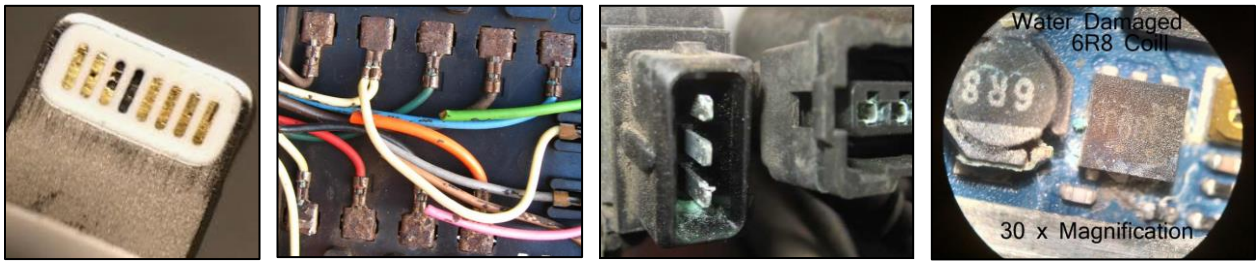

Figure 1.7: Examples of water damage and corrosion on electrical contacts

While the examples illustrated above may be examples of extreme cases, they are still problems and sources of concern for the connector industry. Even worse are the implications for the consumer electronics devices, industrial applications, solar panels, aerospace and defense systems, and automotive subsystems that all utilize standard connectors in some way. In many cases, connectors can be viewed as entry ports for moisture and/or water that further exacerbate these problems degrading electrical performance more and negatively impacting the overall connection efficiency [28] for whatever system they may be installed on.

In this thesis, it is proposed that the best way to eliminate the problems associated with standard metallic electrical contacts within connectors is to eliminate the metallic electrical contacts completely [29]. The way this can be done is by integrating the concepts of WPT theory

into them. In order to accomplish this, the inductor coils used in traditional WPT systems such as the ones illustrated in Figure 1.1 will need to be physically downsized to be small enough to fit inside connector receptacles and plugs. This is where the term micro-WPT is introduced, and when successfully applied to connectors it gives rise to a new type of connector technology that does not therefore depend on metallic electrical contacts to pass signal or power between subsystems. Thus, this new connector technology has been appropriately called the Non-Metallic Connector (NMC).

1.2.2 Practical Implementation of μWPT for Connectors

The purpose for μWPT is to apply the concepts of WPT to the connector industry. It is extremely important to understand that when the term "micro" is used to describe this concept, it is not used in the sense to describe the magnitude or intensity of power that can be transferred over an air gap separation distance. The term "micro" is used in the sense to describe the physical size of the inductors used in μWPT systems and the size of the air gap separation distance relative to traditional WPT systems that were introduced in Figures 1.2 and 1.3. When implemented into connectors, the NMC is consequently created with the intension of solving the type of connector problems briefly discussed in section 1.2.1. For power and signal, both capacitive and inductive coupling can be used. For high-speed signal transfer, optical coupling can be used. There have been attempts made by industry to utilize optical connectors for high-speed data transfer such as Corning, Inc., to take advantage of low latency in optical cables for longer cable lengths, but the interface is still a standard connector that are subject to the same performance-degrading problems mentioned earlier. In some NMC applications a hybrid model that combines two or more of these coupling methods can be created such as the NMC USB connector proposed in [30]. Most applications, however, utilize only one of these methods in efforts to simplify the manufacturing process. Figure 1.8 shows a high-level concept for an NMC based on capacitive coupling first

proposed in [31] followed by a general model for capacitive μWPT in Figure 1.9.

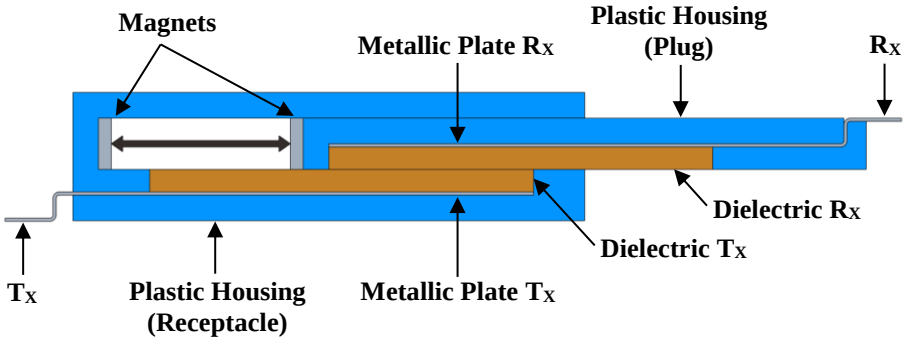

Figure 1.8: High-level model of an NMC based on capacitive coupling

An example of a practical application for NMCs utilizing capacitive coupling that show commercialization potential was presented by Wang and Sanders with an iPhone charger through a USB interface [32] that was based off the original concept presented in [20].

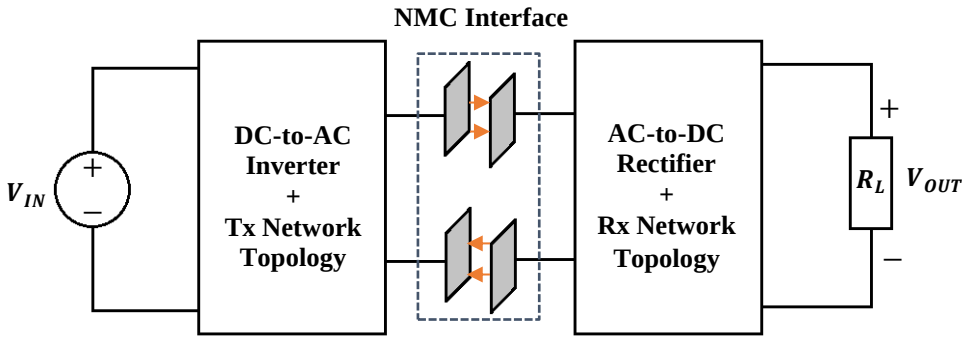

Figure 1.9: General model for capacitive μWPT for NMCs

The main drawback for capacitive-based NMCs is in manufacturing and separation distance limitations. In order to obtain capacitance values high enough that can accommodate realistic separation distances which can be defined as larger than 0.5 mm, the dielectric material needs to be relatively large. Materials such as ceramics and titanites normally have high dielectric constants above 5,000 F/m, but with that often brings other undesirable material characteristics such as piezo electric effects and unacceptable wear properties. Another drawback for capacitive-based NMCs in general is the need to continuously make physical contact between two dielectric

materials. With this comes with limitations on insertion cycles. This is the main reason why inductive coupling is currently the preferred method for NMCs: larger separation distances above 1 mm are common and the separation medium between Tx and Rx is empty space therefore giving rise to unlimited insertion cycles. Figure 1.10 shows a high-level concept for an NMC based on inductive coupling first proposed in [31] followed by a high-level model of inductive coupling in Figure 1.11.

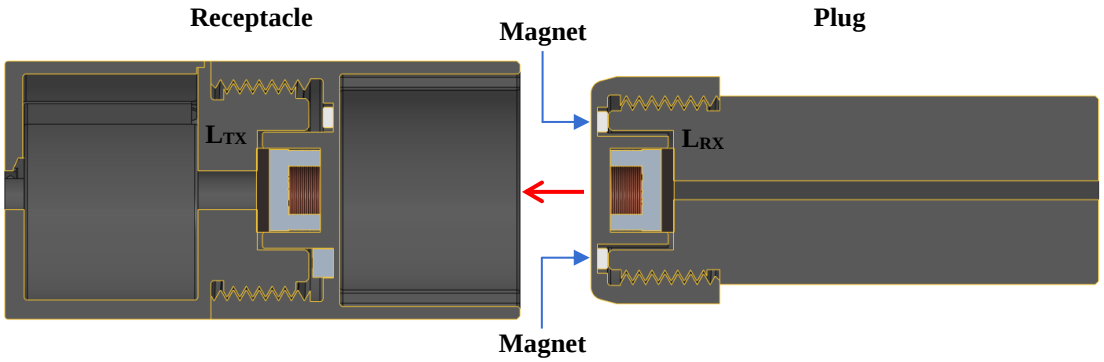

Figure 1.10: High-level model of an NMC based on inductive coupling

An example of an NMC that demonstrated a novel approach for how the concept can generate multiple passbands was presented by Zannat and Franzon using a cylindrically coupled structure [33] and was based off the original concept presented in [31] and is a method for passing both power and signal over a single interface. Both concepts of capacitive-based and inductive-based NMCs are covered and patented in [31].

While it is possible to utilize both capacitive and inductive coupling for μWPT systems, the focus in this thesis will be concentrated on inductive-based power transfer as illustrated in general model in Figure 1.11 and will be explored in the following sections and chapters. One of the main concerns in every NMC application are the restrictions on inductor geometry that will be imposed. This is the topic that will be explored in the next chapter.

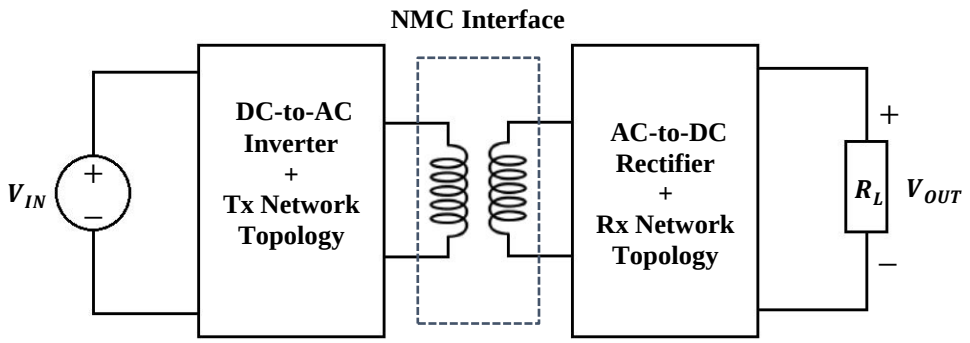

Figure 1.11: General model for inductive μWPT for NMCs

1.2.3 Nomenclature of WPT Systems

Before closing this chapter, it is appropriate to identify where on the WPT classification chart that μWPT systems might fall under. Figure 1.12 shows a classification or Nomenclature of how WPT systems are classified today [6].

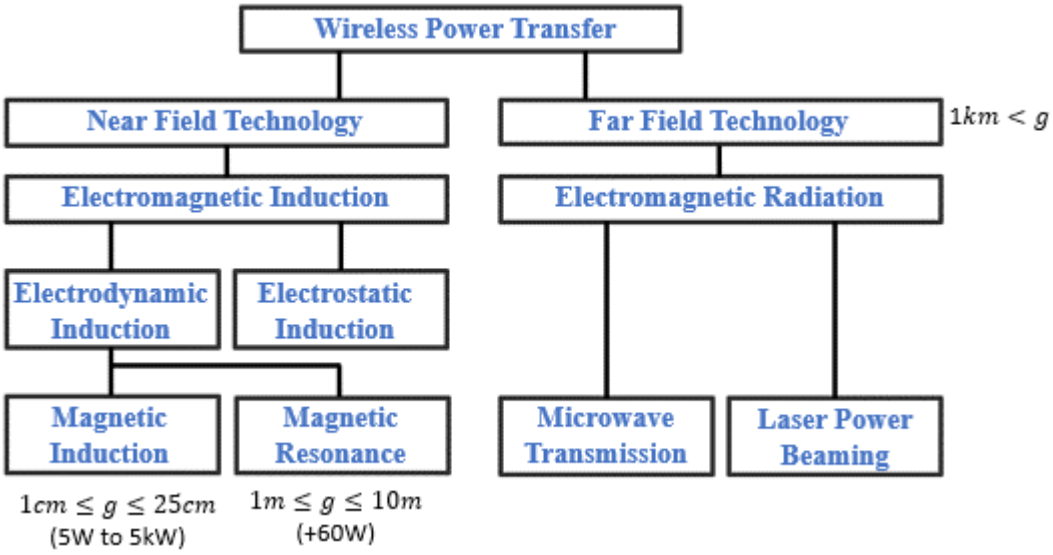

Figure 1.12: Current industry nomenclature of WPT systems

Several things determine how WPT systems are classified. These criteria are principle mechanism or technique by which power is transferred, the magnitude of power being transferred, and the distance over which that power is being transferred. As can be seen from Figure 1.12, there

are two main categories for WPT which is near field and far field technology. For WPT technology to fall under far field, the technique is radiative and transfers energy over long distances well into the km range. Near field WPT technology transfer is non-radiative and transfers energy over shorter distances. To define what it is meant by long and short distances as a general definition, if the application wavelength for the electromagnetic signal is smaller than the transfer distance the application is far field and near field if that wavelength is longer than the transfer distance [2]. Near field technology typically operates on system frequencies under 15 MHz with a separation distance of no greater than 5 cm. It falls under two categories which is electrodynamic and electrostatic induction.

As the name implies, electrostatic induction means the field is static, and power or signal data is transferred by an electric field over a dielectric material as governed by Gauss' Law (1.1). These applications utilize capacitive coupling as the principle mechanism and have very small separation distances between T_X and R_X capacitive plates. There are very limited applications due to this, but one major advantage capacitive coupling has over inductive coupling is that there is very little heat generated relative to an inductive WPT system while power is being transferred [32], [34]. This makes sense given the fact that a capacitively coupled system will not have Eddy currents at electromagnetic interfaces that normally would come with an inductive-based WPT system [35].

Electrodynamic induction utilizes inductive coupling as the principle mechanism by which power or signal data (or both) is transferred and is governed by the principles of induction, particularly equation (1.4). Magnetic resonance is the scheme used by WiTricity mentioned earlier and is generally considered to be within the midrange of WPT given that transfer distances are on the order of a few meters within the range of $1m \leq g \leq 10m$ and can reach power levels of around

60W or more. Typically, these systems are for power and use at least four resonators to accomplish the longer distances. And finally, magnetic induction on the other hand normally uses two inductor coils where both Tx and Rx coils must be concentrated and axially aligned as best as possible for the best power transfer efficiency. Separation distances typically do not go beyond 25 cm. The general consensus for these WPT applications is that they range anywhere between $1cm \leq g \leq 25cm$ with a wide range of power from 5W to about 5kW. For µWPT and NMCs, separation distances would certainly be less than 1 cm. These are very small separation distances for a very broad industry that can fall under a classification all on its own. A reasonable range for separation in most µWPT applications would be $0.5mm \leq g < 1cm$ with power ranging anywhere from 1W to 200W. This is where I propose an addition to the classification of WPT systems to include µWPT and this classification is given in Figure 1.13 in a modified nomenclature.

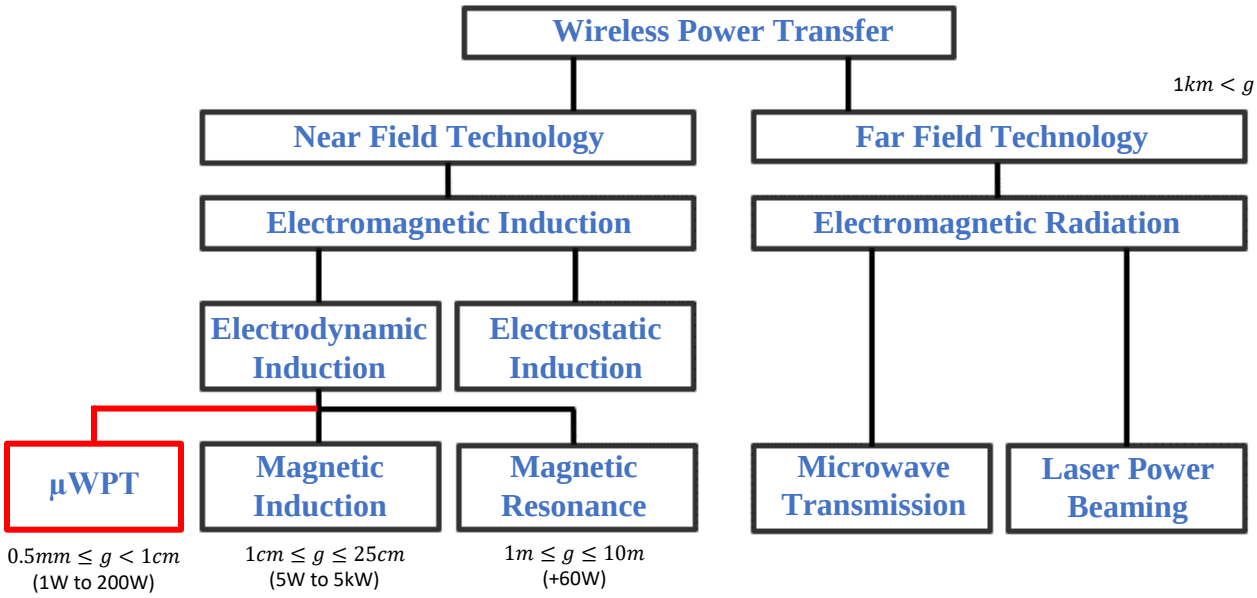

Figure 1.13: Modified nomenclature of WPT systems that includes µWPT

Now that µWPT has been introduced, motivation for it established, and a target industry identified, our attention in this thesis now turns to the performance parameters that impact power

transfer efficiency in μWPT systems. The physical geometry that inductor coils have a significant impact on power transfer efficiency. The next section will describe how. In addition to this, there are four basic network topologies for μWPT systems that have a direct impact on power transfer efficiency. The difference between the four is in the orientation of how compensation capacitance is introduced into the system circuit for the purpose of balancing out the already present inductive reactance. These four network topology circuit configurations will be studied in detail with extensive mathematical derivations for each one that seeks to establish expressions for power transfer efficiency. Simulations for each of these topologies will be carried out comparing them to each other seeking to identify which of the four performs best in μWPT systems. Followed by this, novel measurement techniques will be presented that will be based on this optimal topology, a prototype will be developed based on it, and correlation between simulations and measurements will be verified for a small form factor. The thesis will then close with other NMC examples that are based on μWPT before introducing the reader to the larger vision for how they might be applied to other industries.

Chapter 2
The Impacts of Inductor Geometry and Other Parameters

2.1 Comparing Three Inductor Geometries with the Biot-Savart Law

The focus of this section is to characterize and compare the performance of three different inductor geometries. Specifically, these geometries are a circular, square, and hexagonal loop.

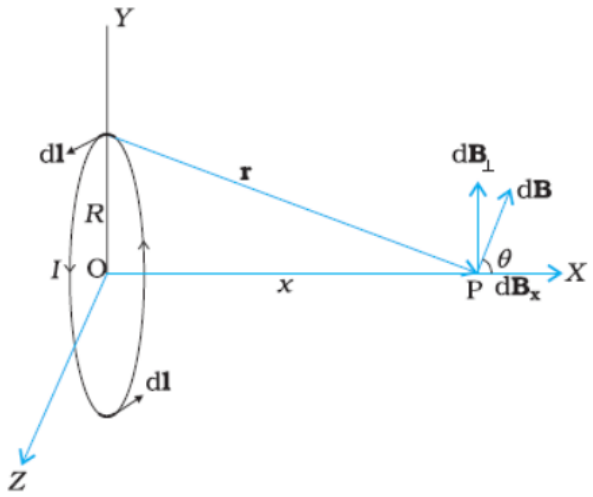

Figure 2.1: Circular loop setup for Biot-Savart Law derivation

Each of these geometries are widely used in industry for WPT systems; some are more desirable than others depending on the unique needs of the application. The purpose of this comparison is to understand if there are any objective performance benefits to use one geometry over another. In other words, if a WPT application is flexible enough such that there is no limiting space factor that would favor one geometry physically over another, why would one be chosen over another? This is the question that will be answered in this section. One of the major challenges in WPT systems is alignment. Optimal performance takes place when two coils are axially aligned. Our analysis will therefore look at each geometry and the magnitude each one has aligned at the center, creating a magnetic field at a point P in space. After this, these three results will be plotted

on one graph for comparison. For WPT systems it is important to understand how geometry impacts magnetic field strength. We can find out what that magnetic field strength is by mathematically setting up the system in Figure 2.1 and driving the result.

2.1.1 Biot-Savart Law Applied to Circular Loop

It is well established in physics that the current I traveling around a conductive wire loop has a corresponding **B**-field that is perpendicular to its flow. In looking at a small section of that wire, $d\boldsymbol{l}$, which I is flowing through, an expression for the magnetic field intensity generated by $d\boldsymbol{l}$ can be defined as: $d\boldsymbol{B} \perp |d\boldsymbol{l} \times \hat{r}|$ which means that the magnetic field is perpendicular to both that small section of wire and the unit vector pointing towards point $\boldsymbol{P}$. In all three geometries being compared (circular, square, and hexagonal), r is the same in all cases: $r^2 = x^2 + R^2$ where r is the distance from point $\boldsymbol{P}$, $\hat{r}$ is the unit vector pointing towards it and R is the circle radius. By observing the geometry, the expression in (2.1) can be derived:

$$d\boldsymbol{B} = \frac{\mu_0 I}{4\pi} \cdot \frac{|d\boldsymbol{l} \times \hat{r}|}{r^2} = \frac{\mu_0 I}{4\pi} \cdot \frac{d\boldsymbol{l}}{(x^2 + R^2)} \tag{2.1}$$

With the circular geometry, observe $\boldsymbol{P} = (x, 0,0)$, therefore:

$$d\boldsymbol{B} = d\boldsymbol{B_X} = \frac{\mu_0 I}{4\pi} \cdot \frac{\cos\theta \, d\boldsymbol{l}}{(x^2 + R^2)}$$

$$= \frac{\mu_0 I}{4\pi} \cdot \left[\frac{d\boldsymbol{l}}{(x^2 + R^2)}\right] \cdot \cos\theta$$

$$= \frac{\mu_0 I}{4\pi} \cdot \left[\frac{d\boldsymbol{l}}{(x^2 + R^2)}\right] \cdot \frac{R}{\sqrt{(x^2 + R^2)}}$$

$$= \frac{\mu_0 I}{4\pi} \cdot \frac{R d\boldsymbol{l}}{(x^2 + R^2)^{3/2}} \tag{2.2}$$

Continuing on with integrating (2.2) yields:

$$\boldsymbol{B_X} = \oint d\boldsymbol{B_X} = \frac{\mu_0 I}{4\pi} \cdot \frac{R}{(x^2 + R^2)^{3/2}} \oint d\boldsymbol{l} \tag{2.3}$$

For a circular geometry if we integrate around the loop the expression is:

$$\oint d\boldsymbol{l} = 2\pi R \tag{2.4}$$

After this, the expression becomes:

$$\boldsymbol{B_X} = \frac{\mu_0 I}{4\pi} \cdot \frac{2\pi R^2}{(x^2 + R^2)^{3/2}} = \frac{\mu_0 I R^2}{2(x^2 + R^2)^{3/2}} \tag{2.5}$$

Considering the special case where $x = 0$ places the location in space right at the center of the loop, that is at the origin. When doing this, equation (2.5) reduces to:

$$\boldsymbol{B_{X\_C}} = \frac{\mu_0 I}{2R} \tag{2.6}$$

The expression in (2.6) is for the magnetic field at point *P* along the x-axis for a circular geometry centered at the origin, and hence the variable description $\boldsymbol{B_{X\_C}}$. The same process is a square geometry, $\boldsymbol{B_{X\_S}}$, (2.7) and hexagonal, $\boldsymbol{B_{X\_H}}$, (2.8) for square and hexagonal loops, respectively, and proper mathematical derivations that arrive at these results are both given in Appendix A.

$$\boldsymbol{B_{X\_S}} = \frac{2\mu_0 I}{\pi R} \tag{2.7}$$

$$\boldsymbol{B_{X\_H}} = \frac{\sqrt{3}\mu_0 I}{\pi R} \tag{2.8}$$

The three results given by (2.6), (2.7), and (2.8) are plotted in Figure 2.2 and the MATLAB code that generated it is given in Appendix B.1.

Contrary to what intuition might suggest, the circular geometry had the lowest intensity between the three geometries holding all parameters constant. The square geometry generated the highest intensity and the hexagonal between the two. Another point worth mentioning here is that with all three cases, the derivations were performed with point $\boldsymbol{P}$ in the center of each geometry.

Misalignment will impact the field intensity significantly which agrees with simulations. In addition to this, it was observed that as the size of the radius R is inversely proportional to the magnetic field. This makes sense in the case of a single wire loop since the single center point is some distance x away from the wire. The smaller the radius is, the closer the wire is to the point and thus intensity increases.

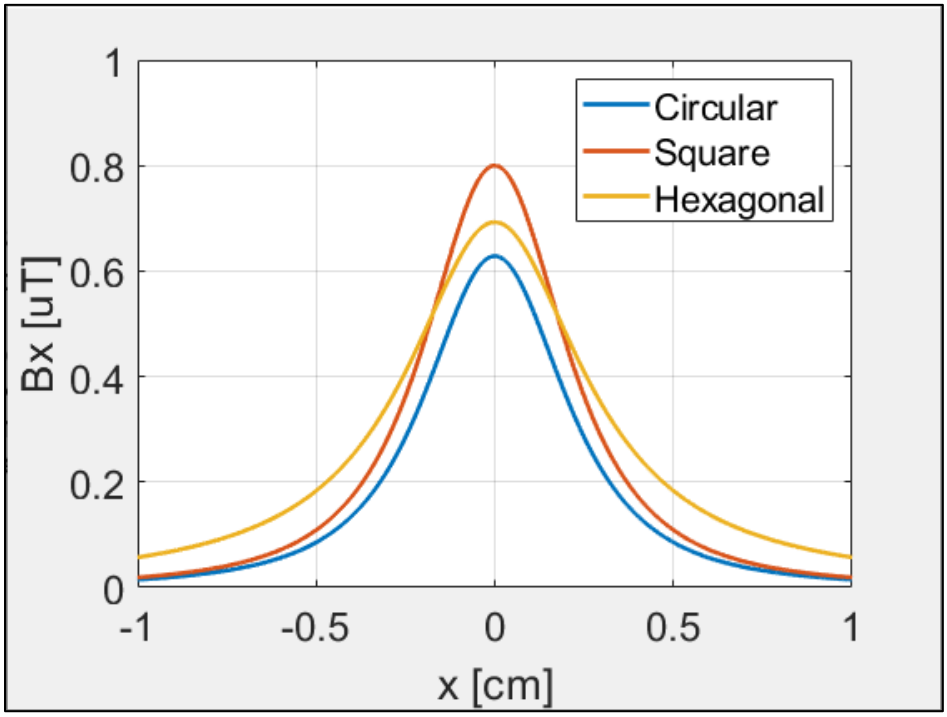

Figure 2.2: Comparison between three geometries for magnetic field intensity

Magnetic field intensity also is at optimal value when the point is directly centered at the origin, $\boldsymbol{P} = (0,0,0)$. Are there any performance benefits to use one geometry over another? Aside from the fact that the square geometry shows a slight larger peak value relative to the other two, the answer is no. The difference in magnetic field intensity between the three geometries is not very much. Because of this, the only reason one might use one geometry instead of another would be entirely dependent on the unique needs to the WPT application. Small or limited space might make one geometry more convenient to choose.

2.1.2 The Archimedean Spiral and Neumann Formula

It was established in the last study that inductor geometry matters, but in on the scale of μWPT it matters not very much in terms of performance. As was concluded in that last study, the main drivers for using one geometry over the other will be in application or manufacturing ease. The purpose of this study is to analyze two axially aligned circular Archimedean spiral spirals and the derivation of one of the most fundamental parameters in all of wireless power transfer: mutual inductance. Circular geometry was chosen primarily on the bases of symmetry and ease of calculations. Indeed, literature has advanced methods for numerically analyzing any geometry, but the circular one is the most straight forward one in terms of calculation and the methods can be applied to the other two geometries looked at in the last study. Figure 2.3 shows a general setup for the derivation for the Neumann formula using electromagnetic theory. Note, that this is for the general case and the result is independent of geometry.

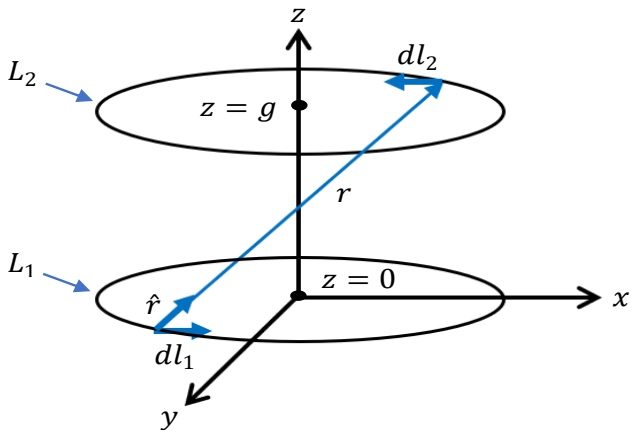

Figure 2.3: Two axially aligned wire loops for Neumann formula derivation

If a current I_1 were to flow in loop L_1, we know it will generate a magnetic field radiating perpendicular to it, call this field B_1 and from that field comes a flux ϕ_2 that cuts through loop L_2.

From Biot-Savart (2.9) we know B_1 is proportional I_1 which fades by a factor of $1/r^2$. Notice this applies to a closed-loop surface.

$$B_1 = \frac{\mu_0 I_1}{4\pi} \oint \frac{|dl_1 \times \hat{r}|}{r^2} \tag{2.9}$$

The flux generated by B_1 is what produces the current in loop L_2 which is I_2. And since $I_1 \sim \phi_2$ and we also know that in general $\phi = LI$, this means $I_1 \sim I_2$. This is an important point when we consider power efficiency in WPT systems which we will consider later when investigating it using circuit theory. But for now, we will continue with our derivation of the Neumann formula. For surface and line currents, the total flux that cuts through L_2 is a measure of divergence between the magnetic field and the surface. If we imagine the enclosed circular loops to be the enclosures of a surface (even though they are actually free space) we can be on our way to mathematically describe a concept called mutual inductance.

$$d\phi_2 = B_1 \cdot da_2 \tag{2.10}$$

Equation (2.10) is a small portion of the flux generated by the transmitting field that cuts a small portion of the encapsulated surface area A_2 by L_2, where a_2 is that small portion of the larger surface area. Integrating this describes the full flux:

$$\phi_2 = \int d\phi_2 = \int B_1 \cdot da_2 \tag{2.11}$$

Given the fact that this is a line current describing the flux through a surface:

$$A_1 = \frac{\mu_0 I_1}{4\pi} \oint_{L_1} \frac{dl_1}{r} \tag{2.12}$$

Stokes' Theorem (2.13) can be used to relate ϕ_2 that cuts through A_2 to the current flowing through L_2 which is I_2:

$$\iint_S (\nabla \times A_1) \cdot da_2 = \oint_{L_2} A_1 \cdot dl_2 \tag{2.13}$$

Given (2.12) and substituting it into (2.13), we have a more complete expression for (2.11):

$$\begin{aligned} \phi_2 &= \oint_{L_2} A_1 \cdot dl_2 \\ &= \oint_{L_2} \left(\frac{\mu_0 I_1}{4\pi} \oint_{L_1} \frac{dl_1}{r} \right) \cdot dl_2 \\ &= \frac{\mu_0 I_1}{4\pi} \oint_{L_1} \oint_{L_2} \frac{dl_1 \cdot dl_2}{r} \end{aligned} \tag{2.14}$$

Once again, since $\phi = LI$, we arrive at one of the fundamental concepts of WPT theory:

$$L_m = \frac{\phi_2}{I_1} = \frac{\mu_0}{4\pi} \oint_{L_1} \oint_{L_2} \frac{dl_1 \cdot dl_2}{r} \tag{2.15}$$

Equation (2.15) is called the Neumann formula and it describes the mutual inductance between two inductor coils of wire. It utilizes a double line integral since two integrations take place around each loop in Figure 2.3. Three very important insights stand out from 2.15), and the first is that inductor geometry certainly does matter, the further apart the two inductors are, the weaker the mutual inductance is between them, and it does not matter which of the two inductors does the transmitting and receiving of current. In other words, whatever the geometry and positions of the loops, the flux through L_2 when we send a current around L_1 will be identical to the flux through L_1 when the same current is sent around L_2 [36].

Taking this a step further, we will now extend this from a system to two concentric axially aligned wire loops with a single turn ($N = 1$) as in Figure 2.3 to two concentric axially aligned Archimedean spirals shown in Figure 2.4. The inner and outer radius, screw pitch, core material, and number of turns is what determines the self-inductance of any inductor.

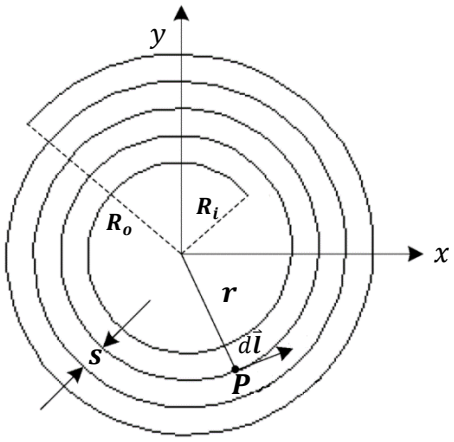

Figure 2.4: Archimedean spiral [37] showing an inner ($\boldsymbol{R_i}$) and outer ($\boldsymbol{R_o}$) radius, screw pitch ($\boldsymbol{s}$), differential element ($d\vec{\boldsymbol{l}}$) and at point $\boldsymbol{P}$ on the spiral with radius length from origin $\boldsymbol{r}$.

In the case of two axially aligned concentric Archimedean spirals, not only do these factors influence mutual inductance, but so does the separation distance. With the parameters in Figure 2.4 defined, driving an expression for L_m for this geometry can now be done and requires a bit more analysis. For the setup in Figure 8, polar coordinates are used at $\boldsymbol{P}(r, \theta)$ where:

$$r = \frac{s}{2\pi}\theta, \text{ where } \varphi_i \leq \theta \leq \varphi_o \tag{2.16}$$

Setting $a = \frac{s}{2\pi}$, we have $\varphi_i = \frac{R_i}{a} = \frac{2\pi R_i}{s}$ and $\varphi_o = \frac{R_o}{a} = \frac{2\pi R_o}{s}$. In other words, the two limits for (2.16) become 2.17) which basically mean r can extend out to any point on the inner and outer circumference (and any point in between) on the Archimedean spiral.

$$r = \frac{s}{2\pi}\theta, \text{ where } \frac{2\pi R_i}{s} \leq \theta \leq \frac{2\pi R_o}{s} \tag{2.17}$$

Converting these polar coordinates to rectangular coordinates these become $x = a\theta\cos\theta$ and $y = a\theta\sin\theta$. Therefore, at a point $\boldsymbol{P}$ on the Archimedean spiral in Figure 8, the tangential differential element $d\vec{\boldsymbol{l}}$ is:

$$d\vec{\boldsymbol{l}} = dx\vec{\boldsymbol{\imath}} + dy\vec{\boldsymbol{\jmath}} = a[(\cos\theta - \theta\sin\theta)\vec{\boldsymbol{\imath}} + (\sin\theta - \theta\cos\theta)\vec{\boldsymbol{\jmath}}]d\theta \tag{2.18}$$

Figure 2.5 shows a setup generated in MATLAB for two axially aligned Archimedean spiral inductors separated by a distance called an air "gap", g.

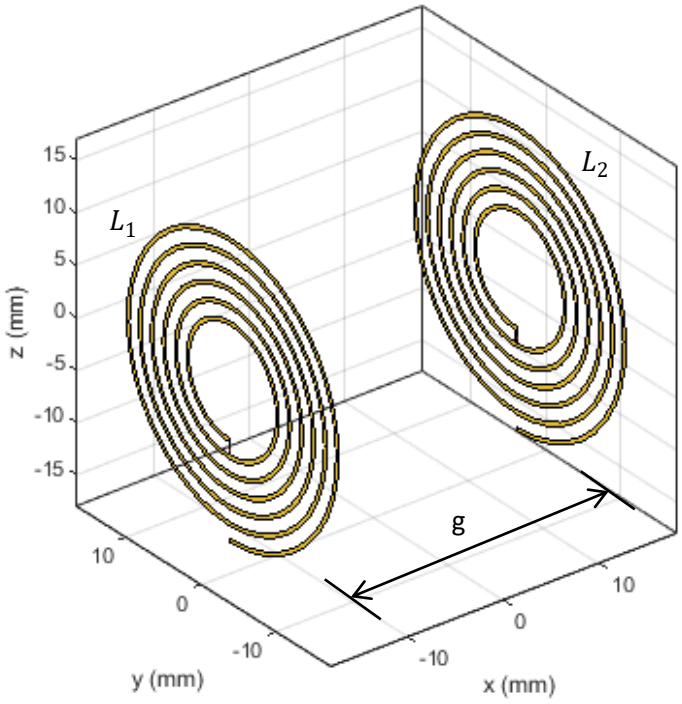

Figure 2.5: Archimedean spiral system generated in MATLAB (see Appendix B.2) showing an axially aligned system with L_1 and L_2 separated by an air "gap", g

There are now two spirals (L_1 and L_2). L_1 is the transmitter T_X and L_2 is the receiver R_X. Considered independently and individually, each spiral has its own screw pitch (s_1 and s_2), and inner and outer radii for both (L_1: R_{i1}, R_{o1} and L_2: R_{i2}, R_{o2}). The equations can be broken down as follows.

$$\boldsymbol{P}(r_1, \theta_1, z_1) = \boldsymbol{P}(a_1\theta_1, \theta_1, 0), \text{ where } \varphi_{i1} \leq \theta_1 \leq \varphi_{o1} \tag{2.19}$$

$$\boldsymbol{Q}(r_2, \theta_2, z_2) = \boldsymbol{Q}(a_2\theta_2, \theta_2, h), \text{ where } \varphi_{i2} \leq \theta_2 \leq \varphi_{o2} \tag{2.20}$$

Following the definition in (2.17):

$$\varphi_{i1} = \frac{R_{i1}}{a_1} = \frac{2\pi R_{i1}}{s_1} \text{ and } \varphi_{o1} = \frac{R_{o1}}{a_1} = \frac{2\pi R_{o1}}{s_1} \tag{2.21}$$

$$\varphi_{i2} = \frac{R_{i2}}{a_2} = \frac{2\pi R_{i2}}{s_2} \text{ and } \varphi_{o2} = \frac{R_{o2}}{a_2} = \frac{2\pi R_{o2}}{s_2} \tag{2.22}$$

Due to the symmetrical nature of this problem, cylindrical coordinates will be used. Thus:

$$\boldsymbol{P}(r_1, \theta_1, 0) = \boldsymbol{P}(r_1 \cos\theta_1 , r_1 \sin\theta_1 , 0) \tag{2.23}$$

$$\boldsymbol{Q}(r_2, \theta_2, h) = \boldsymbol{Q}(r_2 \cos\theta_2 , r_2 \sin\theta_2 , g) \tag{2.24}$$

Both tangential vectors at points $\boldsymbol{P}$ and $\boldsymbol{Q}$ are $d\vec{\boldsymbol{l}}_1$ and $d\vec{\boldsymbol{l}}_2$, respectively. Therefore:

$$d\vec{\boldsymbol{l}}_1 = a_1[(\cos\theta_1 - \theta_1 \sin\theta_1)\vec{\boldsymbol{\imath}} + (\sin\theta_1 - \theta_1 \cos\theta_1)\vec{\boldsymbol{\jmath}}]d\theta_1 \tag{2.25}$$

$$d\vec{\boldsymbol{l}}_2 = a_2[(\cos\theta_2 - \theta_2 \sin\theta_2)\vec{\boldsymbol{\imath}} + (\sin\theta_2 - \theta_2 \cos\theta_2)\vec{\boldsymbol{\jmath}}]d\theta_2 \tag{2.26}$$

$$d\vec{\boldsymbol{l}}_1 \cdot d\vec{\boldsymbol{l}}_2 = a_1 a_2[(1 + \theta_1\theta_2)\cos(\theta_2 - \theta_1) - (\theta_2 - \theta_1)\sin(\theta_2 - \theta_1)]d\theta_1 d\theta_2 \tag{2.27}$$

Applying and equation (2.15) the Neumann formula expression becomes:

$$L_m = \frac{\mu_0}{4\pi} a_1 a_2 \int_{\varphi_{i2}}^{\varphi_{o2}} \int_{\varphi_{i1}}^{\varphi_{o1}} \frac{(1 + \theta_1\theta_2)\cos(\theta_2 - \theta_1) - (\theta_2 - \theta_1)\sin(\theta_2 - \theta_1)}{\sqrt{g^2 + a_1^2\theta_1^2 + a_2^2\theta_2^2 - 2a_1 a_2 \theta_1 \theta_2 \cos(\theta_2 - \theta_1)}} d\theta_1 d\theta_2 \tag{2.28}$$

Equation (2.28) is the final and general result for the theoretical calculated expression for mutual inductance L_m between any two circular spiral inductors. In other words, L_1 and L_2 need not be the same; one can be larger or smaller than the other. In the case where the two inductors are identical in geometry (where $L_1 = L_2$), equation (2.28) can simplify significantly. That is, both L_1 and L_2 have the same screw pitch ($s = s_1 = s_2$) and consequently, $a = a_1 = a_2$. This also means the limits of integration in equations (2.21) and (2.22) reduce only to φ_i and φ_o on both accounts. Therefore (2.27) simplifies to (2.29) and (2.28) simplifies to (2.30).

$$d\vec{\boldsymbol{l}}_1 \cdot d\vec{\boldsymbol{l}}_2 = a^2[(1 + \theta_1\theta_2)\cos(\theta_2 - \theta_1) - (\theta_2 - \theta_1)\sin(\theta_2 - \theta_1)]d\theta_1 d\theta_2 \tag{2.29}$$

$$L_m = \frac{\mu_0 a^2}{4\pi} \int_{\varphi_i}^{\varphi_o} \int_{\varphi_i}^{\varphi_o} \frac{(1 + \theta_1\theta_2)\cos(\theta_2 - \theta_1) - (\theta_2 - \theta_1)\sin(\theta_2 - \theta_1)}{\sqrt{g^2 + a^2[(\theta_1^2 + \theta_2^2) - 2\theta_1\theta_2\cos(\theta_2 - \theta_1)]}} d\theta_1 d\theta_2 \tag{2.30}$$

2.1.3 Separation Distance and Other Parameters

L_m is a fundamental parameter in WPT theory that depends not only on the individual parameters of the two inductors themselves (such as self-inductance and geometric shape), but also on the separation distance between them, which is the air gap, g. Figure 2.6a shows a MATLAB plot for equation (2.30) and Figure 2.6b is a MATLAB plot for the coupling coefficient verses g.

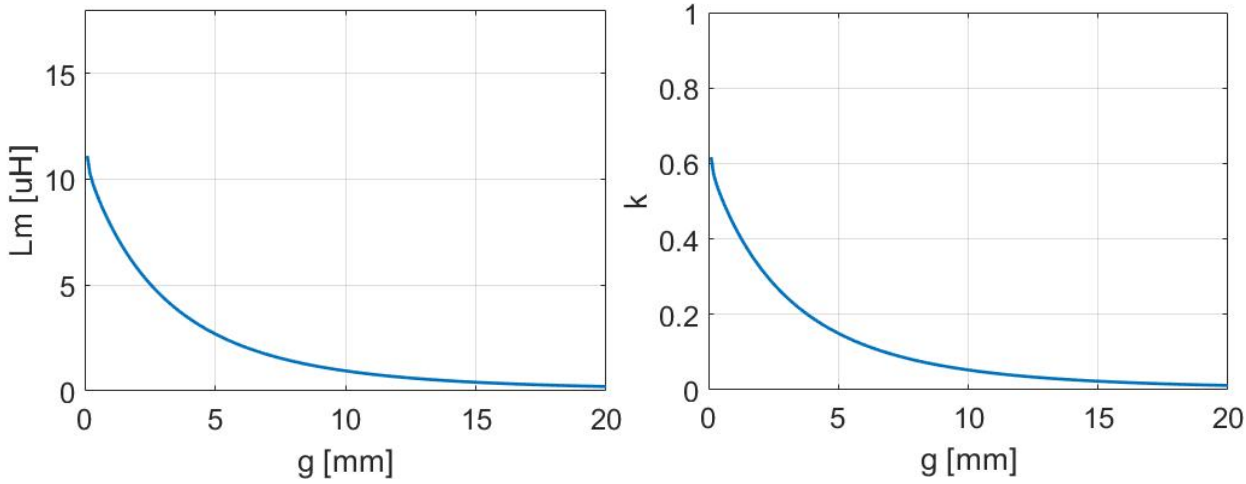

(a) (b)

Figure 2.6: MATLAB simulation of (2.30) (Appendix B.3) showing (a) mutual inductance (L_m) and (b) the coupling coefficient (k), respectively with respect to separation distance (g)

The coupling coefficient (k) is a measure of the flux linkage between any two coils set up in a configuration like Figure 2.7 where energy is being transferred between L_1 and L_2. It is given as a ratio as given in (2.31) and relates the two self-inductance (L_1 and L_2), and L_m.

$$k = \frac{L_m}{\sqrt{L_1 L_2}} \tag{2.31}$$

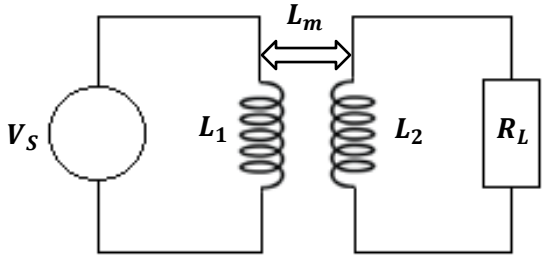

Figure 2.7: Circuit configuration showing mutual inductance between L_1 *and* L_2

In the case when $L = L_1 = L_2$, equation (2.31) simplifies to (2.32):

$$k = \frac{L_m}{L} \tag{2.32}$$

From (2.15) and (2.30), we can see an inverse relationship between L_m and g, or $L_m \propto 1/g$. Since $L_m = kL$ per (2.32), this also means $k \propto 1/g$ which would agree with the behavior displayed in Figure 3.14b. L_m is a critical parameter in optimization of power transfer efficiency between L_1 and L_2 [38], [39]. The same thing can be said about frequency and coupling coefficient which is what will be investigated further in the next section. Up until this point, we have considered mutual inductance from the standpoint of electrodynamics in the derivation of the Neumann formula (2.15) and a specific application to two mutually coupled Archimedean spiral inductors (2.28 and 2.30). There is a striking observation to be made which might be an obvious one: mutual inductance depends entirely on physical inductor qualities, specifically core material and geometry.

2.1.4 Four Network Compensation Topologies

Compensation is an extremely important aspect of WPT systems. Anytime there are energy storage elements such as capacitors and inductors there will be reactive power introduced into the system. In our case, it is the WPT system. The ultimate goal of WPT is for the real power on the Tx side to be transmitted to the Rx side as efficiently as possible. Because of the nature of the WPT system, there are two inductors shown in Figure 2.7, inductor L_1 and inductor L_2; both are energy storage elements. When the time varying signal is generated by the source, there will be reactive power due to the storage of energy. The real power is what we care about getting to the load. Because of this, it is critical that we eliminate reactive power at the source. The way we do this is with capacitive compensation.

In the absence of capacitive compensation, the voltage will lag the current by a certain amount. This is what causes reactive power. Capacitive compensation essentially brings the voltage and current back into phase and by doing so reduces the Volt-Amperes (VA) rating of the source driving the power factor to unity. This is the ideal condition: when there is no lag between voltage and current. It is the condition required to transfer all the real power from the source to the load. However, this is not without some careful design considerations. The main design consideration is resonance condition which is the critical frequency at which all reactive power is zero and the power dissipated is purely resistive physically. In the case for all four compensation topologies for WPT systems, the secondary capacitance is always chosen first per (2.33).

$$\omega_0 = \frac{1}{\sqrt{(L_2 - L_m)C_2}} \tag{2.33}$$

Where $\omega_0 = 2\pi f_0$, and f_0 is the critical frequency for resonance. When calculating the value for R_X capacitance, the desired critical frequency will be defined per industry standards. Modifying (2.33), C_2 can be calculated by (2.34).

$$C_2 = \frac{1}{\omega_0^2(L_2 - L_m)} = \frac{1}{4\pi^2 f_0^2(L_2 - L_m)} \tag{2.34}$$

The selection for T_X or primary capacitance requires some detailed analysis. The four cases are Series-Series (SS), Series-Parallel (SP), Parallel-Series (PS), and Parallel-Parallel (PP), and each has unique characteristics. The analysis that follows will compare these unique characteristics and then an objective decision will be made on which of the four topologies is best from a performance standpoint for connector applications.

2.1.4.1 Series-Series (SS)

Figure 2.8 shows the schematic diagram for SS topology. Notice that both capacitors on

T_X (primary) and R_X (secondary) sides are in series with L_1 and L_2. R_1 and R_2 are the internal dc resistances for both L_1 and L_2, respectively, and R_L is the load resistance.

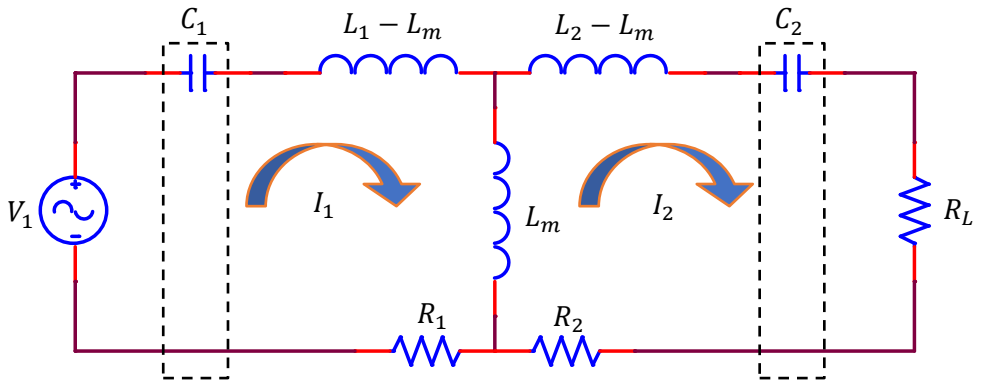

Figure 2.8: Schematic diagram for SS-Topology equivalent model

The first order of business is the calculate the input impedance as seen by the source, Z_{IN}. To do this, we apply Kirkoff's voltage and current laws. Write the first one:

$$V_1 = \frac{1}{j\omega C_1} I_1 + j\omega(L_1 - L_m)I_1 + R_1 I_1 - j\omega L_m I_2 = \left(\frac{1}{j\omega C_1} + j\omega(L_1 - L_m) + R_1\right) I_1 - j\omega L_m I_2 \quad (2.35)$$

Write the second mesh equation:

$$j\omega L_m I_1 = \frac{1}{j\omega C_2} I_2 + j\omega(L_2 - L_m)I_2 + R_2 I_2 + R_L I_2 = \left(\frac{1}{j\omega C_2} + j\omega(L_2 - L_m) + R_2 + R_L\right) I_2 \quad (2.36)$$

Write I_2 in terms of I_1:

$$I_2 = \frac{j\omega L_m}{R_L + R_2 + j\omega(L_2 - L_m) + 1/j\omega C_2} I_1 \quad (2.37)$$

Insert (2.37) into (2.36) and solve for Z_{IN}.

$$V_1 = \left[R_1 + j\omega(L_1 - L_m) - \frac{j}{\omega C_1} - j\omega L_m \left(\frac{j\omega L_m}{R_L + R_2 + j\omega(L_2 - L_m) + 1/j\omega C_2}\right)\right] I_1 \quad (2.38)$$

$$= \left[R_1 + j\omega(L_1 - L_m) - \frac{j}{\omega C_1} + \frac{\omega^2 L_m^2}{R_L + R_2 + j\omega(L_2 - L_m) + 1/j\omega C_2}\right] I_1 \quad (2.39)$$

$$Z_{IN} = \frac{V_1}{I_1} = R_1 + j\omega(L_1 - L_m) - \frac{j}{\omega C_1} + \frac{\omega^2 L_m^2}{R_L + R_2 + j\omega(L_2 - L_m) + 1/j\omega C_2} \tag{2.40}$$

Equation (3.44) is the input impedance as seen by the source. It is critical that this parameter be purely resistive meaning no reactive components are present. This is where the primary compensation capacitance (i.e., C_1) comes into play and is solved. By taking the complex conjugate of (3.44) and setting the imaginary part equal to zero, we can solve for C_1. Mathematically, this condition is described as $Im\{Z_{IN}^*\} = 0$, where Z_{IN}^* is the complex conjugate of (2.40).

$$Z_{IN}^* = R_1 + \omega(L_1 - L_m) - \frac{1}{\omega C_1} - \frac{\omega^2 L_m^2}{R_L + R_2 + \omega(L_2 - L_m) + 1/\omega C_2} \tag{2.41}$$

$$Im\{Z_{IN}^*\} = \omega(L_1 - L_m) - \frac{1}{\omega C_1} - \frac{\omega^2 L_m^2}{\omega(L_2 - L_m) + 1/\omega C_2} = 0 \tag{2.42}$$

$$\frac{1}{\omega C_1} = \omega(L_1 - L_m) - \frac{\omega^2 L_m^2}{\omega(L_2 - L_m) + 1/\omega C_2} \tag{2.43}$$

Considering the fact that C_2, the secondary capacitance, is given by (2.35) at resonance:

$$\omega_0 C_1 = \frac{C_1}{\sqrt{(L_2 - L_m)C_2}} \rightarrow \frac{1}{\omega_0 C_1} = \frac{\sqrt{(L_2 - L_m)C_2}}{C_1} \tag{2.44}$$

$$\omega_0 C_2 = \frac{C_2}{\sqrt{(L_2 - L_m)C_2}} \rightarrow \frac{1}{\omega_0 C_2} = \frac{\sqrt{(L_2 - L_m)C_2}}{C_2} \tag{2.45}$$

$$\omega_0(L_1 - L_m) = \frac{L_1 - L_m}{\sqrt{(L_2 - L_m)C_2}} \tag{2.46}$$

$$\omega_0(L_2 - L_m) = \frac{L_2 - L_m}{\sqrt{(L_2 - L_m)C_2}} \tag{2.47}$$

Inserting (2.44) to (2.47) into (2.43) works out to be:

$$\frac{\sqrt{(L_2 - L_m)C_2}}{C_1} = \frac{L_1 - L_m}{\sqrt{(L_2 - L_m)C_2}} - \frac{\omega^2 L_m^2}{\frac{L_2 - L_m}{\sqrt{(L_2 - L_m)C_2}} + \frac{\sqrt{(L_2 - L_m)C_2}}{C_2}}$$

$$= \frac{L_1 - L_m}{\sqrt{(L_2 - L_m)C_2}} - \frac{\omega^2 L_m^2}{\frac{(L_2 - L_m)C_2 - (L_2 - L_m)C_2}{C_2\sqrt{(L_2 - L_m)C_2}}}$$

$$= \frac{L_1 - L_m}{\sqrt{(L_2 - L_m)C_2}} \tag{2.48}$$

$$C_1(L_1 - L_m) = C_2(L_2 - L_m) = \frac{L_2 - L_m}{\omega_0^2(L_2 - L_m)} = \frac{1}{\omega_0^2} \tag{2.49}$$

$$\therefore \quad C_1 = \frac{1}{\omega_0^2(L_1 - L_m)} \tag{2.50}$$

The result in (2.50) is the primary capacitance required to balance the reactive power and bring the power factor to unity. Given the symmetrical nature of SS topology, we would have expected this. With the secondary also being at resonance, only the dc components are dissipating power. Therefore, the power transfer efficiency under these conditions can be calculated as follows.

$$\eta_{SS} = \frac{P_{OUT}}{P_{IN}} = \frac{|I_2|^2 R_L}{|I_1|^2 R_1 + |I_2|^2 R_2 + |I_2|^2 R_L} = \frac{|I_2|^2 R_L}{|I_1|^2 R_1 + |I_2|^2 (R_2 + R_L)} \tag{2.51}$$

Refering back to (2.38) which expresses I_2 in terms of I_1, and considering the fact that the reactive components are now reduced to zero, (2.38) reduces to:

$$I_2 = \frac{\omega L_m}{R_L + R_2} I_1 \rightarrow I_1 = \frac{R_L + R_2}{\omega L_m} I_2 \tag{2.52}$$

Squaring the absolute value of (2.52), and inserting into (2.51), the expression simplifies to:

$$\eta_{SS} = \frac{|I_2|^2 R_L}{|I_2|^2 \left[\frac{R_1(R_2 + R_L)^2}{\omega_0^2 L_m^2} + (R_2 + R_L)\right]} = \frac{R_L}{(R_2 + R_L)\left[\frac{R_1(R_2 + R_L)^2}{\omega_0^2 L_m^2} + 1\right]} \tag{2.53}$$

Factoring out the term $(R_2 + R_L)$ allows us to see that an expression for the maximum possible efficiency depends primarally on the load. When the following condition holds:

$$\omega_0 \gg \frac{\sqrt{R_1(R_2 + R_L)}}{L_m} \tag{2.54}$$

This means $\frac{R_1(R_2+R_L)^2}{\omega_0^2 L_m^2} \rightarrow 0$. Consequently, when this condition holds, (2.53) reduces even further:

$$\eta_{SS\_MAX} = \frac{R_L}{R_2 + R_L} \tag{2.55}$$

Equation (2.55) is the peak efficiency possible for WPT systems using SS topology. Notice that is depends on the internal resistance of L_2 and the load.

2.1.4.2 Series-Parallel (SP)

Figure 2.9 shows the schematic diagram for SP topology. Notice that the configuration is different in comparison to Figure 2.8 in that the capacitor on the T_X side (primary) is in series with L_1 and the capacitor on the R_X side (secondary) is in parallel with L_2. R_1 and R_2 are the internal dc resistance(s) for both L_1 and L_2, respectively, and R_L is the load resistance.

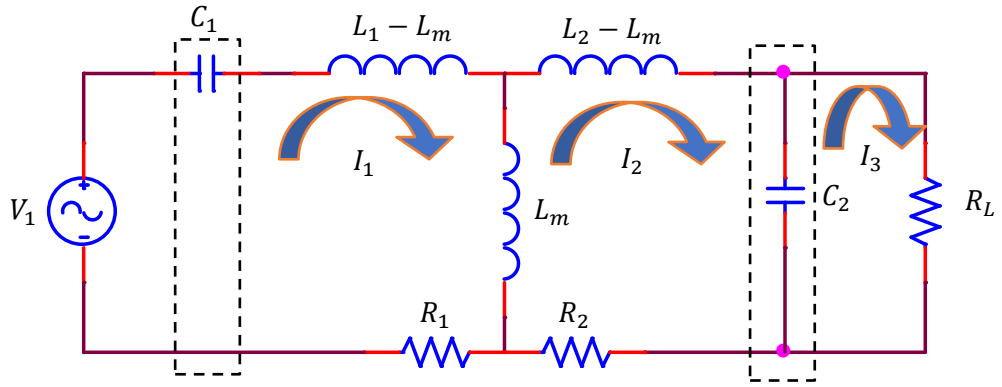

Figure 2.9: Schematic diagram for SP-Topology equivalent model

With this topology there are three mesh equations with the third current flowing between C_2 and R_L. We start the analysis like any other circuit using Kirkoff's Laws.

$$V_1 = \frac{1}{j\omega C_1} I_1 + j\omega(L_1 - L_m)I_1 + R_1 I_1 - j\omega L_m I_2$$

$$= \left(\frac{1}{j\omega C_1} + j\omega(L_1 - L_m) + R_1\right) I_1 - j\omega L_m I_2 \tag{2.56}$$

$$j\omega L_m I_1 = j\omega(L_2 - L_m)I_2 + R_2 I_2 + (X_{C2} \| R_L) I_2$$

$$= j\omega(L_2 - L_m)I_2 + R_2 I_2 + \left(\frac{j\omega C_2 R_L}{R_L + j\omega C_2}\right) I_2$$

$$= \left[j\omega(L_2 - L_m) + R_2 + \left(\frac{j\omega C_2 R_L}{R_L + j\omega C_2}\right)\right] I_2 \quad (2.57)$$

$$X_{C2}(I_2 - I_3) + R_L I_3 = \frac{1}{j\omega C_2} I_2 - \left(R_L - \frac{1}{j\omega C_2}\right) I_3 = 0 \quad (2.58)$$

Equations (2.56), (2.57), and (2.58) are the three mesh equations based on analysis of Figure 2.9. Expanding these equations out and summarizing in matrix form reduces to (2.59).

$$\begin{bmatrix} V_1 \\ 0 \\ 0 \end{bmatrix} = \begin{bmatrix} R_1 + j\omega(L_2 - L_m) - \frac{j}{\omega C_2} & -j\omega L_m & 0 \\ -j\omega L_m & R_1 + j\omega(L_2 - L_m) + \frac{j\omega C_2 R_L}{R_L + j\omega C_2} & 0 \\ 0 & -\frac{j}{\omega C_2} & R_L + \frac{j}{\omega C_2} \end{bmatrix} \begin{bmatrix} I_1 \\ I_2 \\ I_3 \end{bmatrix} \quad (2.59)$$

In the same way that it was done for SS topology, Z_{IN} can be calculated by rewriting (2.57) and expressing I_2 in terms of I_1:

$$I_2 = \frac{j\omega L_m}{j\omega(L_2 - L_m) + R_2 + \frac{j\omega C_2 R_L}{R_L + j\omega C_2}} I_1 \quad (2.60)$$

Insert (2.60) into (2.56) and simplify:

$$V_1 = \left[\frac{1}{j\omega C_1} + j\omega(L_1 - L_m) + R_1 + \frac{\omega^2 L_m^2}{j\omega(L_2 - L_m) + R_2 + \frac{j\omega C_2 R_L}{R_L + j\omega C_2}}\right] I_1 \quad (2.61)$$

The input impedance as seen by the source therefore is:

$$Z_{IN} = \frac{V_1}{I_1} = R_1 + j\omega(L_1 - L_m) - \frac{j}{\omega C_1} + \frac{\omega^2 L_m^2}{j\omega(L_2 - L_m) + R_2 + \frac{j\omega C_2 R_L}{R_L + j\omega C_2}} \quad (2.62)$$

Calculating an expression for the primary capacitance can be done by calculating the complex

conjugate of (2.62) and setting the imaginary components equal to zero. This exercise will be completed in the appendix. Calculating the power transfer efficiency is the more important matter. As was done with the previous topology, the same concept applies for SP topology when calculating efficiency.

$$\eta_{SP} = \frac{P_{OUT}}{P_{IN}} = \frac{|I_3|^2 R_L}{|I_1|^2 R_1 + |I_2|^2 R_2 + |I_3|^2 R_L} \tag{2.63}$$

Equation (2.58) can be simplified to:

$$I_2 = (1 - j\omega C_2 R_L) I_3 \tag{2.64}$$

Taking the absolute value of (2.64) and squaring:

$$|I_2|^2 = (1 - j\omega C_2 R_L)^2 |I_3|^2 \tag{2.65}$$

Inserting (2.65) into (2.63):

$$\eta_{SP} = \frac{P_{OUT}}{P_{IN}} = \frac{|I_3|^2 R_L}{|I_1|^2 R_1 + |I_3|^2 [(1 - \omega C_2 R_L)^2 R_2 + R_L]} \tag{2.66}$$

Express I_1 in terms of I_3 by inserting (3.68) into (3.61) then squaring the absolute value:

$$j\omega L_m I_1 = \left[j\omega (L_2 - L_m) + R_2 + \left(\frac{j\omega C_2 R_L}{R_L + j\omega C_2} \right) \right] (1 - j\omega C_2 R_L) I_3 \tag{2.67}$$

$$I_1 = \frac{\left[j\omega (L_2 - L_m) + R_2 + \left(\frac{j\omega C_2 R_L}{R_L + j\omega C_2} \right) \right] (1 - j\omega C_2 R_L)}{j\omega L_m} I_3 \tag{2.68}$$

$$|I_1|^2 = \frac{\left[\omega (L_2 - L_m) + R_2 + \left(\frac{\omega C_2 R_L}{R_L + \omega C_2} \right) \right]^2 (1 - \omega C_2 R_L)^2}{\omega^2 L_m^2} |I_3|^2 \tag{2.69}$$

Insert (2.69) into (2.66) to simplify the expression further:

$$\eta_{SP} = \frac{R_L}{\frac{R_1 \left[\omega (L_2 - L_m) + R_2 + \left(\frac{\omega C_2 R_L}{R_L + \omega C_2} \right) \right]^2 (1 - \omega C_2 R_L)^2}{\omega^2 L_m^2} [(1 - \omega C_2 R_L)^2 R_2 + R_L]} \tag{2.70}$$

Considering the condition for maximum peak power transfer efficiency, this takes place at resonance frequency and when the following condition holds:

$$\omega_0 \gg \frac{\sqrt{R_1\left(R_2 + \omega_0(L_2 - L_m) + \frac{\omega_0 C_2 R_L}{R_L + \omega_0 C_2}\right)^2 (1 - \omega_0 C_2 R_L)^2}}{L_m} \tag{2.71}$$

When (2.71) holds true, (2.70) reduces to:

$$\eta_{SP\_MAX} = \frac{R_L}{(1 - \omega_0 C_2 R_L)^2 R_2 + R_L} \tag{2.72}$$

The final expression of η_{SP_MAX} is after we apply (2.34). Inserting this into (2.72), the final form finally is equation (2.73).

$$\eta_{SP\_MAX} = \frac{R_L}{R_L + R_2 - \frac{R_2 R_L}{\omega_0(L_2 - L_m)}} \tag{2.73}$$

2.1.4.3 Parallel-Series (PS)

Figure 2.10 shows the schematic diagram for PS topology. Notice that the configuration is the opposite of SP topology in Figure 2.9 in that the capacitor orientation is reversed. That is, the capacitor on the T_X side (primary) is in parallel with L_1 and the capacitor on the R_X side (secondary) is in series with L_2. R_1 and R_2 are the internal dc resistance(s) for both L_1 and L_2, respectively, and R_L is the load resistance.

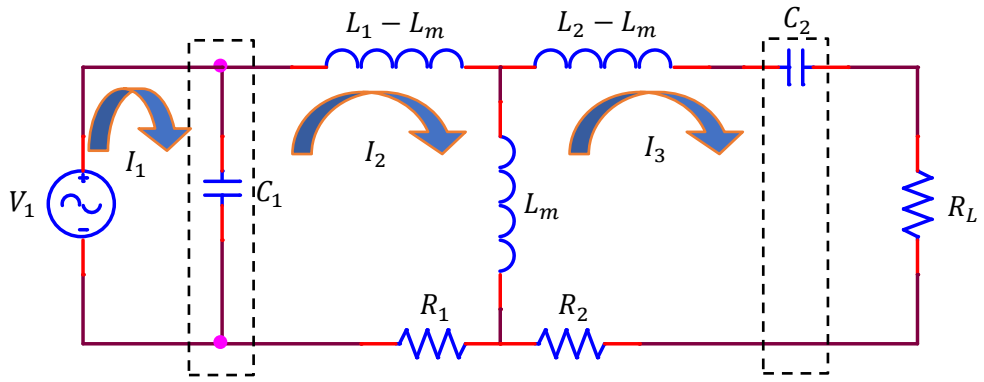

Figure 2.10: Schematic diagram for PS-Topology equivalent model

With this topology there are also three mesh equations with the voltage at the source being the same as the voltage across C_1. We start the analysis like any other circuit using Kirkoff's Laws.

$$V_1 = X_{C1}(I_1 - I_2) = X_{C1}I_1 - X_{C1}I_2 \tag{2.74}$$

$$X_{C1}(I_2 - I_1) + R_1 I_2 + j\omega(L_1 - L_m)I_2 - j\omega L_m I_3 = 0 \tag{2.75}$$

$$X_{C1}I_1 = \big(X_{C1} + R_1 + j\omega(L_1 - L_m)\big)I_2 - j\omega L_m I_3 \tag{2.76}$$

$$j\omega L_m I_2 = R_2 I_3 + j\omega(L_1 - L_m)I_3 + X_{C2}I_3 + R_L I_3$$

$$= \big(R_2 + R_L + X_{C2} + j\omega(L_1 - L_m)\big)I_3 \tag{2.77}$$

Equations (2.74) – (2.77) are the mesh equations based on analysis of Figure 2.10. Expanding these equations out and summarizing in matrix form reduces to (2.78).

$$\begin{bmatrix} V_1 \\ 0 \\ 0 \end{bmatrix} = \begin{bmatrix} -\frac{j}{\omega C_1} & \frac{j}{\omega C_1} & 0 \\ \frac{j}{\omega C_1} & -\frac{j}{\omega C_1} + R_1 + j\omega(L_1 - L_m) & -j\omega L_m \\ 0 & -j\omega L_m & R_2 + R_L + \frac{j}{\omega C_2} + j\omega(L_1 - L_m) \end{bmatrix} \begin{bmatrix} I_1 \\ I_2 \\ I_3 \end{bmatrix} \tag{2.78}$$

Solve for I_3 in terms of I_2:

$$I_3 = \frac{j\omega L_m}{R_2 + R_L + j\omega(L_2 - L_m) - \frac{j}{\omega C_2}} I_2 \tag{2.79}$$

Insert (2.79) into (2.76):

$$\frac{I_1}{j\omega C_1} = \left(X_{C1} + R_1 + j\omega(L_1 - L_m)\right) I_2 - j\omega L_m I_3$$

$$= \left(\frac{1}{j\omega C_1} + R_1 + j\omega(L_1 - L_m) + \frac{\omega^2 L_m^2}{R_2 + R_L + j\omega(L_2 - L_m) - \frac{j}{\omega C_2}} \right) I_2 \tag{2.80}$$

Express I_2 in terms of I_1:

$$I_2 = \frac{1/j\omega C_1}{\frac{1}{j\omega C_1} + R_1 + j\omega(L_1 - L_m) + \frac{\omega^2 L_m^2}{R_2 + R_L + j\omega(L_2 - L_m) - \frac{j}{\omega C_2}}} I_1$$

$$= \frac{j\omega C_1}{j\omega C_1 + \frac{1}{R_1 + j\omega(L_1 - L_m) + \frac{\omega^2 L_m^2}{R_2 + R_L + j\omega(L_2 - L_m) - \frac{j}{\omega C_2}}}} I_1 \tag{2.81}$$

Insert (2.81) into (2.74) and solve for Z_{IN}:

$$V_1 = X_{C1} I_1 - X_{C1} I_2$$

$$= \frac{1}{j\omega C_1} I_1 - \frac{1}{j\omega C_1} \left(\frac{j\omega C_1}{j\omega C_1 + \frac{1}{R_1 + j\omega(L_1 - L_m) + \frac{\omega^2 L_m^2}{R_2 + R_L + j\omega(L_2 - L_m) - \frac{j}{\omega C_2}}}} \right) I_1$$

(2.82)

$$Z_{IN} = \frac{V_1}{I_1} = 1 - \frac{1}{j\omega C_1 + \dfrac{1}{R_1 + j\omega(L_1 - L_m) + \dfrac{\omega^2 L_m^2}{R_2 + R_L + j\omega(L_2 - L_m) - \dfrac{j}{\omega C_2}}}} \tag{2.83}$$

Turning our attention now to power transfer efficiency, we start with (3.84).

$$\eta_{PS} = \frac{P_{OUT}}{P_{IN}} = \frac{|I_3|^2 R_L}{|I_2|^2 R_1 + |I_3|^2 R_2 + |I_3|^2 R_L} = \frac{|I_3|^2 R_L}{|I_2|^2 R_1 + |I_3|^2 (R_2 + R_L)} \tag{2.84}$$

In order to isolate $|I_3|^2$ within (2.84) denominator so that they may cancel, we simply manipulate (2.79) by taking the absolute value and squaring both sides. Doing this gives us:

$$|I_3| = \frac{\omega L_m}{R_2 + R_L + \omega(L_2 - L_m) + \dfrac{1}{\omega C_2}} |I_2| \tag{2.85}$$

$$|I_3|^2 = \frac{\omega^2 L_m^2}{\left(R_2 + R_L + \omega(L_2 - L_m) + \dfrac{1}{\omega C_2}\right)^2} |I_2|^2 \tag{2.86}$$

Considering optimal power transfer efficiency takes place at resonance, we insert (2.34) into (2.86). Considering also that both compensation capacitors have been chosen appropriately such that all reactive power tends to zero, (2.86) becomes:

$$|I_3|^2 = \frac{\omega^2 L_m^2}{\left(R_2 + R_L + 2\omega_0(L_2 - L_m)\right)^2} |I_2|^2 \tag{2.87}$$

Inserting this result back into (2.84) and simplifying gives:

$$\eta_{PS} = \frac{R_L}{\dfrac{R_1\left(R_2 + R_L + 2\omega_0(L_2 - L_m)\right)^2}{\omega_0^2 L_m^2} + R_2 + R_L} \tag{2.88}$$

Finally, by inspection of (2.88) it can be seen that as $\frac{R_1\left(R_2+R_L+2\omega_0(L_2-L_m)\right)^2}{\omega_0^2 L_m^2} \rightarrow 0$ that the expression can be simplified. It is obtained when the following condition holds:

$$\omega_0 \gg \frac{\sqrt{R_1\left(R_2+R_L+2\omega_0(L_2-L_m)\right)^2}}{L_m} \tag{2.89}$$

When the condition in (2.89) is met, (2.88) becomes:

$$\eta_{PS\_MAX} = \frac{R_L}{R_2+R_L} \tag{2.90}$$

2.1.4.4 Parallel-Parallel (PP)

Figure 2.11 shows the schematic diagram for PP topology. Notice that both capacitors on T_X (primary) and R_X (secondary) sides are in parallel with L_1 and L_2. R_1 and R_2 are the internal dc resistance(s) for both L_1 and L_2, respectively, and R_L is the load resistance.

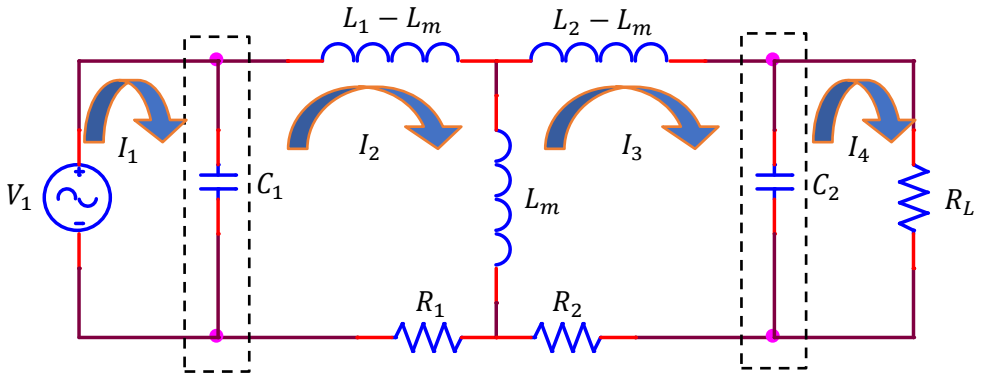

Figure 2.11: Schematic diagram for PP-Topology equivalent model

With this topology there are four mesh equations with the voltage at the source being the same as the voltage across C_1 and the fourth current flowing between C_2 and R_L. We start the analysis like any other circuit using Kirkoff's Laws.

$$V_1 = X_{C1}I_1 - X_{C1}I_2 \tag{2.91}$$

$$X_{C1}(I_1 - I_2) + j\omega(L_1 - L_m)I_2 + R_1I_2 - j\omega L_mI_3 = 0 \tag{2.92}$$

$$X_{C1}I_1 = (X_{C1} + j\omega(L_1 - L_m) + R_1)I_2 - j\omega L_mI_3 \tag{2.93}$$

$$j\omega L_mI_2 = j\omega(L_2 - L_m)I_3 + R_2I_3 + X_{C2}(I_3 - I_4) \tag{2.94}$$

$$j\omega L_mI_2 = (j\omega(L_2 - L_m) + R_2 + X_{C2})I_3 - X_{C2}I_4 \tag{2.95}$$

$$X_{C2}(I_4 - I_3) + R_LI_4 = 0 \tag{2.96}$$

$$(X_{C2} + R_L)I_4 - X_{C2}I_3 = 0 \tag{2.97}$$

Equations (2.91) – (2.97) are the mesh equations based on analysis of Figure 2.11. Expanding these equations out and summarizing in matrix form reduces to (2.98).

$$\begin{bmatrix} V_1 \\ 0 \\ 0 \\ 0 \end{bmatrix} = \begin{bmatrix} -\frac{j}{\omega C_1} & \frac{j}{\omega C_1} & 0 & 0 \\ \frac{j}{\omega C_1} & -\frac{j}{\omega C_1} + j\omega(L_1 - L_m) + R_1 & -j\omega L_m & 0 \\ 0 & -j\omega L_m & -\frac{j}{\omega C_1} + j\omega(L_1 - L_m) + R_1 & \frac{j}{\omega C_2} \\ 0 & 0 & \frac{j}{\omega C_2} & R_L - \frac{j}{\omega C_2} \end{bmatrix} \begin{bmatrix} I_1 \\ I_2 \\ I_3 \\ I_4 \end{bmatrix} \tag{2.98}$$

Solve for I_4 in terms of I_3 using (2.97):

$$I_3 = \frac{X_{C2} + R_L}{X_{C2}} I_4 \rightarrow I_4 = \frac{X_{C2}}{X_{C2} + R_L} I_3 \tag{2.99}$$

Insert (2.99) into (2.95):

$$j\omega L_mI_2 = (j\omega(L_2 - L_m) + R_2 + X_{C2})I_3 - X_{C2}\left(\frac{X_{C2}}{X_{C2} + R_L}\right)I_3$$

$$= \left[j\omega(L_2 - L_m) + R_2 + X_{C2} + \frac{1}{\omega^2 C_2^2}\left(\frac{1}{X_{C2} + R_L}\right)\right]I_3 \tag{2.100}$$

Solve for I_3 in terms of I_2 using (2.100):

$$I_3 = \frac{j\omega L_m}{j\omega(L_2 - L_m) + R_2 + X_{C2} + \frac{1}{\omega^2 C_2^2}\left(\frac{1}{X_{C2} + R_L}\right)} I_2 \tag{2.101}$$

Insert (2.101) into (2.93) and isolate I_1:

$$X_{C1} I_1 = X_{C1} + j\omega(L_1 - L_m) + R_1 + \frac{\omega^2 L_m^2}{j\omega(L_2 - L_m) + R_2 + X_{C2} + \frac{1}{\omega^2 C_2^2}\left(\frac{1}{X_{C2} + R_L}\right)} I_2 \tag{2.102}$$

$$I_1 = \frac{j\omega C_1}{j\omega C_1 + \frac{1}{j\omega(L_1 - L_m) + R_1 + \frac{\omega^2 L_m^2}{j\omega(L_2 - L_m) + R_2 + X_{C2} + \frac{1}{\omega^2 C_2^2}\left(\frac{1}{X_{C2} + R_L}\right)}}} I_2$$

$$\leftrightarrow$$

$$I_2 = \frac{1}{\frac{j\omega C_1}{j\omega C_1 + \frac{1}{j\omega(L_1 - L_m) + R_1 + \frac{\omega^2 L_m^2}{j\omega(L_2 - L_m) + R_2 + X_{C2} + \frac{1}{\omega^2 C_2^2}\left(\frac{1}{X_{C2} + R_L}\right)}}}} I_1 \tag{2.103}$$

Insert (2.103) into (2.91) and solve for Z_{IN}:

$$Z_{IN} = \frac{V_1}{I_1} = X_{C1} - \frac{1}{j\omega C_1 + \frac{1}{j\omega(L_1 - L_m) + R_1 + \frac{\omega^2 L_m^2}{j\omega(L_2 - L_m) + R_2 + X_{C2} + \frac{1}{\omega^2 C_2^2}\left(\frac{1}{X_{C2} + R_L}\right)}}} \tag{2.104}$$

Equation (2.104) is the impedance as seen by the source for PP-topology. Taking the complex conjugate of this expression, setting the imaginary components equal to zero we can solve for the

primary capacitance that will ensure that the primary side is balanced, and all reactive power tends to zero. This brings the power factor to unity as desired. Power transfer efficiency for this topology is given by (2.105).

$$\eta_{PP} = \frac{P_{OUT}}{P_{IN}} = \frac{|I_4|^2 R_L}{|I_2|^2 R_1 + |I_3|^2 R_2 + |I_4|^2 R_L} \tag{2.105}$$

The strategy is to cancel out $|I_4|^2$ in both the numerator and denominator. We start with (2.99), taking the absolute value, and squaring it. We then use the result to simplify (2.105).

$$I_3 = \frac{X_{C2} + R_L}{X_{C2}} I_4 = (1 + j\omega C_2 R_L) I_4 \tag{2.106}$$

$$|I_3|^2 = (1 + \omega C_2 R_L)^2 |I_4|^2 \tag{2.107}$$

$$\eta_{PP} = \frac{|I_4|^2 R_L}{|I_2|^2 R_1 + |I_4|^2 (R_2 (1 + \omega C_2 R_L)^2 + R_L)} \tag{2.108}$$

To express I_2 in terms of I_4 we utilize (2.95) by first inserting (2.106) and simplifying. When doing this, we arrive at (2.109). Subsequently we also preform the additional steps.

$$j\omega L_m I_2 = (j\omega (L_2 - L_m) + R_2 + X_{C2})(1 + j\omega C_2 R_L) I_4 - X_{C2} I_4 \tag{2.109}$$

$$I_2 = \frac{(j\omega (L_2 - L_m) + R_2 + X_{C2})(1 + j\omega C_2 R_L) - X_{C2}}{j\omega L_m} I_4 \tag{2.110}$$

$$|I_2|^2 = \frac{\left[\left(\omega (L_2 - L_m) + R_2 + \frac{1}{\omega C_2}\right)(1 + \omega C_2 R_L) - \frac{1}{\omega C_2}\right]^2}{\omega^2 L_m^2} |I_4|^2 \tag{2.111}$$

Inserting (2.111) into (2.108):

$$\eta_{PP} = \frac{R_L}{R_1 \frac{\left[\left(\omega (L_2 - L_m) + R_2 + \frac{1}{\omega C_2}\right)(1 + \omega C_2 R_L) - \frac{1}{\omega C_2}\right]^2}{\omega^2 L_m^2} + R_2 (1 + \omega C_2 R_L)^2 + R_L} \tag{2.112}$$

When the term $\frac{\left[\left(\omega(L_2-L_m)+R_2+\frac{1}{\omega C_2}\right)(1+\omega C_2 R_L)-\frac{1}{\omega C_2}\right]^2}{\omega_0^2 L_m^2} \rightarrow 0$, the following condition is true:

$$\omega_0 \gg \frac{\sqrt{R_1\left[\left(\omega(L_2-L_m)+R_2+\frac{1}{\omega C_2}\right)(1+\omega C_2 R_L)-\frac{1}{\omega C_2}\right]^2}}{L_m} \tag{2.113}$$

Consequently, because of (2.113), (2.112) reduces to the maximum peak value of:

$$\eta_{PP\_MAX} = \frac{R_L}{R_2(1+\omega C_2 R_L)^2 + R_L} = \frac{R_L}{R_2\left(1+\frac{R_L}{\omega_0(L_2-L_m)}\right)^2 + R_L} \tag{2.114}$$

2.2 Important Observations and Important Performance Parameters

Equations (2.53), (2.70), (2.88), and (2.112) are the expressions for power transfer efficiency for all four network topologies. When the input impedance as seen by the source (Z_{IN}) is purely resistive this condition means all the reactive components are eliminated or small enough to be ignored; power integrity is optimized with a very small amount of insertion loss ($S_{11} \approx -\infty\ dB$). It also ensures that maximum power transfer can occur or that the return loss is near zero ($S_{21} \approx 0\ dB$). This is the purpose for capacitive compensation which is to balance the inductive reactance already present from L_1, L_2, and L_m with capacitive reactance effectively canceling out all reactive components in the system at a predefined resonance frequency in order to maintain good power integrity.

It is also important to observe that L_m plays a critical role in governing a balanced system along with capacitive compensation. When the value of L_m changes it can introduce undesired reactance into the system in the same way that the wrong compensation capacitance can by offsetting reactance – inductive reactance, in this case. As Figure 2.6 indicated along with the mathematical derivation of equation (2.30), there is a direct dependence of L_m on the separation

distance (g) between L_1 and L_2. This means that changing g in µWPT systems will impact L_m and thus the reactance of the overall balance in the system. Finding this optimal value of g for each network topology therefore becomes critical in terms of system performance. It is for this reason that the focus turns to performing ADS simulations on each network topology in order to find these optimized conditions, compare each topology to each other highlighting the advantages and disadvantages of each one and then identifying the best performing topology for µWPT systems.

CHAPTER 3
Simulations for μWPT Network Topologies

Simulating the four topologies will serve two purposes. The first purpose is to validate the mathematical derivations obtained in Chapter 2 and the second purpose is to identify in more detail the advantages and disadvantages of each topology. The end goal of this chapter is to fully understand why one topology would be used over another based on the needs of a given application while comparing them to what the theory in the last chapter has revealed about them.

3.1 ADS Simulations and Analysis

In all four cases, the simulation setup and approach will be the same for all topologies. Advanced System Design (ADS) will be the primary simulation software used which will model S-parameters and input impedance. Specifically, the two most critical S-parameters in this case are S_{11} and S_{21}. These two parameters will be scaled according to equations 3.1 and 3.2.

$$\eta_{11} = |S_{11}|^2 \times 100\% \tag{3.1}$$

$$\eta_{21} = |S_{21}|^2 \times 100\% \tag{3.2}$$

As indicated in Chapter 2, the goal is to minimize η_{11} and to maximize η_{21}. Recall the discussion from Section 2.2 on capacitive compensation and the importance of using the correct values of capacitance which can be calculated as was done in detail in the previous chapter. There are two functions within ADS that will help us in this endeavor which is the tuning and optimization features. They will allow more control over the circuit parameters during the analysis that will help determine how η_{11} and η_{21} change as certain other parameters change, which, ultimately, will help reveal critical differences between the four topologies in the process of accomplishing our goal. In addition to this, it is important to point out that there may be impedance mismatches between $Term1$ and $Term2$ in the process of tuning each circuit topology for the

optimal power transfer condition. If these simulations where to be validated with measurements within a lab using a VNA, impedance re-normalization techniques may be required in order to match both terminations to be the same as the VNA port impedance. There are numerous papers on such re-normalization techniques [47], [48], and [49].

3.1.1 Power Transfer Efficiency and Separation Distance

In addition to optimizing η_{11} and η_{21}, a relationship between η_{21} – the power transfer efficiency – and the separation distance or air gap, g, between L_1 and L_2 will be established. This is accomplished by changing the coupling coefficient, k, value in the process of tuning the circuit values in each simulation iteration and then tabulating the data. Equations (2.31) and (2.32) establish the relationship between k and L_m and applying the Neumann formula obtained in (2.30) – which was plotted in Section 2.1.3 – establishes the desired relationship between η_{21} and g. This is a critical parameter in the design of NMC power connectors. While the impact of vertical, lateral, and angular misalignment problems are not really problems for NMC power connectors, there will be tolerance variations in the housing molds that are designed that fixture L_1 and L_2. The tolerance variation will have slight impacts on the otherwise axial alignment between both inductors which will consequently have a very slight impact on power transfer efficiency.

3.1.2 Circuit Parameters and ADS Topology Models

For each of the four compensation topologies, certain circuit parameters will be the same. Both L_1 and L_2 will have the same value of $L_1 = L_2 = 24\ \mu H$, and will make simulations much easier with one less dependent variable. In all four cases, the internal parasitic resistance for both inductors will also be held constant at $R_1 = R_2 = 1\ \Omega$. In the process of tuning and optimizing, it can be useful to also tune one of these inductors in order to help eliminate reactive power in the primary and reduce the power factor to unity. However, equations (2.53), (2.70), (2.88), and

(2.112) in all four topologies reveal that this is can be done by calculating the primary capacitance after first selecting a resonance frequency for the secondary capacitance that is based on equations (2.33) and (2.34). They apply in all four cases. What determines the selected frequency is based on the specific application industry. For example, in the consumer electronics industry and for WPT systems, the Qi standard is the governing standard in accordance with the wireless power consortium. For this standard, the frequency range is from $95\,kHz \leq f_0 \leq 200\,kHz$ with a nominal frequency of $f_0 = 125\,kHz$. In this chapter and for the following simulations, this is the frequency that will be used.

3.2 ADS Simulations and Analysis of SS-Topology

This section focuses on SS-Topology. As the name implies, Series-Series (SS) Topology means that the primary capacitance is in series with L_1 and the secondary compensation capacitance is in series with L_2. Figure 3.1 shows the ADS circuit setup for SS topology. For this topology, attention will be on the input termination ($Term1$), the output termination ($Term2$) and coupling coefficient which can all impact the system performance. Both terminations will be equal due to system symmetry and they along with k will act as the independent variables with S_{11}, S_{21} and Z_{IN} as the dependent variables.

ADS has a useful tuning feature. If we know both self-inductance for each inductor, and the frequency we can tune the circuit parameters that matter most for design. These parameters are the Z_{IN}, the load, and ultimately the separation distance between L_1 and L_2.

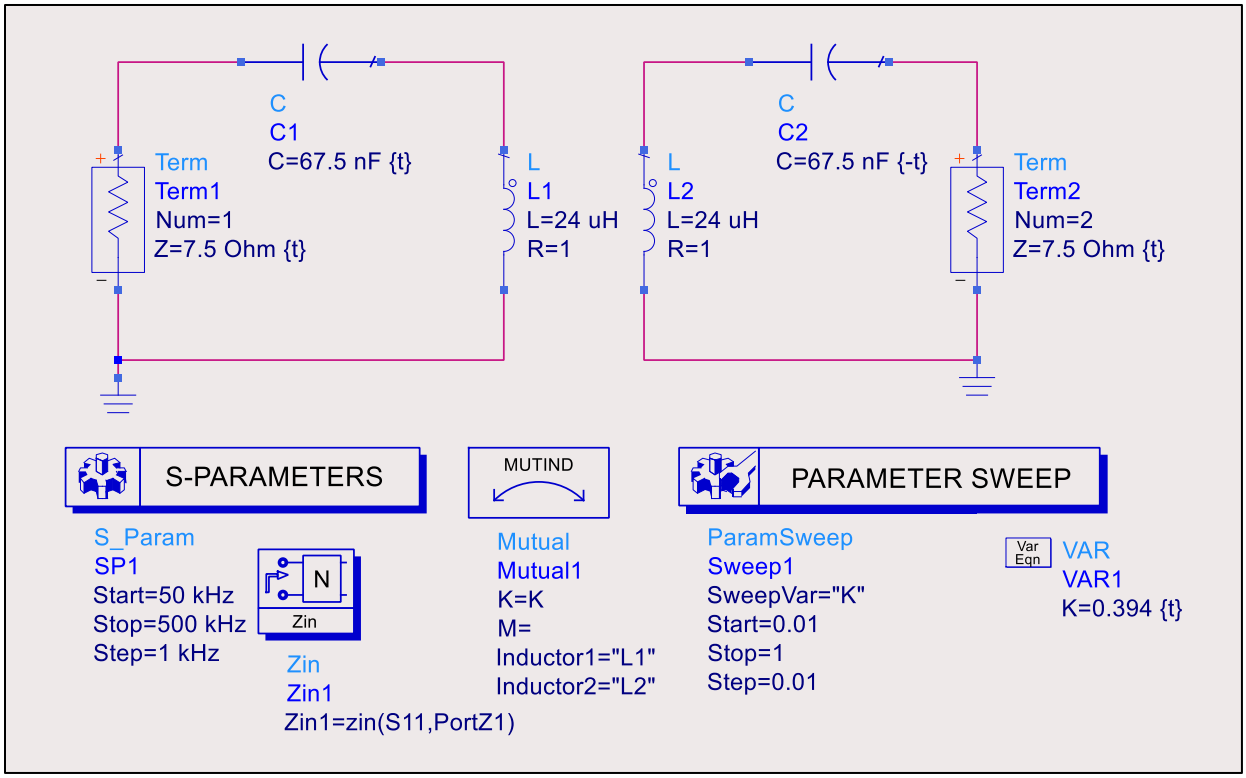

Figure 3.1: ADS circuit configuration and setup for SS-Topology

Table 3.1 is a summary of simulation runs for the setup shown in Figure 3.1. What does this data tell us about the system? When both termination resistances are changed as shown in the first two columns of Table 3.1, the coupling coefficient is adjusted or "tuned" so as to optimize η_{11} and η_{21} for a set $f_0 = 125\ kHz$. The goal is to optimize so that η_{11} is the lowest value possible.

Table 3.1: Summary Data for SS-Topology

$\boldsymbol{Term1}$ [Ω]	$\boldsymbol{Term2}$ [Ω]	$\boldsymbol{k}$	$\boldsymbol{\eta_{11}}$ [%]	$\boldsymbol{\eta_{21}}$ [%]	$\boldsymbol{\lvert Z_{in}\rvert}$ [Ω]
2.50	2.50	0.122	0.265	65.64	2.511
3.50	3.50	0.177	0.197	74.59	3.488
5.00	5.00	0.260	0.054	81.83	5.003
6.00	6.00	0.313	0.100	84.71	5.989
7.50	7.50	0.394	0.077	87.69	7.489
8.50	8.50	0.447	0.063	89.12	8.49
10.0	10.0	0.527	0.147	90.75	9.971
12.5	12.5	0.666	0.203	92.59	12.67
15.0	15.0	0.807	1.517	93.63	15.46
17.5	17.5	0.960	0.382	94.57	18.70
20.0	20.0	1.000	0.609	94.68	17.91

There are a few other considerations. The primary consideration is the separation distance between L_1 and L_2 which is positively correlated with the coupling coefficient k. In design, it is desirable to have the lowest k-value in order to give the designer more distance margin. We can see from the data that the benefit in performance gains start to plateau after the fifth run (Table 3.1) when $\eta_{21} = 87.69\%$. After this, subsequent runs show very little gains in efficiency at the expense of distance margin and increases in impedance. Therefore, this will be the best design choice which we will now look at a little more closely.

Figures 3.2 and 3.3 show that the input impedance as seen by the source stays constant at around $5.5\ \Omega$ with very little insertion loss. Power transfer efficiency from to the load stays above 85% for $116\ kHz \leq f_0 \leq 151\ kHz$ which is within the Qi specification and meets the requirements for the wireless power consortium. Over this same frequency range, Figure 4.3 shows that the input impedance stays below $10\ \Omega$. This is what a separation distance margin for a k-value of 0.394 would allow. It turns out that we really cannot optimize beyond this point with the independent variable parameters set. Adjusting the k-value a little higher or lower outside this optimized point reduces the efficiency and the data in Table 3.1 shows insertion loss increasing after both terminations are higher than $8.5\ \Omega$.

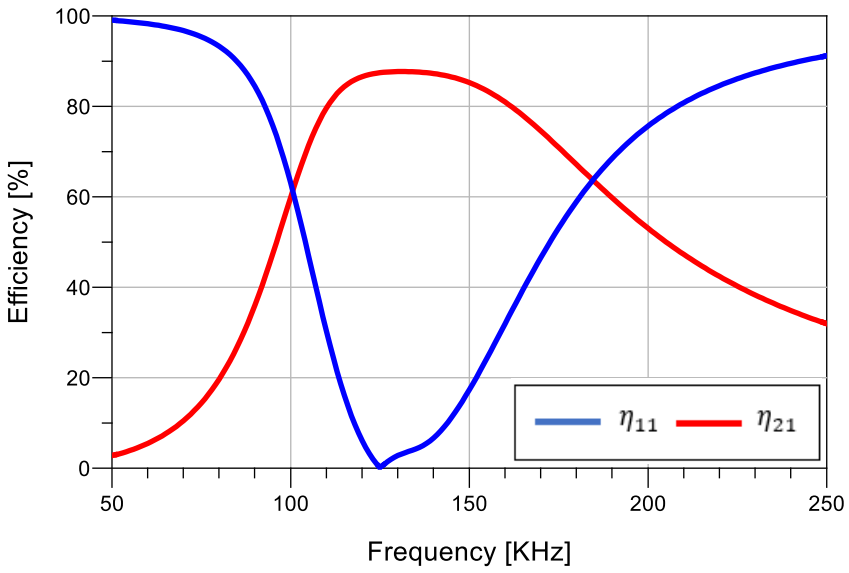

Figure 3.2: SS-Topology best performance plot for η_{11} and η_{21}

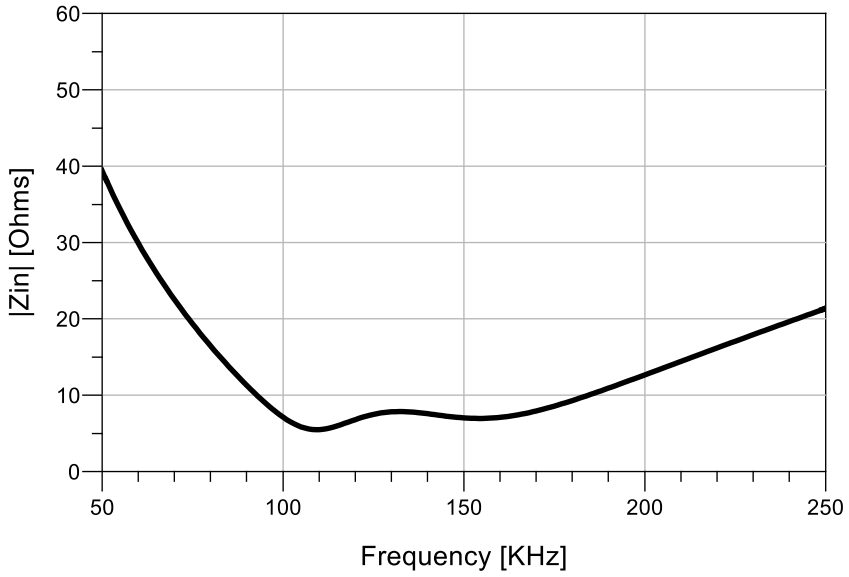

Figure 3.3: SS-Topology best input impedance plot for third run

This implies that for any impedance at the source termination or the load there is a sweet spot for optimal power transfer efficiency. In the real world that translates to there being a fixed and optimal separation distance between L_1 and L_2 that gives rise to the optimal power transfer

efficiency. Adjusting that separation distance just a little in either direction will negatively impact efficiency. Figure 3.4 plots the data in Table 3.1 for η_{21} verses k.

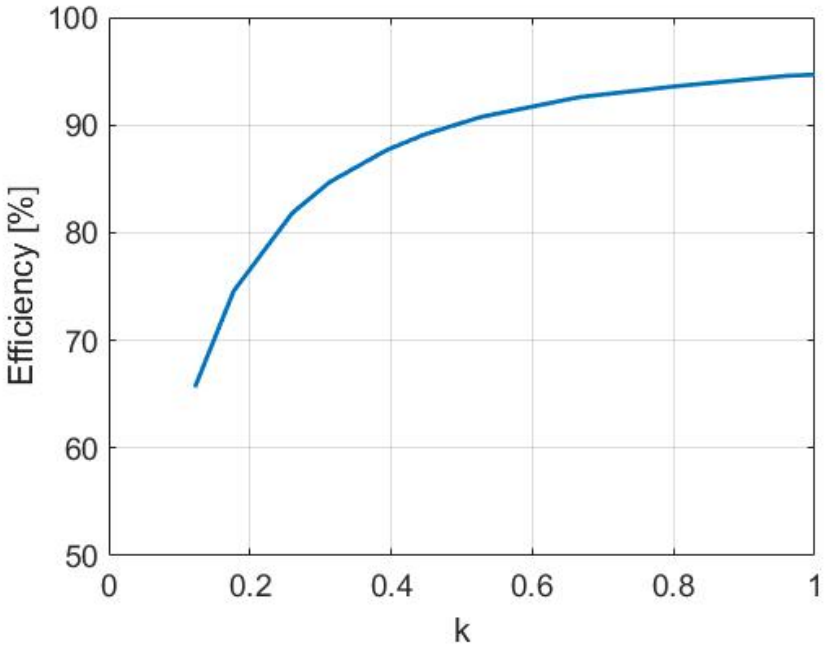

Figure 3.4: MATLAB plot of Table 3.1 of η_{21} verses k for SS-Topology

3.3 ADS Simulations and Analysis of SP Topology

This section focuses on SP-Topology. As the name implies, Series-Parallel (SP) Topology means that the primary capacitance is in series with L_1 and the secondary compensation capacitance is in parallel with L_2. All ADS simulation runs for SP-Topology that was done in section 3.2 for SS-Topology. With all parameters fixed from our investigation of SS-Topology, this study also looks at how SP-Topology operates over the same frequency range in accordance with Qi standards. Therefore, the frequency range is from $95\ kHz \leq f_0 \leq 200\ kHz$ with the nominal frequency at $f_0 = 125\ kHz$.

Figure 3.5 shows the ADS circuit setup. In this case, the input termination ($Term1$) and output termination ($Term2$) and coupling coefficient all impact the system performance. The

output termination – representing the load impedance – is held fixed at $Term2 = 200\ \Omega$. $Term1$, k, and C_1 are the independent variables that S_{11}, S_{21}, and Z_{IN} depend on.

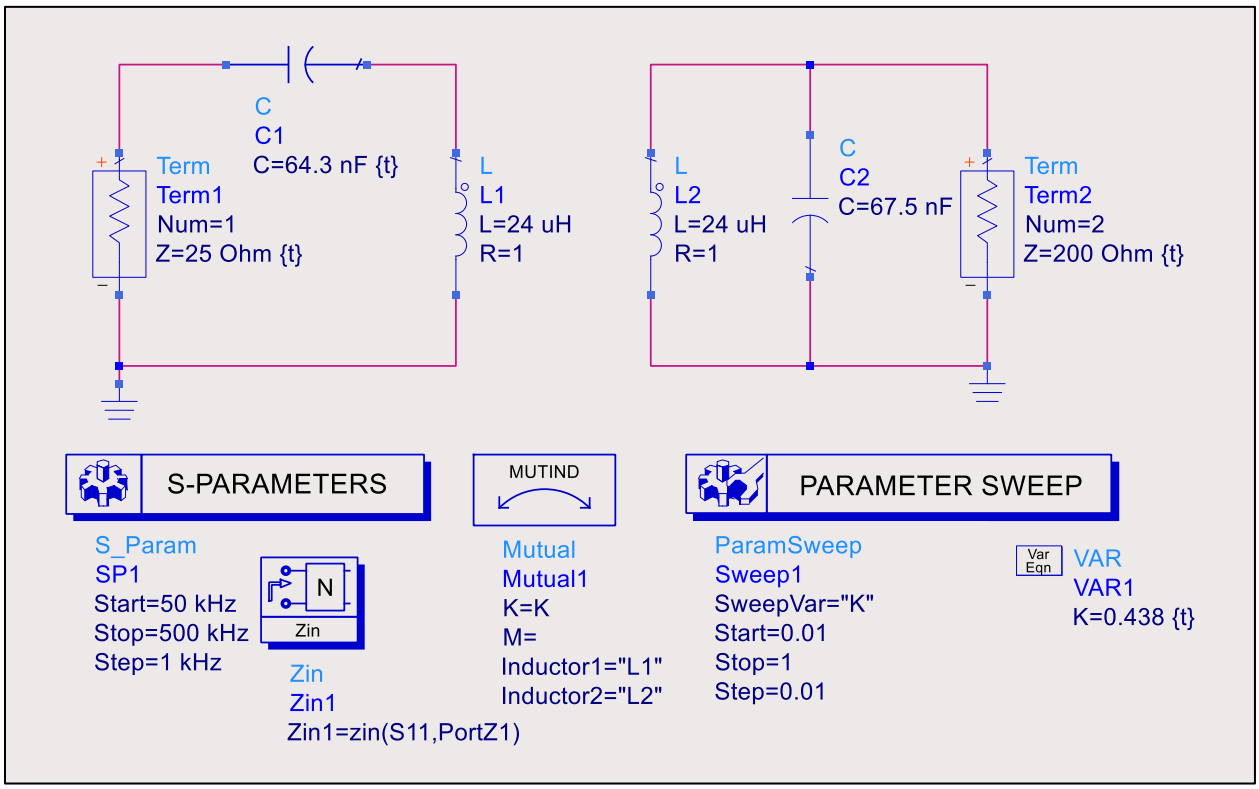

Figure 3.5: ADS circuit configuration and setup for SP-Topology

Using the tuning function in ADS we are able to obtain the optimal performance for a given set of fixed parameters. For example, if we know both self-inductance for each inductor, the frequency (and thus compensation capacitance values) we can tune the circuit parameters that matter most for design. These parameters are the input impedance, primary capacitance, and ultimately the separation distance between L_1 and L_2. Table 3.2 is a summary of simulation runs for the setup shown in Figure 3.5. What does this data tell us about the system? When the input termination resistance and primary capacitance values are adjusted or "tuned" as shown in the first and fourth columns of Table 3.2, η_{11} and η_{21} are optimized for best performance over the target frequency range. This was done and over a range of values shown in the first four columns of

Table 3.2. There is not much more additional benefit in terms of performance after the 6th run when $Term1 = 25\,\Omega$. η_{21} makes very little additional performance gains in subsequent iterations. Therefore, this is the value that best optimizing performance for a fixed load impedance for SP-Topology.

Table 3.2: Summary Data for SP-Topology

$\boldsymbol{Term1}$ [Ω]	$\boldsymbol{Term2}$ [Ω]	$\boldsymbol{k}$	$\boldsymbol{C_1}$ $[\boldsymbol{nF}]$	$\boldsymbol{\eta_{11}}$ [%]	$\boldsymbol{\eta_{21}}$ [%]	$\lvert\boldsymbol{Z_{in}}\rvert$ [Ω]
2.50	200	0.108	67.4	0.333	61.93	2.328
5.00	200	0.189	67.1	0.336	72.32	5.620
7.50	200	0.228	67.4	0.058	74.57	7.725
10.0	200	0.268	67.0	0.153	75.98	10.32
12.5	200	0.303	66.5	0.131	76.83	12.94
25.0	200	0.438	64.3	0.078	78.54	26.10
50.0	200	0.626	60.4	0.053	79.38	52.56
75.0	200	0.769	56.9	0.027	79.66	79.07
100	200	0.890	53.8	0.031	79.80	105.5
125	200	1.000	50.9	0.361	79.89	133.0

Other observations from the data in Table 3.2 is that SP-Topology offers the advantage of more stability over that of SS-Topology. However, the power transfer efficiency is not as great by comparison. In addition, for the optimal performance values, the performance margin is not as wide meaning the frequency would need to be fixed $124\,kHz$ with very little room for error. Otherwise, η_{11} will increase sharply if the separation distance is changed in either direction by just a small amount. The data also reflects the dependence on primary capacitance values when secondary capacitance is chosen in advance. This fact reinforces the theoretical derivations from Chapter 2 indicating such dependence on C_1.We can also see from the data that for optimal performance, C_1 decreases in value as $Term1$ increases in value. This not only indicates an inverse relationship between these two parameters, but it also means that for SP-Topology, the primary side resonates at a higher frequency than the secondary side. A more general conclusion for SP-Topology is with the applications it would be ideal for. It is suitable for use in applications with a

fixed load impedance that is higher than the input termination impedance, the separation distance between L_1 and L_2 is fixed, and the operating frequency is finely tuned.

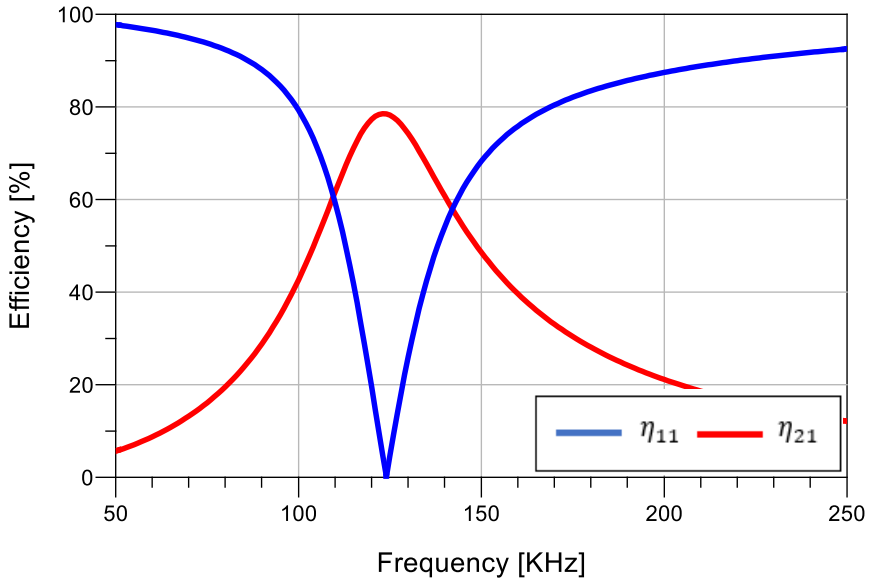

Figure 3.6: SP-Topology best performance plot for η_{11} and η_{21}

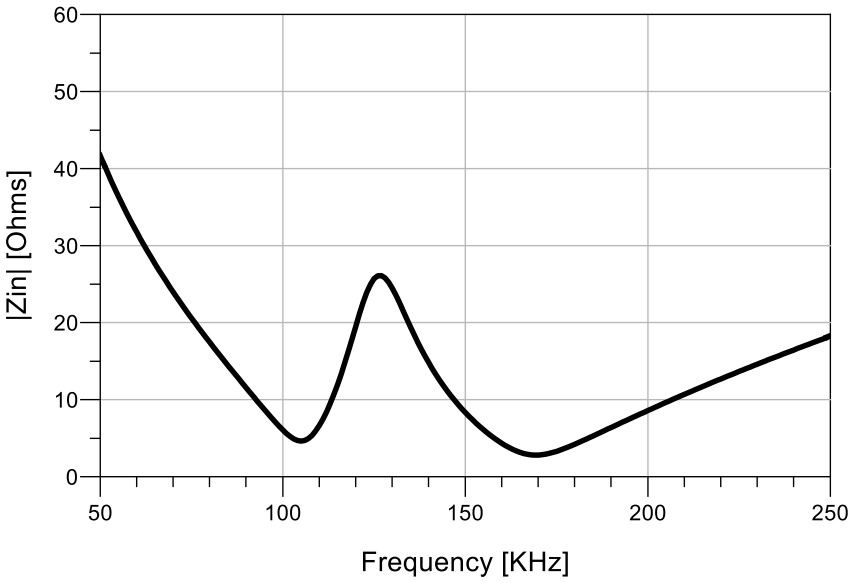

Figure 3.7: SP-Topology best input impedance plot for third run

From Figure 3.8 we can also make some conclusions about SP-Topology regarding separation distance between L_1 and L_2. Relative to SS-Topology, SP-Topology has its optimal performance at around the same k-value of about 0.4 but at a much lower power transfer efficiency value. The curve also flattens out much faster and in the real world that means not much additional power transfer efficiency gains are realized as the two inductors are physically moved closer to each other. The maximum optimized efficiency that can be realized with the set of parameters never goes above 80%.

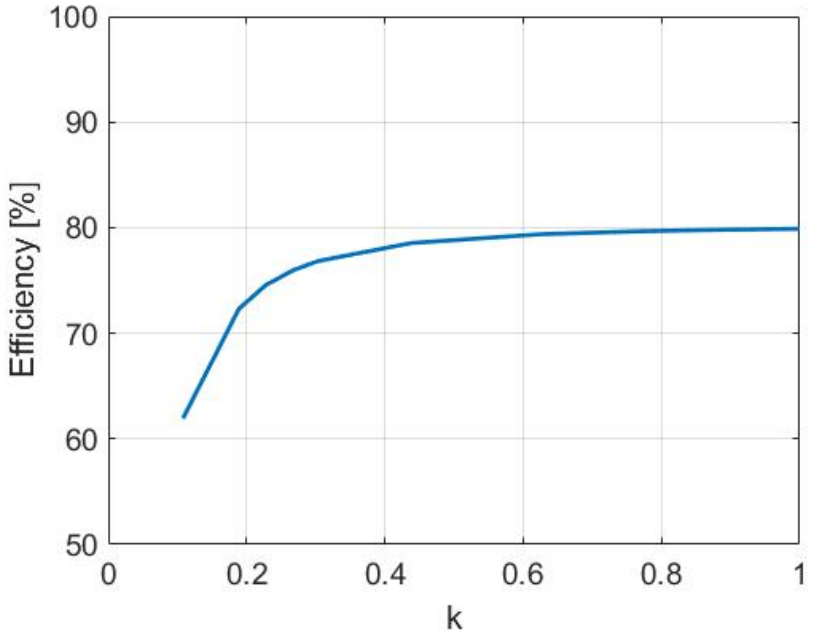

Figure 3.8: MATLAB plot of Table 4.2 of η_{21} verses k for SP-Topology

3.4 ADS Simulations and Analysis of PS Topology

This section focuses on PS-Topology. As the name implies, Parallel-Series (PS) Topology means that the primary capacitance is in parallel with L_1 and the secondary compensation capacitance is in series with L_2. With all parameters fixed from our investigation of SS-Topology and SP-Topology, this study also looks at how this topology differs relative to the others and the

unique characteristics that this topology offers. With an idea of what to already expect based on mathematical derivations, this system will also operate over the same frequency range in accordance with Qi standards meaning, like the other topologies, the nominal frequency is kept fixed at $f_0 = 125\ kHz$ for simulation runs.

Figure 3.9 shows the ADS circuit setup. In contrast to SP-Topology, in this case the input termination ($Term1$) fixed at 200 Ω, and the output termination ($Term2$) is varied along with the coupling coefficient (k), and primary capacitance (C_1). They will act as the independent variables. System performance is measured in terms of S-parameters, specifically S_{11} and S_{21}. The input impedance as seen by the source (Z_{IN}) is also studied as the three independent variables are changed. These will be the dependent variables.

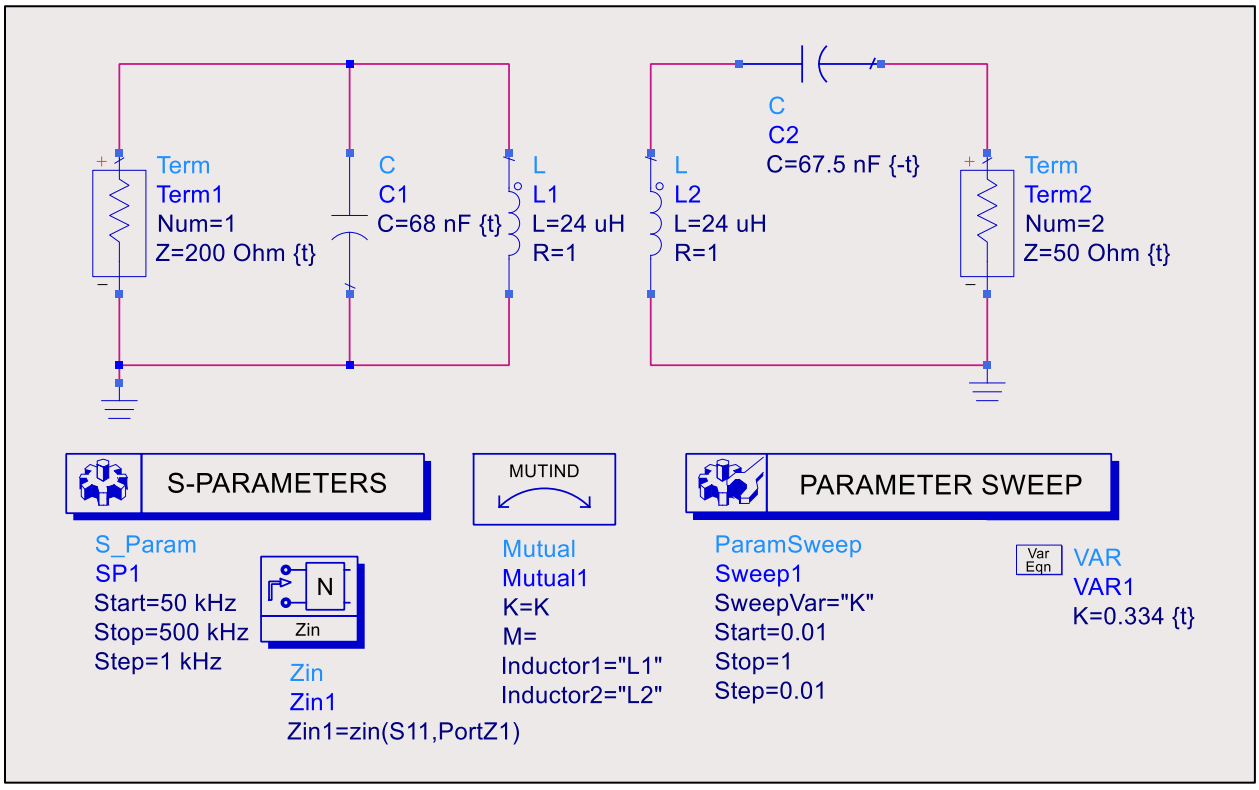

Figure 3.9: ADS circuit configuration and setup for PS-Topology

Table 3.3: Summary Data for PS-Topology

$Term1$ [Ω]	$Term2$ [Ω]	k	C_1 [nF]	η_{11} [%]	η_{21} [%]	$\lvert Z_{in}\rvert$ [Ω]
200	2.50	0.090	67.7	0.686	56.65	197.2
200	5.00	0.116	67.9	0.287	60.62	198.8
200	7.50	0.137	67.9	0.050	62.09	199.8
200	10.0	0.155	68.0	0.034	62.94	200.0
200	12.5	0.172	68.0	0.087	63.56	199.6
200	25.0	0.238	68.0	0.025	64.62	200.0
200	50.0	0.334	68.0	0.013	65.24	199.9
200	75.0	0.408	68.0	0.047	65.48	199.8
200	100	0.469	68.0	0.036	65.52	200.1
200	125	0.525	68.0	0.023	65.63	199.9
200	150	0.574	68.0	0.033	65.62	200.1
200	175	0.620	68.0	0.014	65.67	200.0
200	200	0.663	68.0	0.020	65.72	199.9
200	225	0.703	68.0	0.021	65.74	199.9
200	275	0.777	68.0	0.030	65.77	199.9
200	375	0.906	68.0	0.035	65.76	200.0

What does this data in Table 3.3 tell us about the system? Notice when the load termination resistance is changed as shown in the second column, the coupling coefficient and primary capacitance values are both adjusted or "tuned" so as to optimize η_{11} and η_{21} for a set frequency of $f_0 = 125\ kHz$. There are a few other observations. This data indicates that Z_{IN} is very stable no matter how the load changes. The load impedance can shift from being very low to very high as shown in the second column of Table 3.3, but that will have no impact on Z_{IN}The same can be said about changing the value of k. Along those same lines, another observation is the margin of k is not as volatile as it was in the previous three studied topologies meaning that no matter how it changes from 0 to 1, there is little impact on η_{21}. This also means that as L_m changes – or physically as g changes – there is little impact on η_{21}. In addition to this, the efficiency remains relatively flat after $Term2 = 50\ \Omega$. What these conclusions mean is unlike the previously studied topologies, the separation distance can change over a larger margin with very little impact on power transfer efficiency. The drawback from using this topology is the low efficiency, η_{21}. If an

application requires a high input termination, a high input impedance, has changing load demands, and requires a larger separation distance margin between L_1 and L_2, PS-Topology is the best choice. See Figures 3.10 and 3.11 for performance and impedance plots, respectively.

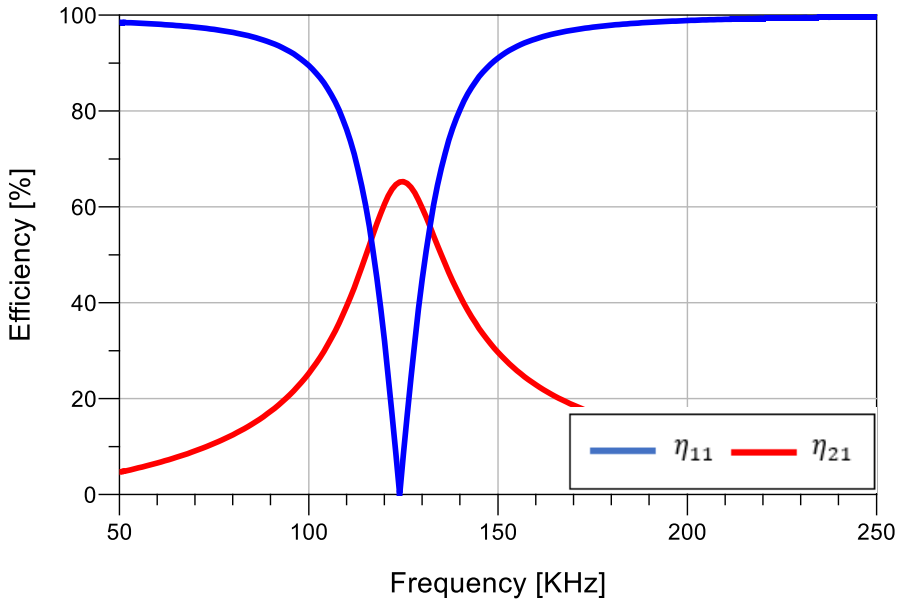

Figure 3.10: PS-Topology best performance plot for η_{11} and η_{21}

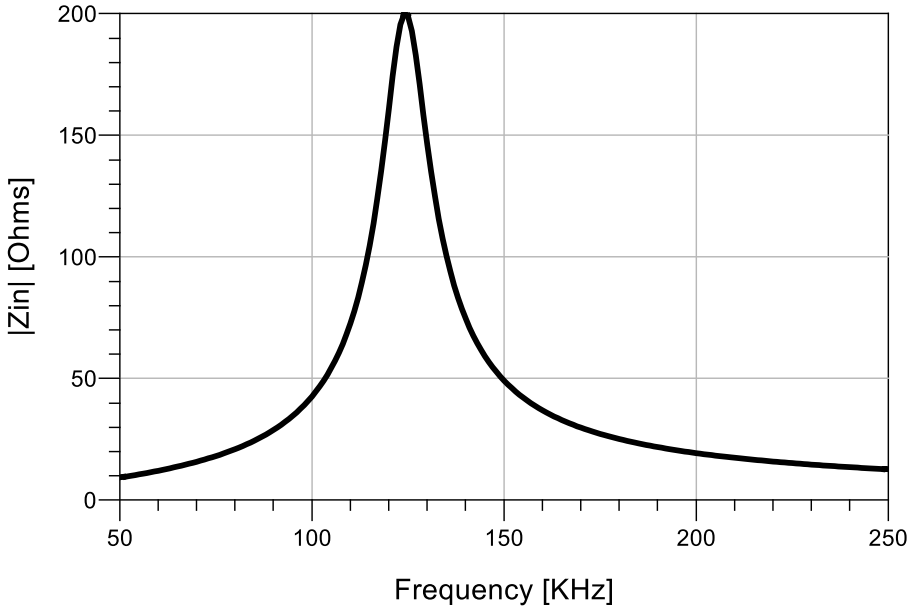

Figure 3.11: PS-Topology best input impedance plot for third run

From Figure 3.12 we can also make some conclusions about PS-Topology regarding separation distance between L_1 and L_2. Unlike the previous two topologies where the optimal performance value was around $k = 0.4$, PS-Topology has its optimal performance at around the same $k = 0.2$ and at this value has a much lower power transfer efficiency value. The curve also flattens out right after this value which, once again, in the real world that means not much additional power transfer efficiency gains are realized after this point as the two inductors are physically moved closer to each other. The maximum optimized efficiency that can be realized with the set of parameters never goes above 65% making it the least efficient topology, but by far the post stable.

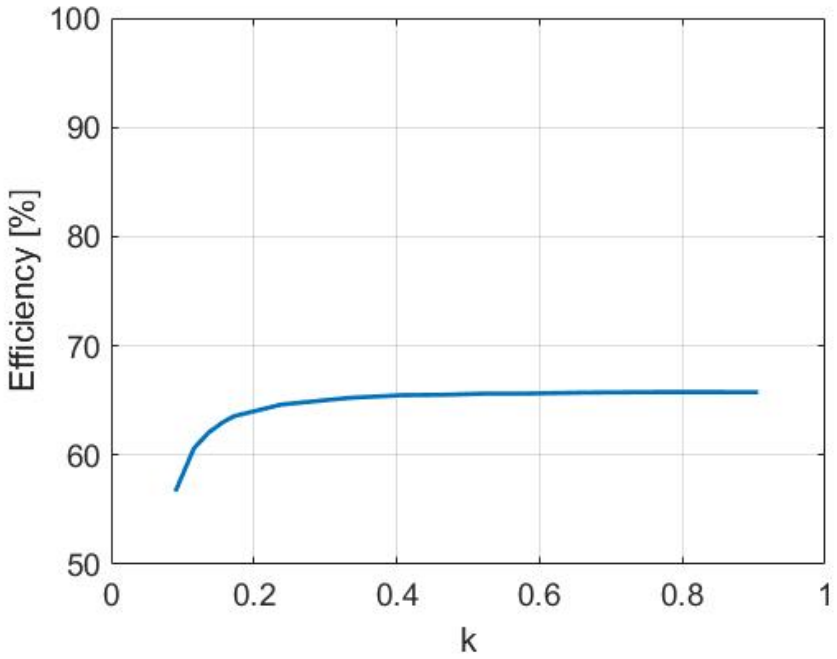

Figure 3.12: MATLAB plot of Table 3.3 of η_{21} verses k for PS-Topology

3.5 ADS Simulations and Analysis of PP Topology

This section focuses on PP-Topology. As the name implies, Parallel-Parallel (PP) Topology means that the primary capacitance is in parallel with L_1 and the secondary compensation capacitance is in parallel with L_2. With all parameters fixed from our investigation

of the previous three topologies, this section focuses on how PP-Topology differs. With an idea of what to already expect based on mathematical derivations, for comparison, this system will also operate over the same frequency range in accordance with Qi standards. Therefore, the nominal frequency is once again $f_0 = 125\ kHz$.

Figure 3.13 shows the ADS circuit setup. In this setup, both input termination ($Term1$) and output termination ($Term2$) is changed while in the process of tuning, the coupling coefficient (k), and primary capacitance (C_1) all impact the system performance and are also adjusted and tuned for optimal performance. They will act as the independent variables. As in the previous three sections, system performance is measured in terms of S-parameters, specifically S_{11} and S_{21}. The input impedance as seen by the source (Z_{IN}) is also studied as the three independent variables are changed. These will be the dependent variables.

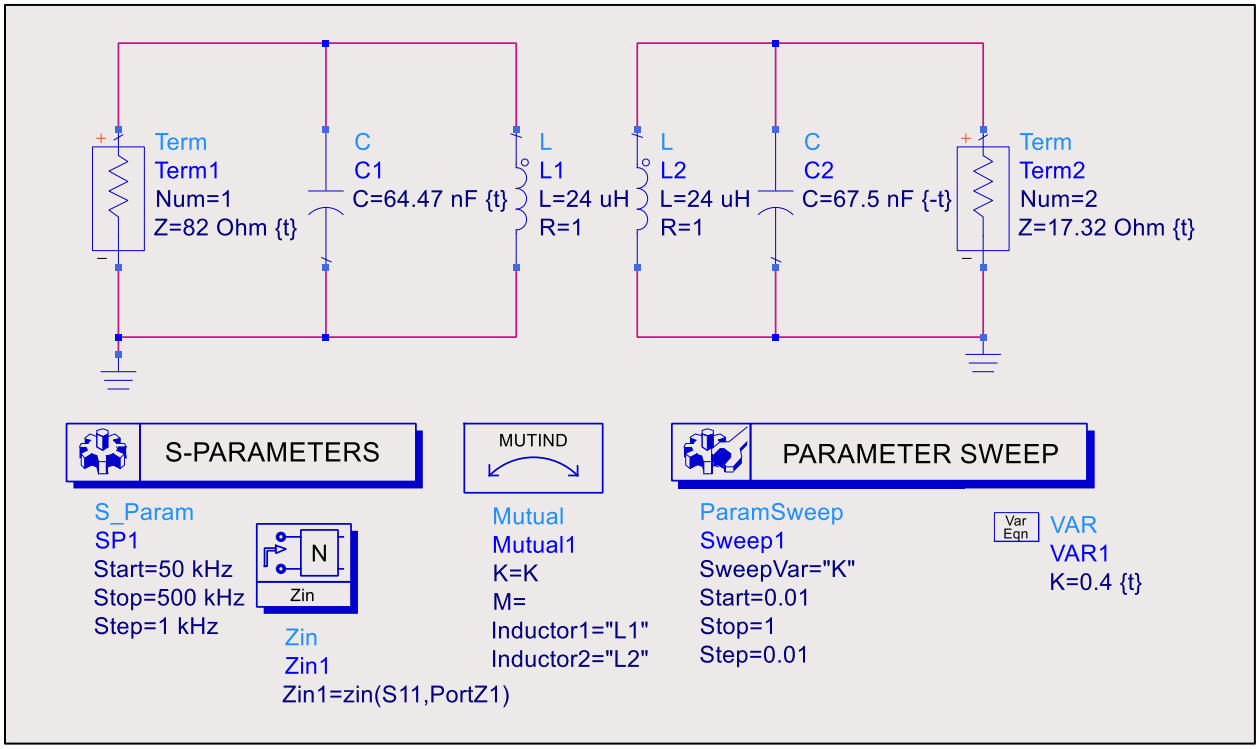

Figure 3.13: ADS circuit configuration and setup for PP-Topology

Table 3.4: Summary Date for PP-Topology

$Term1$ [Ω]	$Term2$ [Ω]	k	C_1 [nF]	η_{11} [%]	η_{21} [%]	$\lvert Z_{in}\rvert$ [Ω]
356.2	17.42	0.050	64.3	0.025	19.47	356.2
306.5	19.82	0.100	64.7	0.018	38.54	306.5
256.5	18.62	0.150	64.4	0.043	51.62	256.5
205.4	18.52	0.200	64.4	0.016	61.95	205.6
161.7	18.42	0.250	64.6	0.031	69.45	162.5
127.3	18.02	0.300	65.1	0.027	74.65	128.5
99.07	17.72	0.350	66.7	0.027	78.54	100.4
82.00	17.32	0.400	64.4	0.014	81.18	83.91
65.37	17.22	0.450	64.1	0.038	83.34	67.90
51.75	17.22	0.500	64.0	0.026	85.04	55.09
31.42	17.32	0.600	64.1	0.056	87.72	28.29
20.72	17.52	0.700	64.2	0.101	89.99	21.23
19.22	17.52	0.800	64.2	0.087	91.23	17.25
18.52	17.22	0.900	63.9	0.094	91.86	15.21
18.32	17.22	1.000	62.7	0.111	92.33	14.61

What does this data tell us about the system? When $Term1$ is changed as shown in the first column of Table 3.4, the coupling coefficient and primary capacitance values are both adjusted or "tuned" so as to optimize η_{11} and η_{21} for a set frequency of $f_0 = 125\ kHz$. The goal, as in the other sections, is to optimize so that η_{11} is the lowest value possible while using the tuning feature in ADS. There are a few other considerations. This data indicates that Z_{IN} is very stable no matter how $Term2$, but changes nearly exactly the same was as $Term1$. No matter how other parameters are adjusted, C_1 does not change much.

Another observation worth mentioning is this topology is very similar to SS-Topology in terms of how changes in k impact η_{21}. As k increases, so does η_{21}. One fundamental difference between SS-Topology and PP-Topology is how both $Term1$ and $Term2$ changes. With the former, both terminations are equal. In the later, $Term1$ is a high value and $Term2$ is a much lower value. Notice also that as $Term1 \rightarrow Term2$ while k increases in value, η_{21} also increases in value. If an application requires an input termination that is around 20Ω, but with very small separation distance between L_1 and L_2, then PP-Topology is the best choice. Figure 3.14 shows

that η_{21} has some tolerance while staying above 80%, while η_{11} has very little room for change and increases rapidly as separation changes in either direction (closer or further away from L_1 and L_2). Lastly, in order to realize the high efficiency gains shown in Table 3.4, k must be very high which physically means there is not much distance margin. Applications that require very small separation distances would do well with this topology, however, the power transfer efficiency goes down if larger distance margins are required.

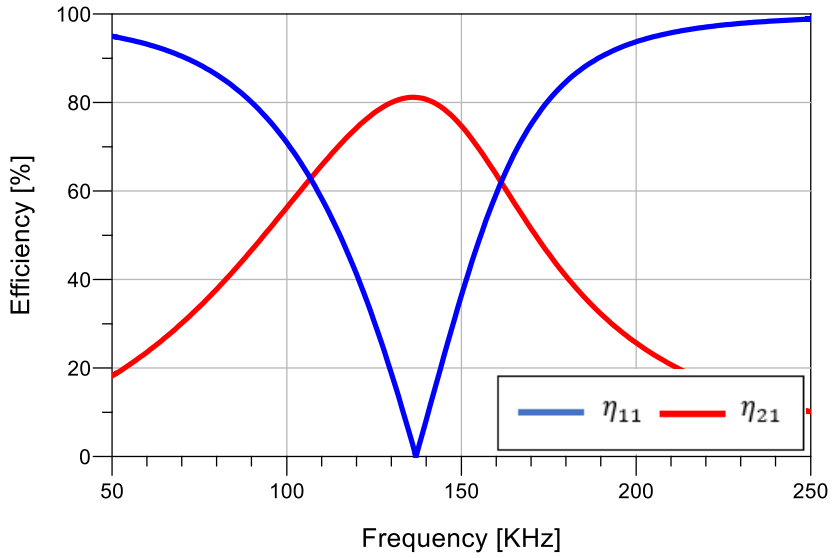

Figure 3.14: PP-Topology best performance plot for η_{11} and η_{21}

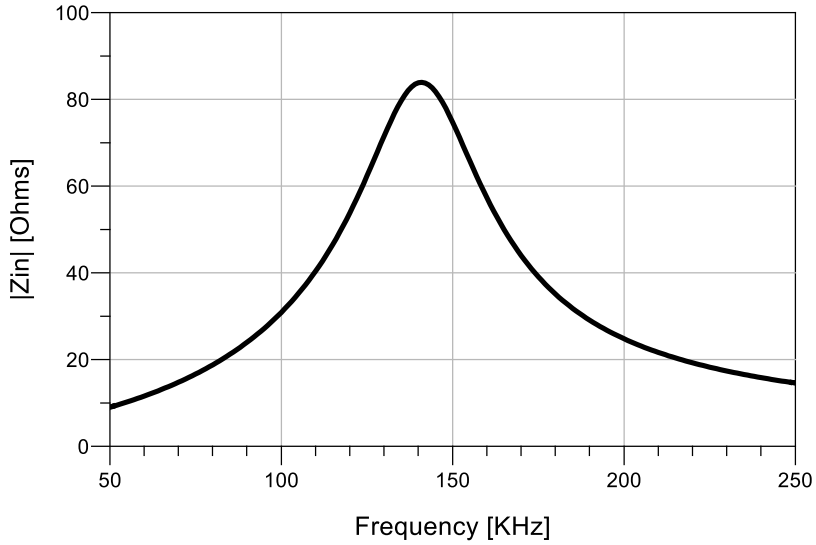

Figure 3.15: PP-Topology best input impedance plot for third run

Figure 3.16 summarizes the conclusions make up until this point. Once again, the optimal performance value was around $k = 0.4$ and is only because the distance margin reduces significantly with slight increases in η_{21}. The curve in Figure 3.16 is for PP-Topology very similar to Figure 3.4 for SS-Topology and behaves about the same, however it has slightly lower efficiency.

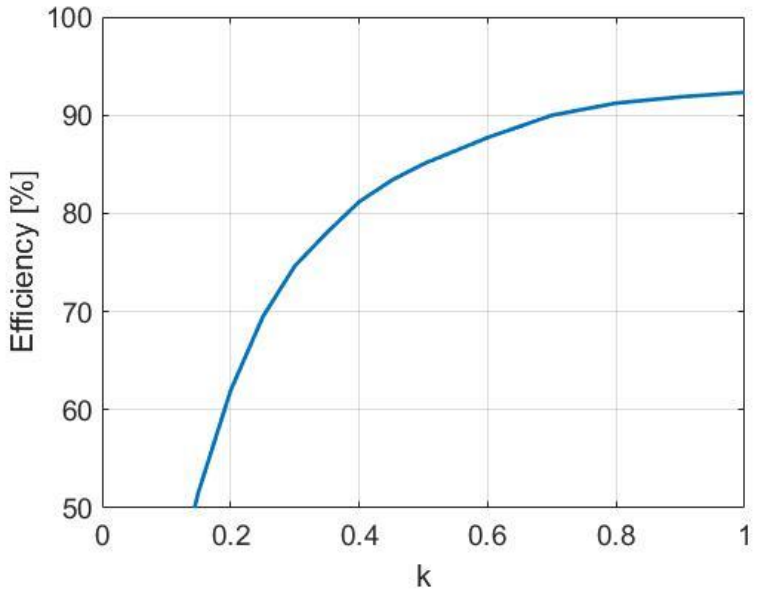

Figure 3.16: MATLAB plot of Table 3.4 of η_{21} verses k for PP-Topology

3.6 Analysis and Comparison of the Four Network Topology Models

Figure 3.17 and 3.18 summarizes all four topologies on a single plot for comparison of both k and L_m verses efficiency, respectively. Since $L_m = Lk$, Figure 3.18 simply rescales the x-axis in Figure 3.17. Appendix B shows the MATLAB code used to process the data from the previous four detailed studies on these four topologies.

As a comparison, the best performing topology that is the most stable and flexible that yields the highest power transfer efficiency is SS-Topology relative to the others. This is with both termination impedances the same and because of symmetry, $C_1 = C_2$ as shown in the simulations

which also agrees with equations (2.34) and (2.50). This is the model that will be used for measurements due to its flexibility and performance. The next best performing topology is PP-Topology, but unlike SS-topology, $C_1 \neq C_2$ for optimal performance according to simulation data and mathematical derivations.

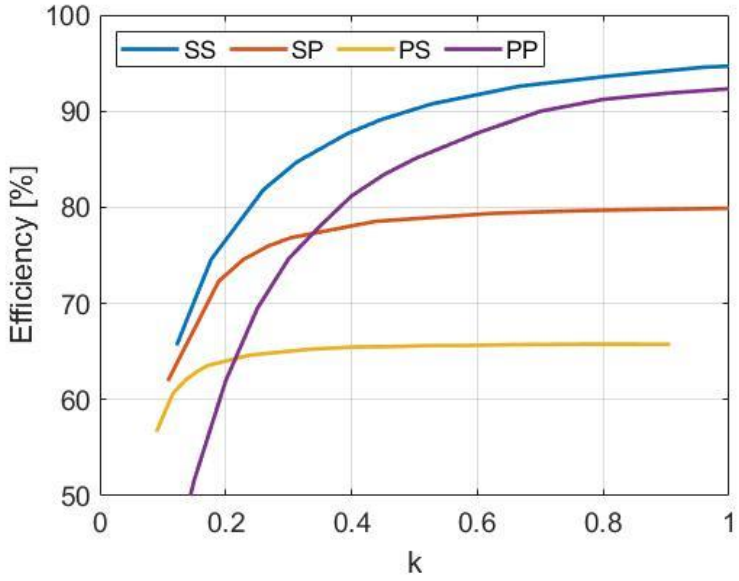

Figure 3.17: MATLAB plot of η_{21} verses k comparing all topologies

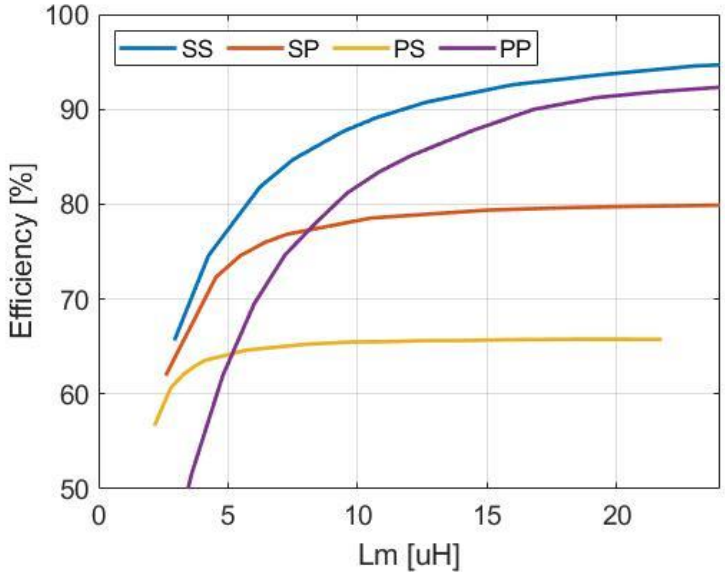

Figure 3.18: MATLAB plot of η_{21} verses L_m comparing all topologies

The input and load terminations must also change and be adjusted as k changes meaning it is not as stable relative to SS-Topology. SP and PS-Topologies are the least best performing in terms of efficiency but they do offer some design advantages. For an application that requires a high load termination impedance relative to the input termination, SP-Topology is the best choice. On the other hand, an application that requires the opposite, in that it requires a high input termination impedance and low load impedance, PS-Topology is the best performing. In both of these cases Z_{IN} changes and is the mirror image of the input termination impedance.

CHAPTER 4
Experimental Setup for SS-Topology and Measurements

4.1 Modified Simulation Setup and Component Values

Based on the simulations in previous sections, the topology that will be used and integrated into a prototype for experimentation and measurements is SS-Topology. Due to the limitations of certain laboratory equipment, the operating frequency will need to be increased to greater than $f_0 = 1\ MHz$. For measurements, the test specimen or Device Under Test (DUT) that will be used for this study is from Wurth Elektronik Part Number 760308101208A which has physical dimensions according to Figure 4.1 with some performance data taken from the data sheet in Figure 4.2. It is critical to point out that this geometry is an Archimedean spiral with an inner and outer diameter as it was described in Section 2.1.2, Figure 2.5. Therefore, the theoretical relationship between L_m and g as described by equations (2.28) and (2.30) will apply to this DUT.

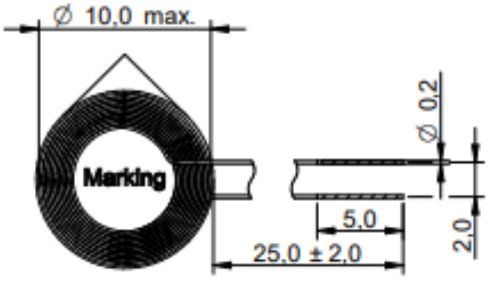

Figure 4.1: Inductor for measurement, Wurth Elektronik PN 760308101208A

Properties	Test conditions		Value	Unit	Tol.
Inductance	125 kHz/ 10 mA	L	18	µH	±10%
Q-Factor	125 kHz/ 10 mA	Q	18		typ.
Rated Current	ΔT = 40 K	I_R	0.7	A	max.
Saturation Current		I_{SAT}	2	A	typ.
DC Resistance	@ 20 °C	R_{DC}	550	mΩ	typ.
DC Resistance	@ 20 °C	R_{DC}	650	mΩ	max.
Self Resonant Frequency		f_{res}	24	MHz	

Figure 4.2: Important performance characteristics of the inductor Figure 4.1

Before measurements are actually taken, a re-simulation of SS-Topology will be performed at a higher operating frequency as mentioned previously. There are two reasons this was done. The first reason was so that measurements could be obtained with a capable VNA in order to measure S-parameters. Even though an oscilloscope could still be used at a lower frequency, the intention is to utilize the same test setup for higher frequency measurements in the future. The second reason this was done is so that a slightly higher Q-factor could be obtained and thus better efficiency. According to the performance data in Figure 4.2, the Q-factor for this DUT is not very great at $Q = 18$ measured at a test frequency of $f_{test} = 125\ kHz$. Increasing the frequency should yield a better result. Figure 4.3 shows the ADS circuit configuration and setup that sweeps from $0.5\ MHz \leq f_0 \leq 2\ MHz$. The system parameters are chosen with the experimental setup in mind and per the inductor values in Figure 4.2. For a frequency of $f_0 = 1\ MHz$ both compensation capacitances according to (4.1) would need to both be $C = C_1 = C_2 = 1.407\ nF$, which is not a common capacitance value.

$$C = \frac{1}{4\pi^2 f_0^2 L} \tag{4.1}$$

It also would not be worth the effort to try and parallel connect capacitors in order to obtain that simply because the tolerance of each component would not make the effort worth it. Therefore, for this upcoming experimental setup, a common capacitance value of $C = 1\ nF$ will be chosen which, according to equation (4.2) will give rise to a resonance frequency of $f_0 = 1.186\ MHz$.

$$f_0 = \frac{1}{2\pi\sqrt{LC}} \tag{4.2}$$

Once again, because component tolerance levels will interfere with this experimental setup it will be perfectly acceptable to set both compensation capacitances at $1\ nF$ for this reason. Before

taking measurements, we will run some ADS simulations in order to get an idea of the type of performance to expect using these system parameters.

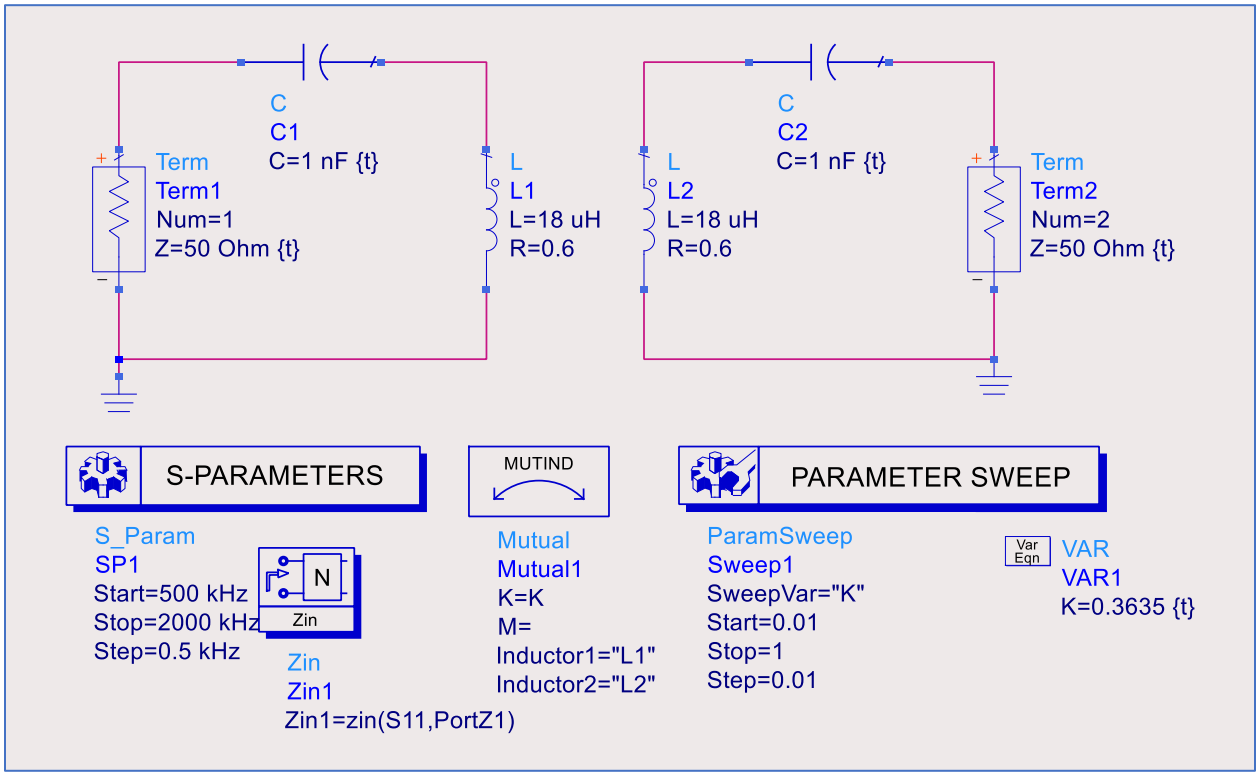

Figure 4.3: ADS circuit configuration and setup for SS-Topology rerun for $C = 1\ nF$

We would expect that the power transfer efficiency is going to increase given and increase in operating frequency which is positively correlated with Q-factor. This expectation is based on equation (4.3) indicating that the quality factor is proportional to frequency with all other parameters held fixed.

$$Q = \frac{2\pi f L}{R} \tag{4.3}$$

4.1.1 k-to-g: method for obtaining simulated g from after simulating k

The Vector Network Analyzer (VNA) that will be used is Keysight E5063A and is shown in Figure 4.4. It is good for a frequency range starting at 100 kHz until 4.5 GHz. This means that

it is more than capable to test the system setup over the required frequency range per the system configuration setup in Figure 4.3.

The VNA used for experimental measurements shown in Figure 4.4 and has 50 Ω ports. Because of these 50 Ω ports, the ADS circuit in Figure 4.3 also needed to be setup and made with 50 Ω terminations.

Figure 4.4: Keysight VNA E5063A used for experimental measurements

As they were preformed previously, the ADS simulations were run for both S_{11} and S_{21}. Following the same procedure that was done in Section 3.2 at this new higher resonance frequency, the simulation that gave rise to optimal results was found when $k = 0.3635$ and the S-parameter results are displayed in Figure 4.5. An additional 12 runs were made and tabulated in Table 3.5.

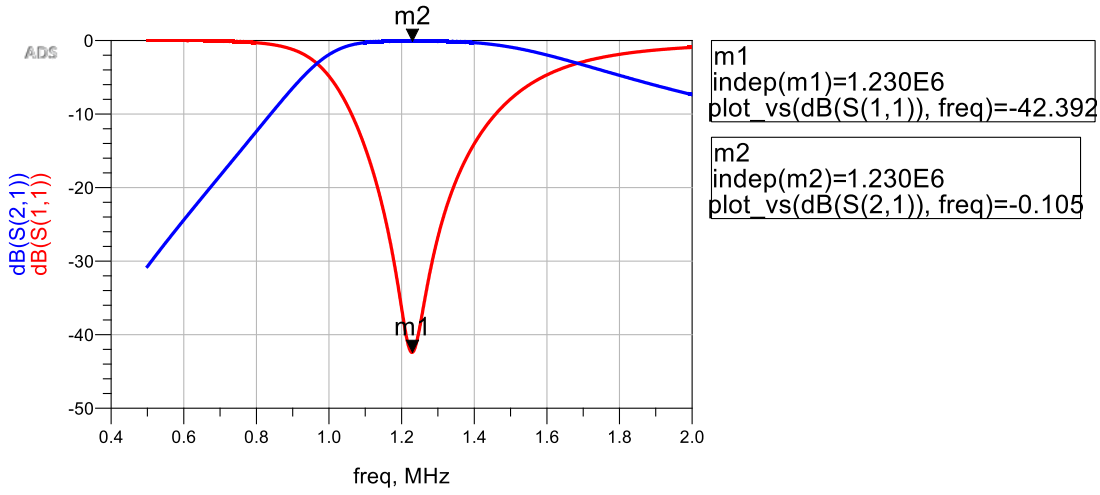

Figure 4.5: Simulated optimal performance result for $k = 0.3635$

The simulated values for k and L_m were fed back into the Neumann formula (2.30) and generated numerical values for g. Therefore, based on ADS simulations, when $k = 0.3635$ equation (2.30) predicts the optimal separation distance between L_1 and L_2 to be when $g = 1.59\ mm$. This reasoning is summarized in Figure 4.6 and it is a method to obtain a simulated value numerically for g from ADS simulated values of k with using well established theory. If the mathematical derivation for the Neumann formula was done correctly for Archimedean spiral, this approach should be a valid method. Confirmation of this claim would be when the reverse method is applied with measured values for g giving rise to measured values for k using once again the same Neumann formula. The two results should agree.

Table 4.1: Simulated ADS Data for SS-Topology @ $f_0 = 1.230\ MHz$

k	L_m [µH]	g [mm]	S_{11} [dB]	S_{21} [dB]
0.4395	7.911	0.960	-14.75	-0.236
0.3880	6.984	1.370	-24.67	-0.113
0.3635	6.543	1.590	-42.39	-0.105
0.3500	6.300	1.720	-26.88	-0.118
0.3300	5.940	1.930	-19.67	-0.163
0.3080	5.544	2.170	-15.32	-0.255
0.2945	5.301	2.330	-13.38	-0.337
0.2750	4.950	2.580	-11.171	-0.489
0.2590	4.662	2.810	-9.587	-0.662
0.2556	4.601	2.850	-9.252	-0.710
0.2485	4.473	2.960	-8.674	-0.800
0.2335	4.203	3.200	-7.541	-1.023

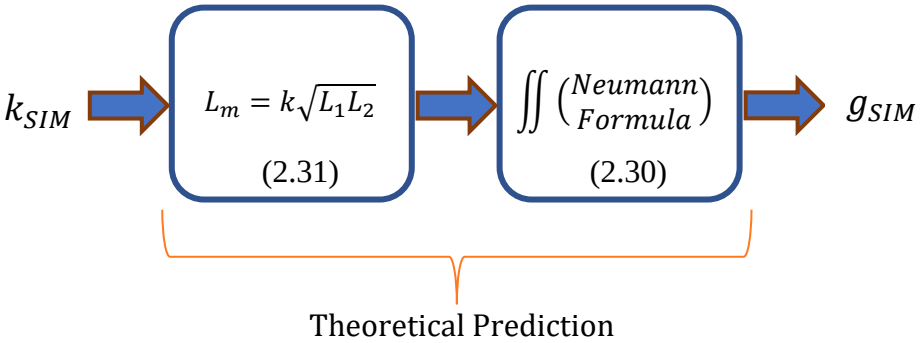

Figure 4.6: Method/model for obtaining simulated g from simulating k (k-to-g)

4.2 Test Specimens and Initial Measurements

The experimental setup needs to be designed in such a way so that distance measurements between L_1 and L_2 can be repeatable. In order for S-parameter measurements to be possible, both inductors must connect to and be terminated with an SMA 50Ω connector. As discussed previously, both inductors must have a 1 nF capacitor in series with it. The test specimens designed are shown in Figure 4.7 using FR4 1.6 PCB that measures (L x W) = (32 x 20) mm. As shown, there are soldering pads on the end for both inductors.

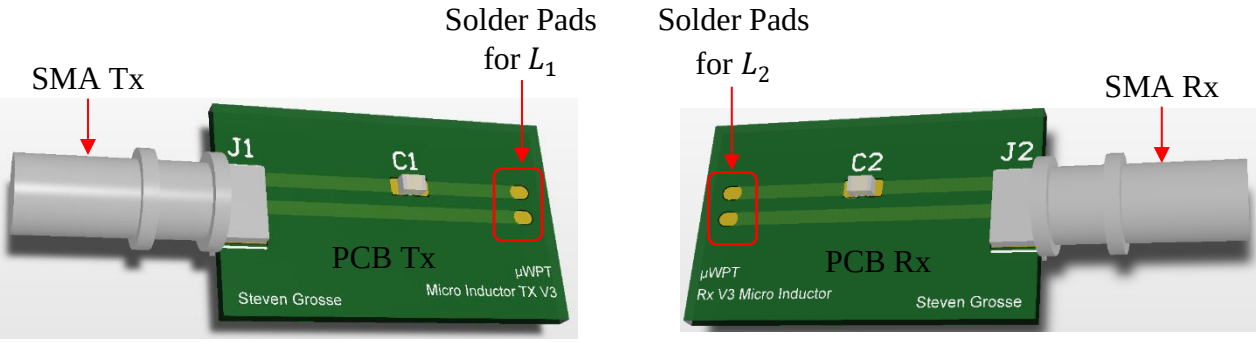

Figure 4.7: CAD model showing for PCB test specimens for experimental setup

L_1 and L_2 must also be axially aligned similar to how they would be fixtured in a typical connector application. In addition, one inductor must be statically fixtured while the other is free to move back and forth in 1-demension while g is measured. The proposed setup is shown in Figure 4.8 allows us to do just that using a pair of digital calipers. In this setup both PCB Tx and Rx are epoxied onto one flange of the calipers. PCB Tx is held fixed while PCB Rx is allowed to move back and forth while the separation distance can be adjusted and measured just as required. What is convenient about this setup is once the two PCBs are positioned and mounted independently, both L_1 and L_2 can be brought right up to each other as shown in the figure to the point that they

are physically touching each other. This is when the digital calipers are set to zero reference. Whenever PCB Rx is moved back slightly, that distance is accurately measured. See Figure 4.9.

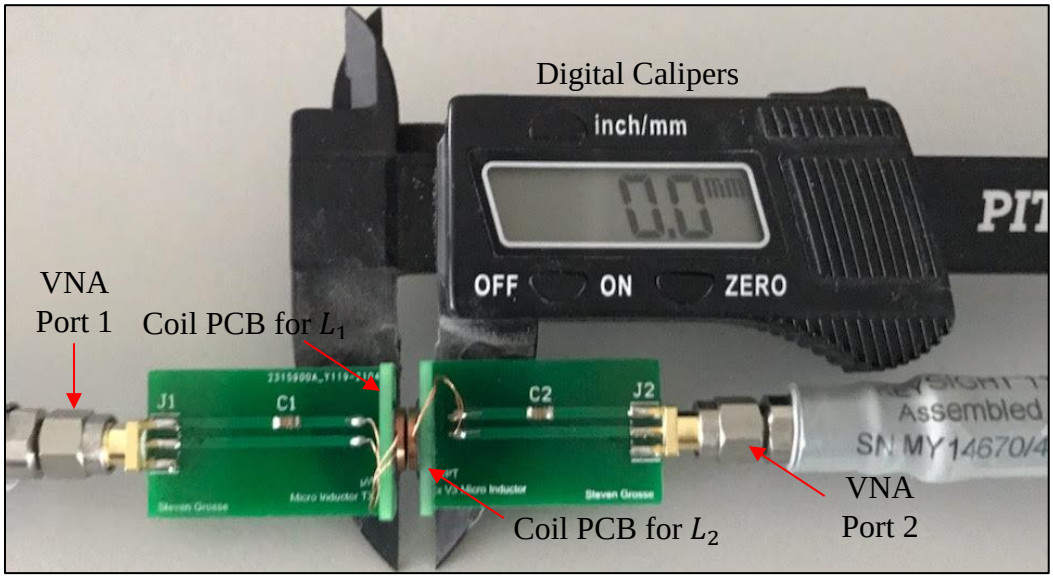

Figure 4.8: Experimental setup using digital calipers at $g = 0.0$ mm

One more important detail worth mentioning are the Coil PCBs. There is one for each L_1 and L_2 which are both mounted perpendicular onto their respective PCB. They are what allows both inductors to be axially aligned and face each other.

Figure 4.9: Experimental setup setting separation distance at $g = 5.0$ mm

Figure 4.10 shows the experimental setup connected to the VNA. In this setup, the separation distance is $g = 1.6$ mm which is what was predicted in ADS simulations to be the optimal value.

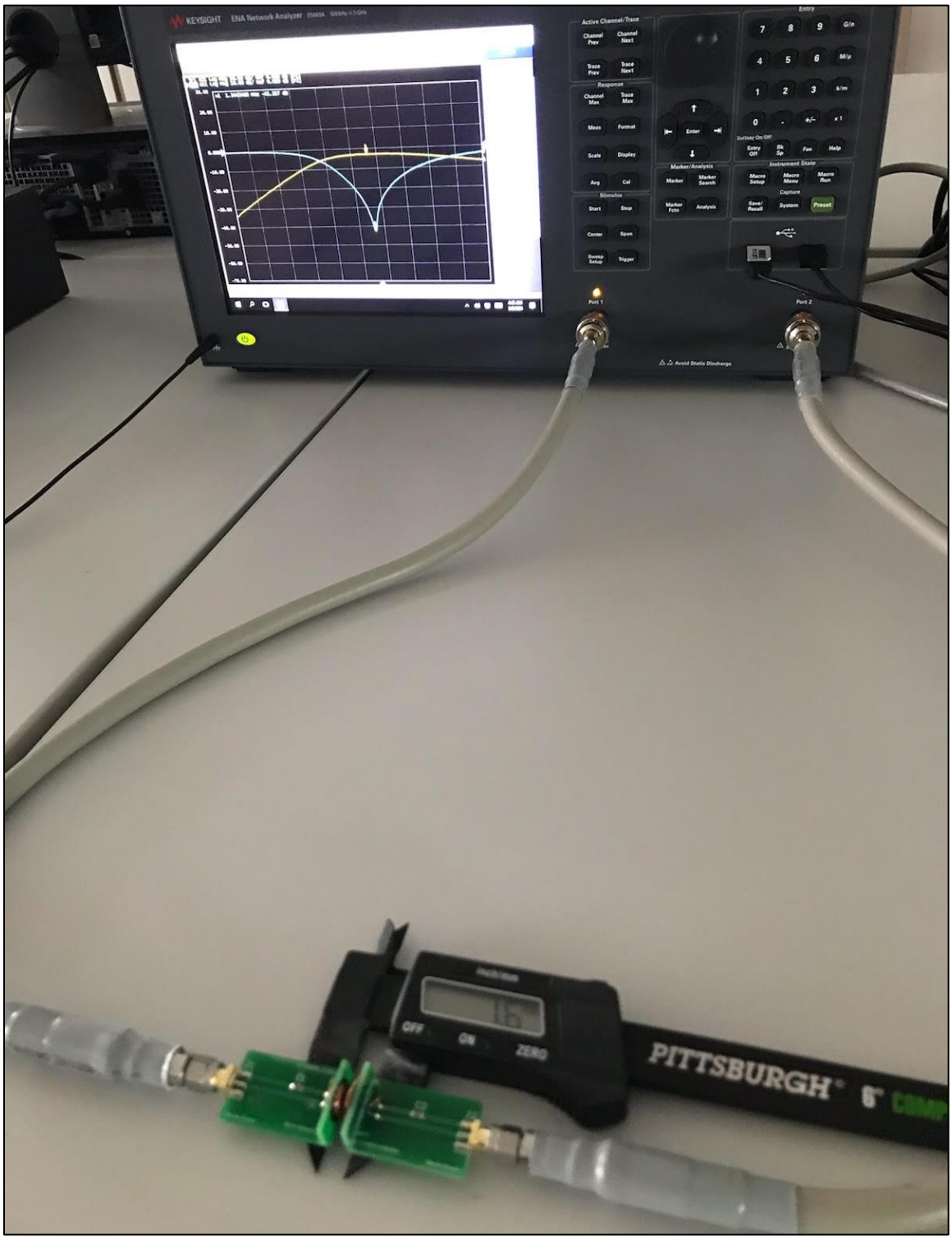

Figure 4.10: Experimental setup connected to the VNA at $g = 1.6$ mm

A screenshot of Figure 4.10 was taken during this measurement and is displayed in Figure 4.11. Notice the striking similarity to ADS simulations in Figure 4.5 for $k = 0.3635$, which was predicted to be the optimal performance value for this setup. Table 4.1 and the k-to-g model in Figure 4.6 predict that $g = 1.59\ mm$. Measurements show $g = 1.6\ mm$ at the same S-parameter values. The VNA trace data was taken for this measurement which produced 204 data points from $0.5\ MHz \leq f_0 \leq 2\ MHz$ – the same scale used in all ADS simulations and subsequent measurements. The trace data for the simulation taken in Figure 4.5 was also recorded – which produced 3000 data points – and both sets of data were imported into MATLAB and plotted on the same axis for comparison. This comparison is show in Figures 4.12 and 4.13 for S_{11} and S_{21}, respectively. The MATLAB code written to process this data is given in Appendix B.4.

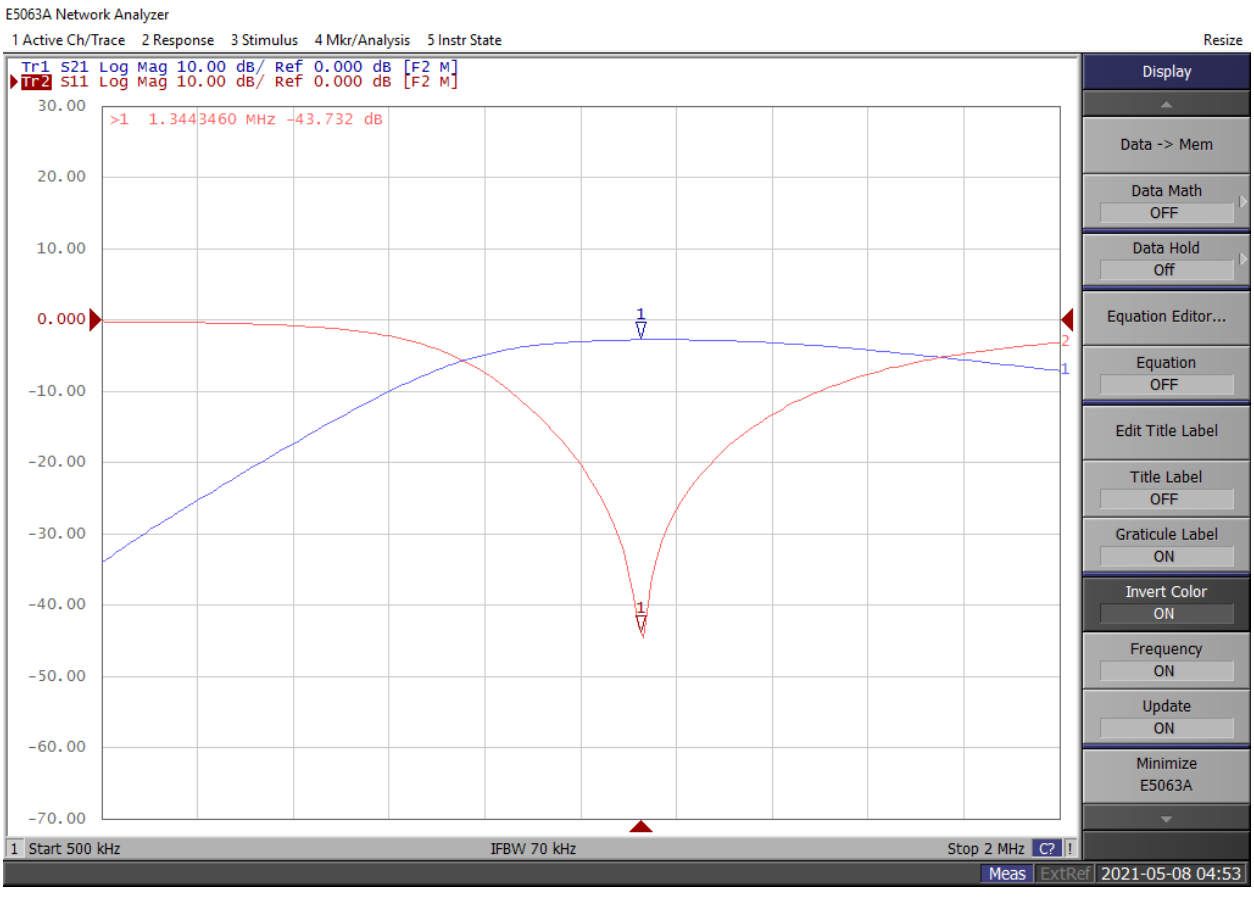

Figure 4.11 Screenshot of VNA for separation distance set at $g = 1.6$ mm

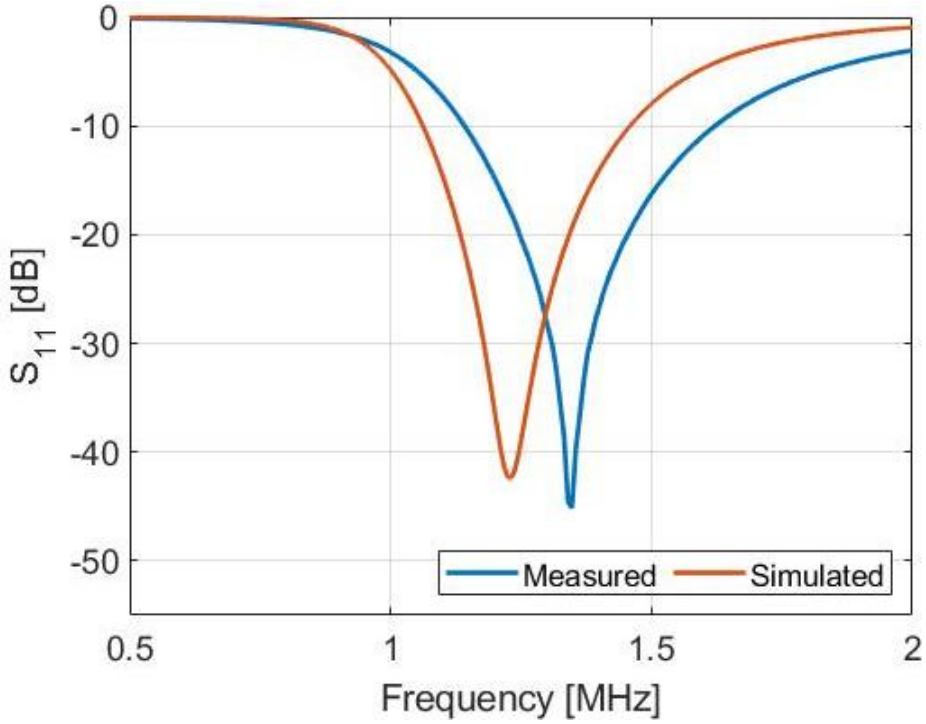

Figure 4.12: Comparison between measured and simulated data for S_{11} at $g = 1.6$ mm

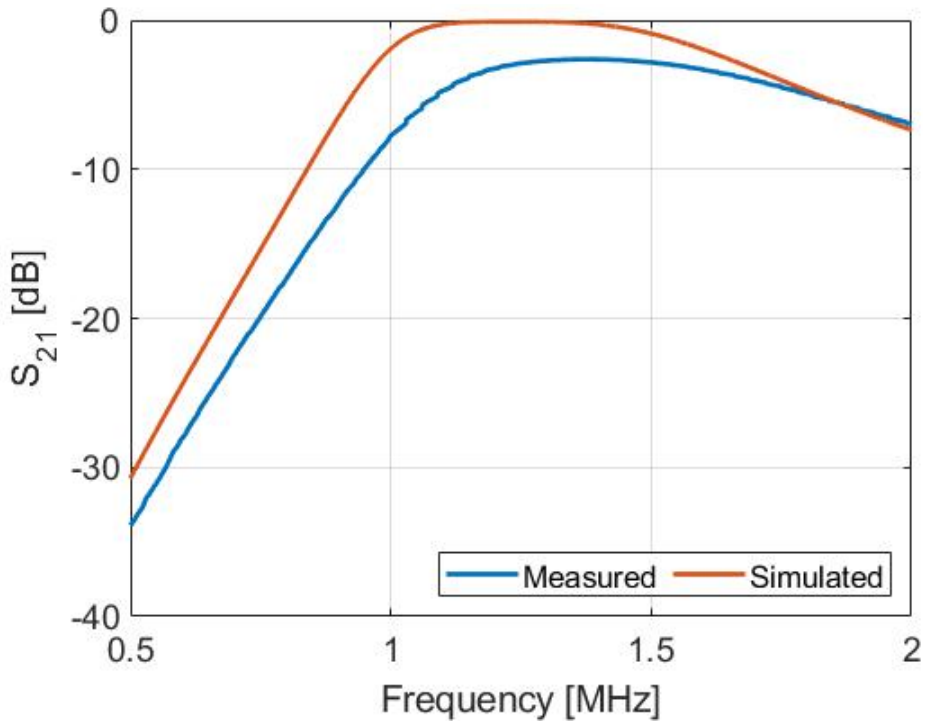

Figure 4.13: Comparison between measured and simulated data for S_{21} at $g = 1.6$ mm

4.2.1 ADS simulation and VNA measurement comparison

From analyzing both Figures 4.12 and 4.13, there exists a noticeable discrepancy between ADS simulations and VNA measurements. The shape and profile between the two are the same, but there is a shift in resonance frequency between the two. Theoretical calculations per equation (4.2) predict $f_0 = 1.186\,MHz$, however ADS simulations showed this condition occurs at $f_0 = 1.230\,MHz$ and VNA measurements show it to be at $f_0 = 1.344\,MHz$. While these values are not very far off from each other, and explanation is still forthcoming. A plausible explanation for the discrepancy between simulation and measurements are with component tolerances. The simulations were performed with all component values set at the nominal values. That is, $C_1 = C_2 = 1\,nF$, $L_1 = L_2 = 18\,\mu H$, and $Term1 = Term2 = 50\,\Omega$ exactly. But this is not the case in the real world where the actual values that these components take on drift within their allowed manufactured tolerance range of 5%.

Table 4.2 shows the minimum and maximum extremes these components can drift. The question then becomes can these values shift the resonance frequency range and create a possible condition that would allow simulations to better match measurements, and if so, what values must the components take on? ADS can answer both of these questions with the tuning function. With the target frequency set to $f_0 = 1.344\,MHz$, the component values are each tuned allowed 5% tolerance range.

Table 4.2: Table of values for measurement components within 5% tolerance

Value	C_1 [nF]	C_2 [nF]	L_1 [µH]	L_2 [µH]	Term1 [Ω]	Term2 [Ω]
Minimum	0.95	0.95	17.1	17.1	47.5	47.5
Nominal	1.0	1.0	18.0	18.0	50.0	50.0
Maximum	1.05	1.05	18.9	18.9	52.5	52.5
Tuned	0.96	0.91	16.0	17.1	45.0	53.4

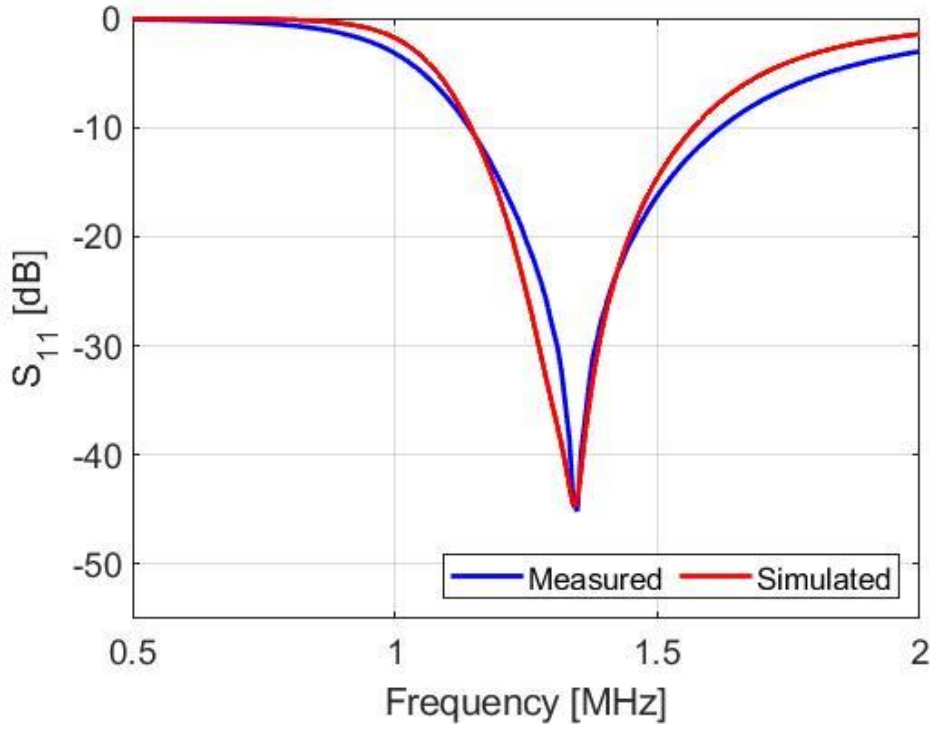

Figure 4.14: Comparison of measured and tuned simulated data for S_{11} at $g = 1.6$ mm

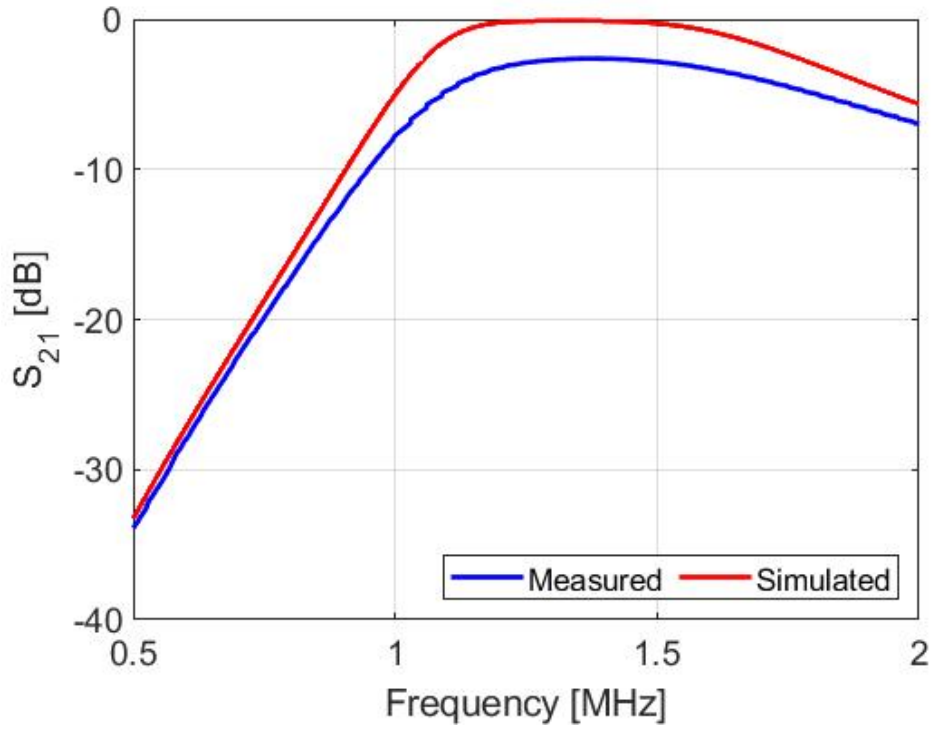

Figure 4.15: Comparison of measured and tuned simulated data for S_{21} at $g = 1.6$ mm

When the tuned values in Table 4.2 are used in the ADS circuit configuration in Figure 4.3 and the simulation rerun, and then subsequently compared with measurements again, the comparison plots change as shown in Figures 4.14 and 4.15, the resonance frequency between simulation and measurements are aligned. It was observed during the experimental runs that careful adjustments must be made while setting up the VNA cables and connecting them to the SMA connectors on the test specimen PCBs. Not torqueing them enough would result in a poor measurement, and over torqueing them weakens the SMA connection. Four additional measurement and simulation data sets were taken for $g = 1.2$ mm, $g = 1.4$ mm, $g = 2.1$ mm, and $g = 3.5$ mm in Figure 4.16.

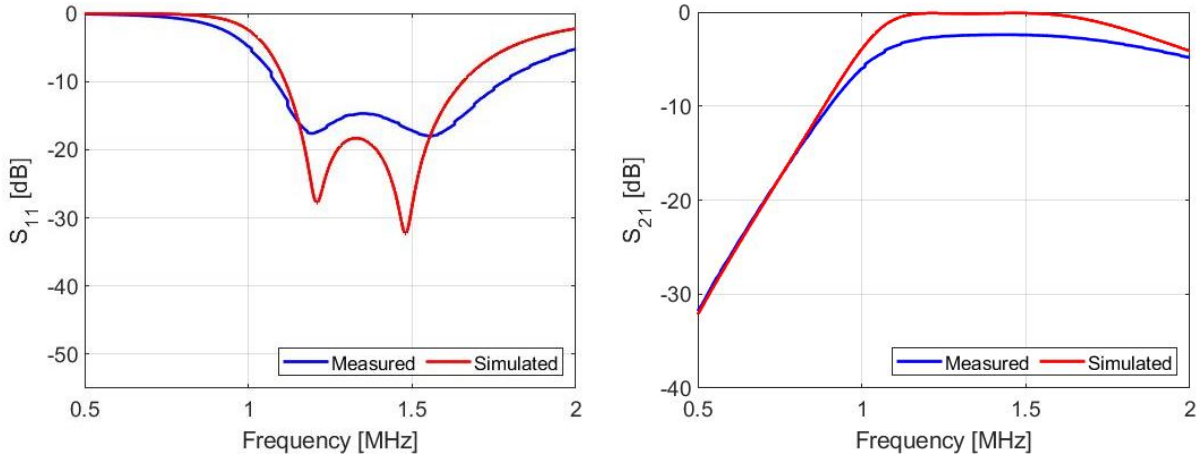

(a)

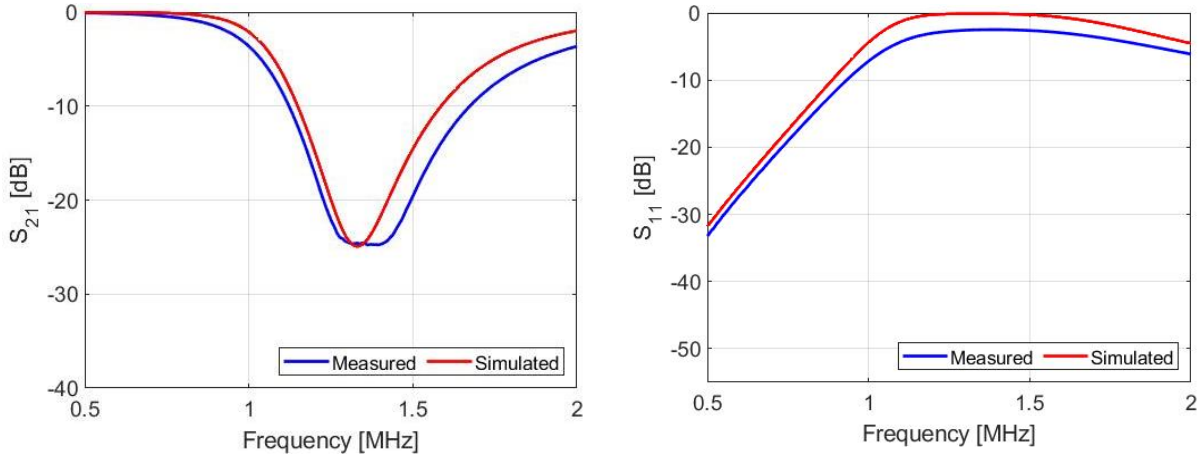

(b)

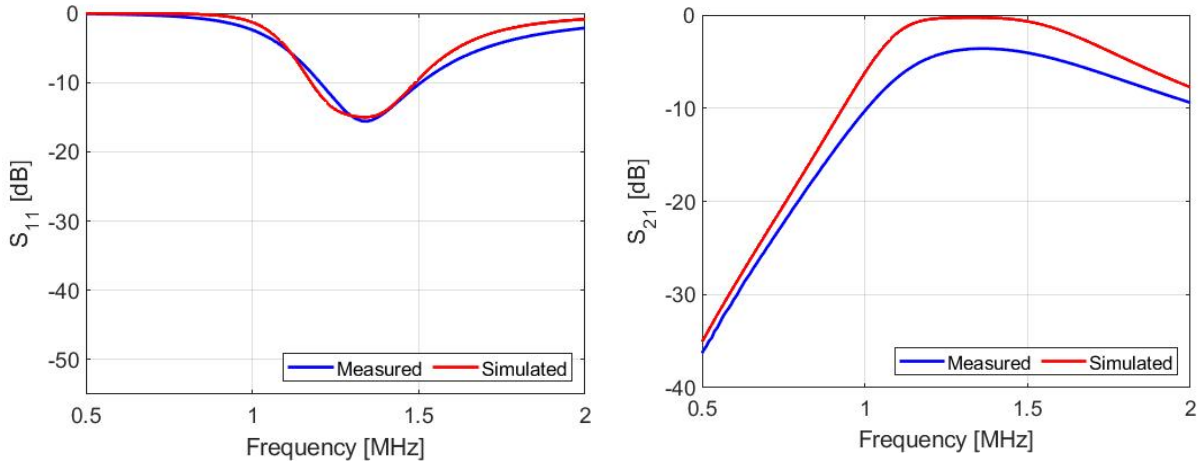

(c)

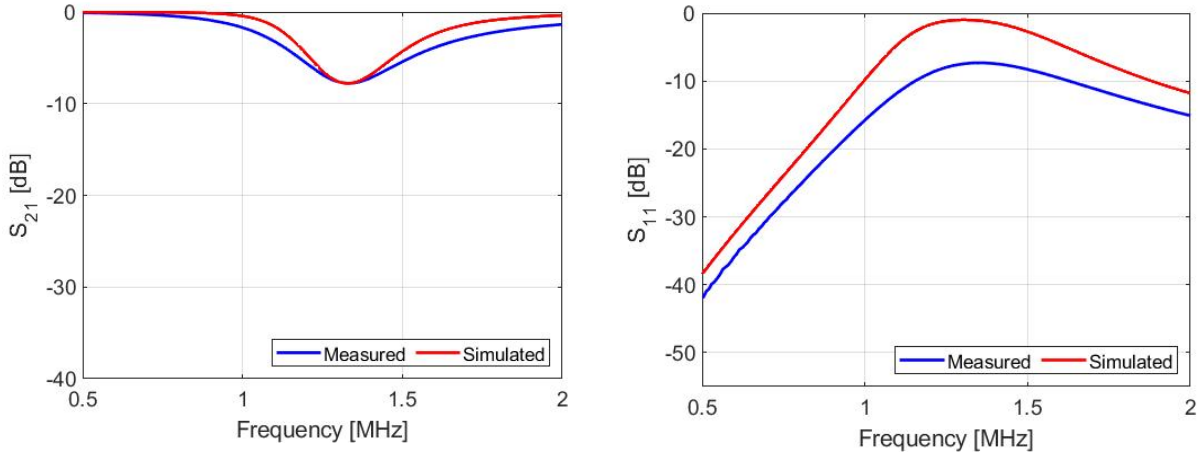

(d)

Figure 4.16: Simulation/measurement comparisons at $g = 1.2$ mm (a), $g = 1.4$ mm (b), $g = 2.1$ mm (c), and $g = 3.5$ mm (d)

4.2.2 g-to-k: method for obtaining measured k from after measuring g

Measurements continued even beyond what was obtained in Figure 4.16 (a)-(d) and a total of 12 data points were taken and recorded very similar to the way they were done for ADS simulations. This measured data is tabulated in Table 4.3. The reverse method was used for measurements in that separation distance measurements were taken first, S-parameter data recorded, and then those separation distance measurement values were run through the Neumann

formula to obtain measured values for k. This is the reverse method that was done for simulations as summarized in the model in Figure 4.17. This reverse method is summarized in Figure 4.6. As mentioned already, 12 different separation distances were measured that ranged from $1.2\ mm \leq g \leq 3.5\ mm$ followed by S-parameter measurements at each point. It was stated in Section 4.1.1 that if the mathematical derivation for the Neumann formula – obtained in equation (2.30) – was done correctly for the Archimedean spiral geometry, this approach should be a valid method and that confirmation of this claim would be in the agreement between both the forward (k-to-g) and reverse (g-to-k) methods. That comparison was obtained in Figures 4.18 and 4.19 by taking the data in both Tables 4.1 and 4.3 and plotting it using MATLAB for g vs k.

Table 4.3: Measured VNA Data for SS-Topology @ $f_0 = 1.344\ MHz$

k	L_m [μH]	g [mm]	S_{11} [dB]	S_{21} [dB]
0.4084	7.352	1.2	-14.72	-2.434
0.3846	6.924	1.4	-24.62	-2.521
0.3626	6.528	1.6	-43.73	-2.633
0.3522	6.341	1.7	-26.89	-2.789
0.3326	5.987	1.9	-19.63	-3.056
0.3143	5.658	2.1	-15.72	-3.600
0.2972	5.351	2.3	-13.39	-3.828
0.2813	5.065	2.5	-11.16	-4.450
0.2666	4.799	2.7	-10.07	-4.910
0.2527	4.549	2.9	-9.200	-5.540
0.2397	4.316	3.1	-8.650	-6.000
0.2161	3.891	3.5	-7.510	-7.230

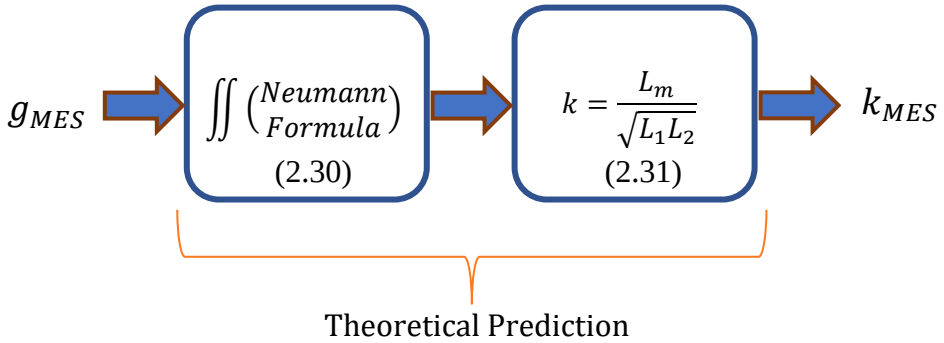

Figure 4.17: Method/model for obtaining measured k from measuring g (g-to-k)

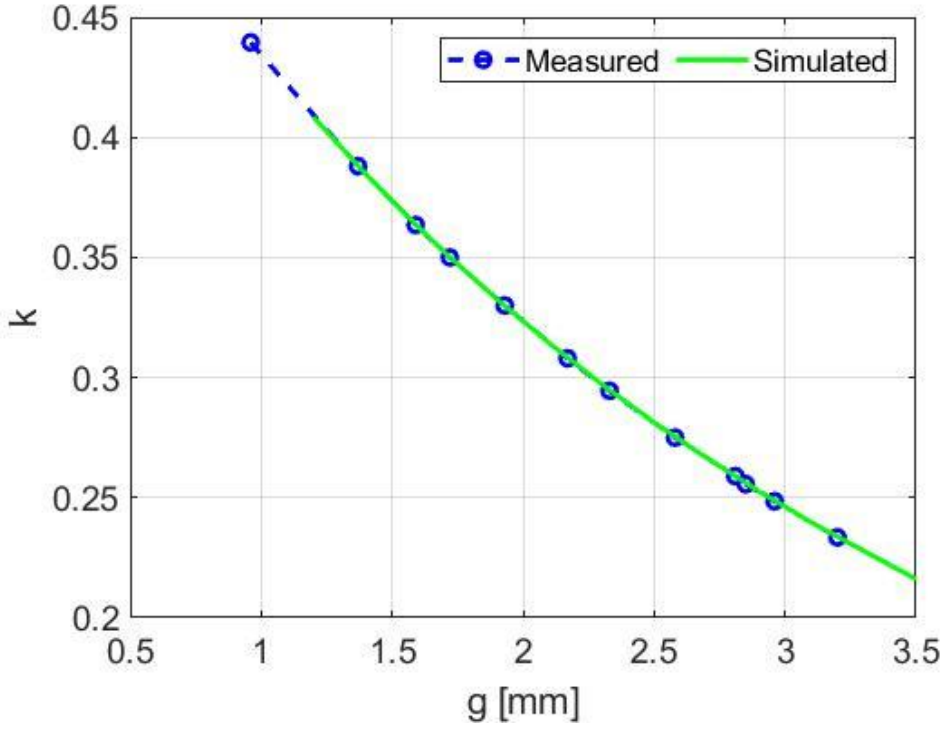

Figure 4.18: Comparison between measured and simulated g vs k

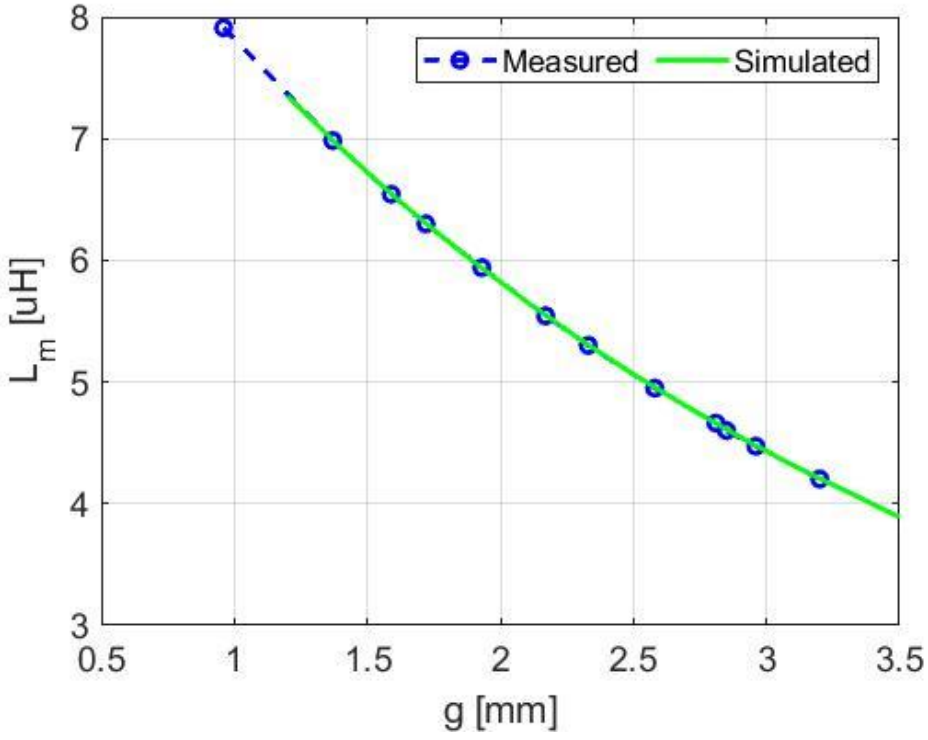

Figure 4.19: Comparison between measured and simulated g vs L_m

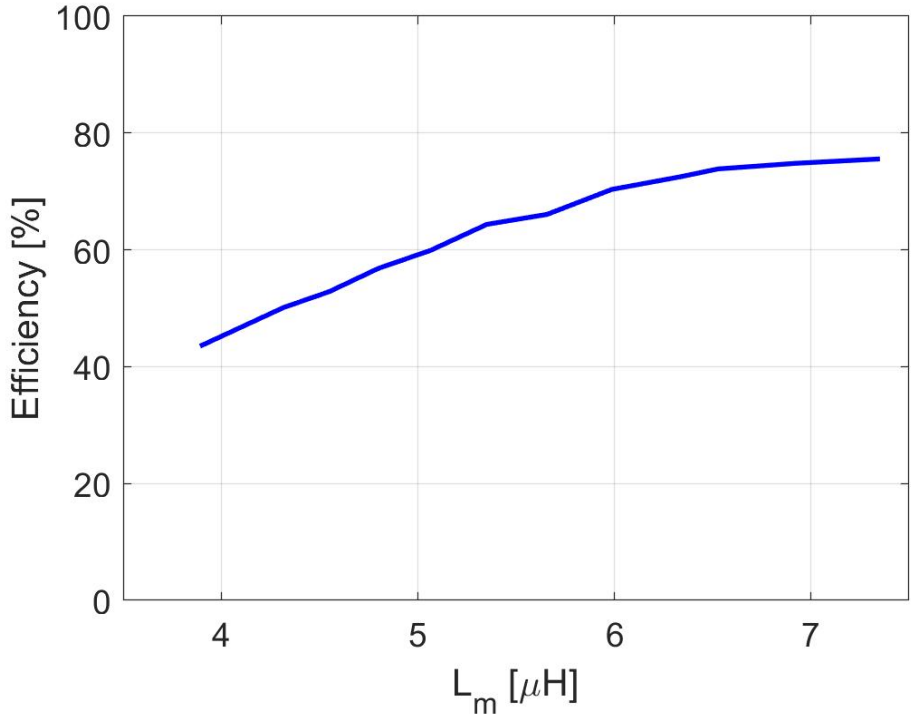

Figure 4.20: Relationship between measured L_m vs power transfer efficiency

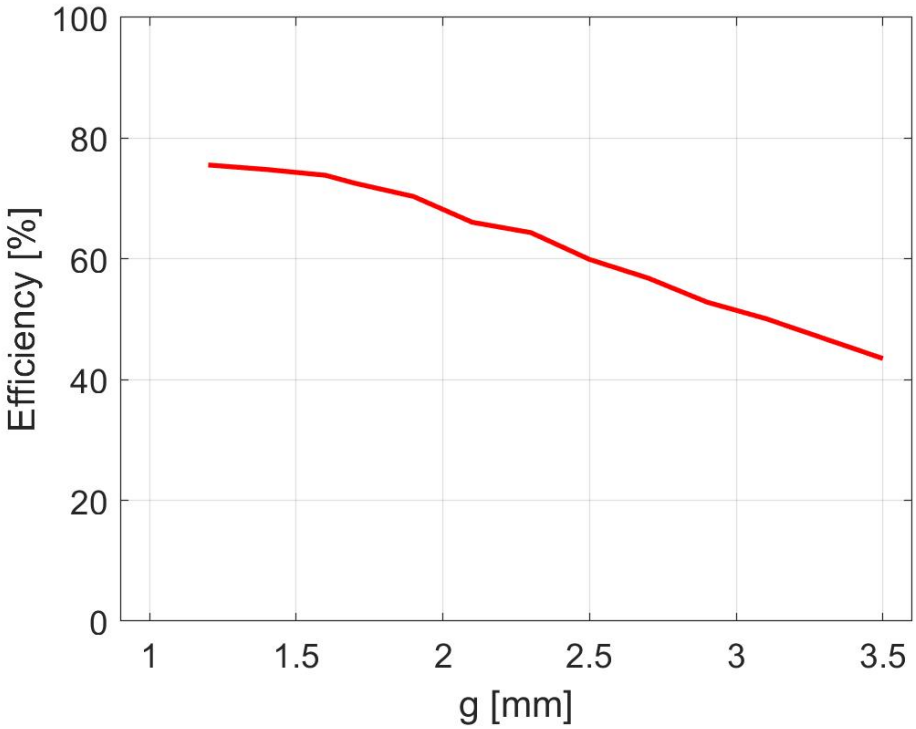

Figure 4.21: Relationship between measured g vs power transfer efficiency

Figure 4.20 plots the measured data in Table 4.3 of L_m and power transfer efficiency calculated by equation (3.2) and Figure 4.21 plots power transfer efficiency with respect to g. This is arguably the most useful plot because it reveals the distance margin as it relates to efficiency. It is important to keep in mind that this performance would change if a different topology was used or a different inductor geometry. This is practical information that can be used in the construction of an actual prototype that tests the concept of μWPT as it would apply to connectors. Integrating these concepts into an actual prototype and testing it over this distance margin would be proof-of-concept and validation that WPT systems can applied to connectors. However, it is important to note in order to completely correlate the results from this chapter to the theoretical calculations that were performed in Chapter 2, impedance re-normalization would still need to be accomplished.

CHAPTER 5
Non-Metallic Connectors for µWPT Applications

Chapter 4 provided both simulation and measurement validation for the concept of µWPT that were tied together with the theoretical derivations from Chapter 2 regarding the purpose for compensation capacitance. This chapter seeks to demonstrate the concept of µWPT even further by integrating those concepts into an actual Non-Metallic Connector (NMC) prototype and testing it. By doing so, and by showing an example of how µWPT can work with a prototype NMC, this would further the validation and claims made in section 1.2.1 about the benefits the NMC can bring to the connector industry by the problems that it can solve for it.

5.1 The NMC Power Connector

5.1.1 The Prototype Model

Figure 5.1 shows the NMC prototype housings. They were modeled and designed with Creo and 3D printed with high-resolution plastic resin. This prototype is based off the high-level illustration in Figure 1.10 for an inductively coupled NMC. For this prototype, the NMC Receptacle will embed the DC-to-AC inverter and the NMC Plug will embed the AC-to-DC rectifier according to the model illustrated in Figure 1.11. All components are enclosed behind plastic giving rise to a hermetically sealed assembly to ensure no water or moisture gets in.

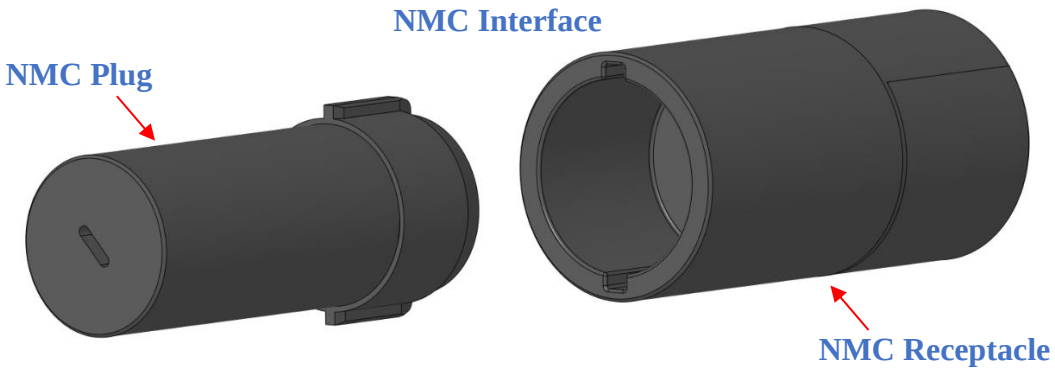

Figure 5.1: NMC prototype model for µWPT demonstration

Figure 5.2 shows a side view of the modeled NMC prototype unmated (top diagram) along with a longitudinal cross-sectional area (bottom diagram) that shows where the components will be placed. By looking at the housings themselves, the only thing that can be seen is the plastic housings. Everything else is inside. The point behind the NMC power connector operation is to have DC power coming in from the Receptacle end, and DC power coming out at the Plug end; the same function as standard connectors, but there are major differences in between that make that all happen. The inverters and rectifiers do the power conversion in between which sends it through NMC contactless interface and thus all the benefits of a contactless interface are achieved.

Notice that mechanical latches that are responsible for holding both connector halves together in standard connectors have been eliminated in the NMC design and replaced by magnets.

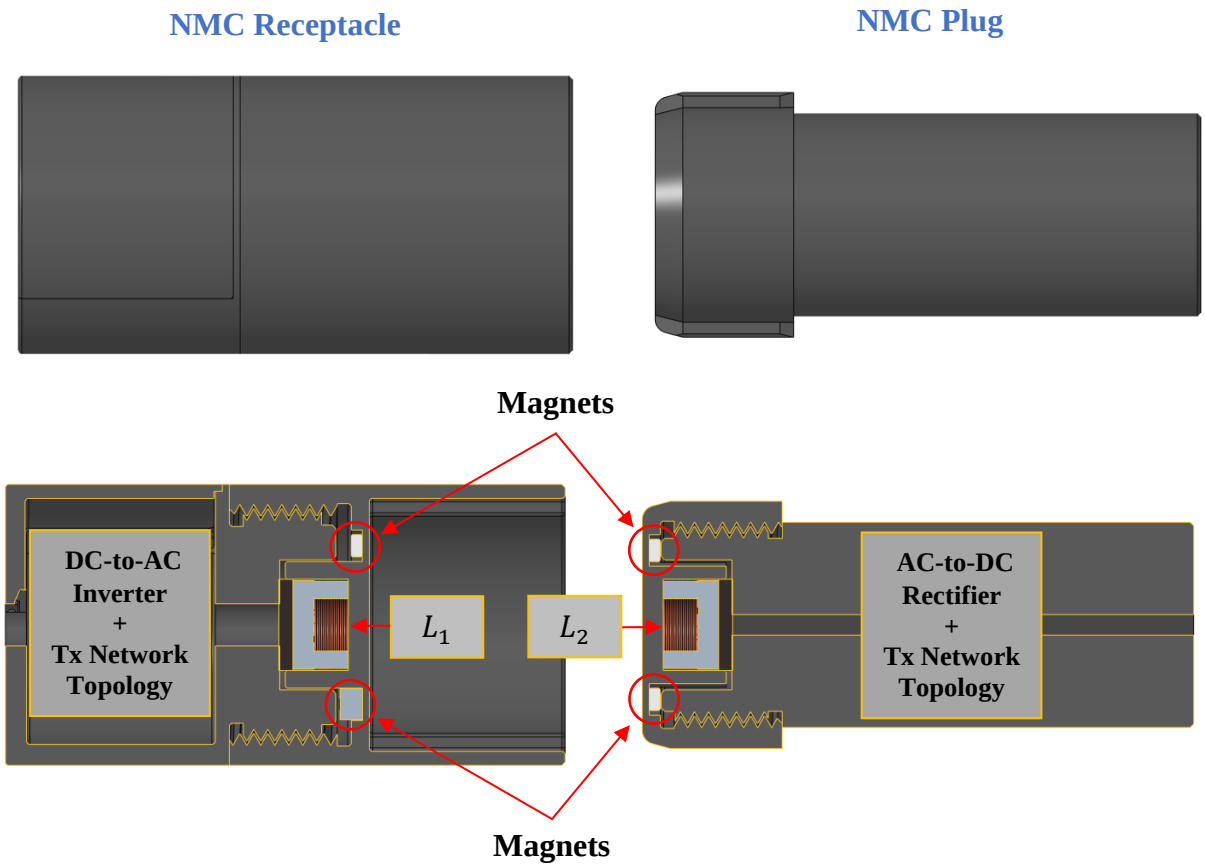

Figure 5.2: Unmated NMC prototype sideview and longitudinal cross-sectional area

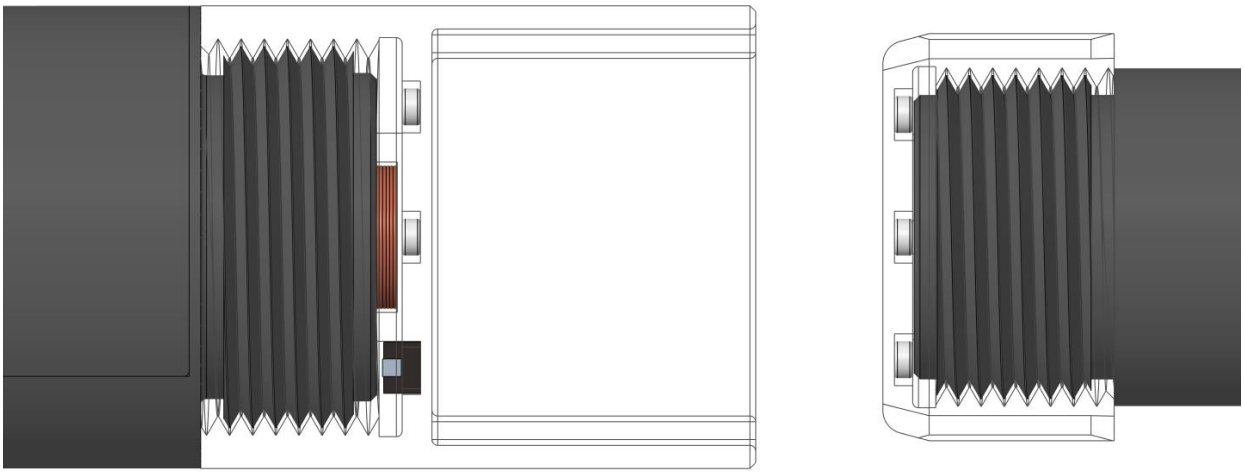

(a)

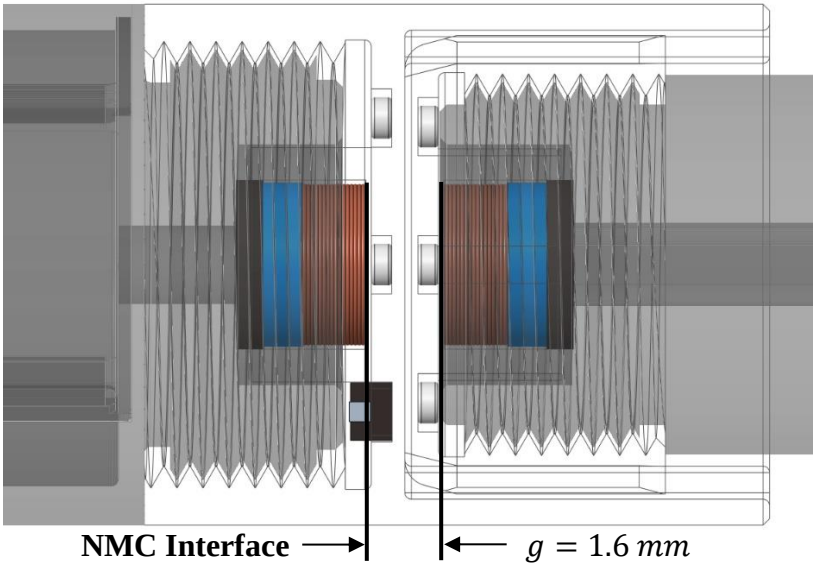

(b)

Figure 5.3: Transparent NMC model showing (a) unmated condition and (b) mated condition

To help better illustrate the NMC model, Figure 5.3 shows a transparent version of it with both halves mated and unmated. Notice that in the mated condition, the model has been designed with the optimal separation distance of $g = 1.6\ mm$ between the plug and receptacle. Recall from Chapter 4 that this is the separation distance experimentally found to be the optimal distance for power transfer efficiency. Therefore, we can expect a power transfer efficiency to be around 75%.

5.1.2 The Prototype Experimental Signal Test

Before the DC-to-AC (inverter) and AC-to-DC (rectifier) circuits are constructed, the test specimen from the previous chapter will be tested in a different way. It will be tested by sending a signal generator and oscilloscope which will generate and measure a sinusoidal signal set at the same resonance frequency of $f_0 = 1.344\ MHz$ found to give rise to the best performance. The signal generator used for this experiment is Siglent model number SDG1026 which will connect to SMA Tx as the input signal and set to the desired configuration. To measure both input and output signals that result, an oscilloscope will be used which in this case is a 2-channel Hanteck model number DSO5202BM. Both signal generator and oscilloscope are down in Figure 5.4. Channel 1 will be connected to SMA Tx to measure the input signal and Channel 2 will be connected to SMA Rx to measure the output signal. The separation distance between L_1 and L_2 will once again be set at $g = 1.6\ mm$. This experimental setup is shown in Figure 5.5.

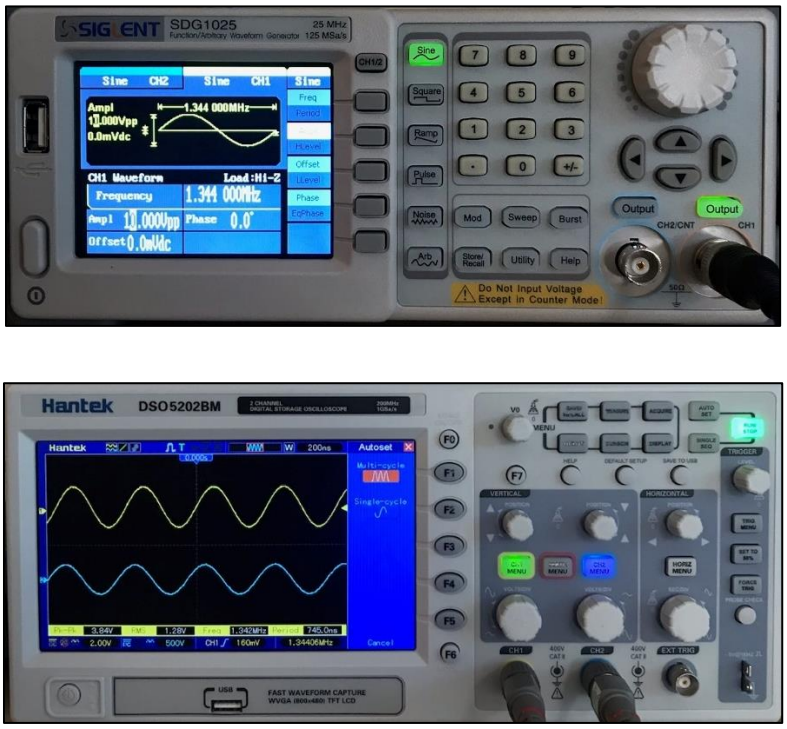

Figure 5.4: Siglent signal generator and Hanteck oscilloscope used in the experiment

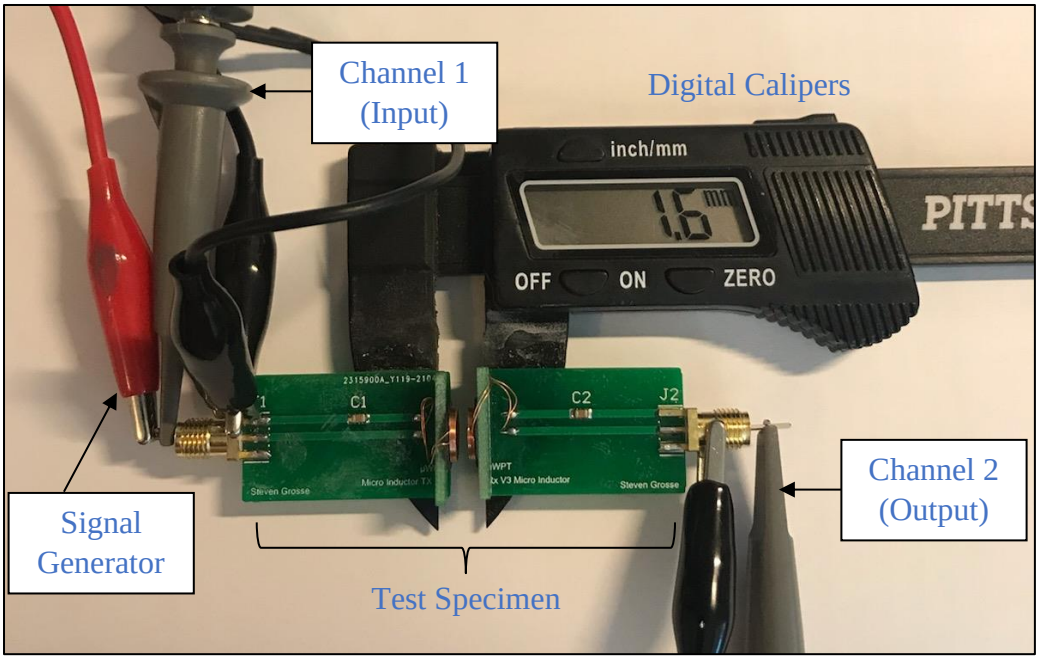

Figure 5.5: Experimental signal test setup with SS-Topology DUT

Note that the experimental setup in Figure 5.5 will test the integrity of the signals generated, passed through the DUT and received on the other end. It essentially is the SS-Topology that was tested in Chapter 4 that will be connected between both inverter and rectifier circuits when integrated into the final prototype. Notice also how both SMA connectors on the Test Specimen are probed. For both SMA Tx and SMA Rx, a small pin was inserted on both ends in order for the signal generator and oscilloscope to be able to make electrical connection to the signal on both ends. The alligator clips for the GND connection on both ends easily connected to both GND SMA for a good connection.

The purpose for this experiment therefore is to simply test the topology in this way separately before using it for the final prototype. The resulting waveforms measured by the oscilloscope are displayed in Figure 5.6. Notice that the oscilloscope is reading the same 1.344 MHz that is generated by the signal generator. Notice also that the Input signal measured on Channel 1 is slightly larger and amplitude relative to Channel 2 just as we would expect.

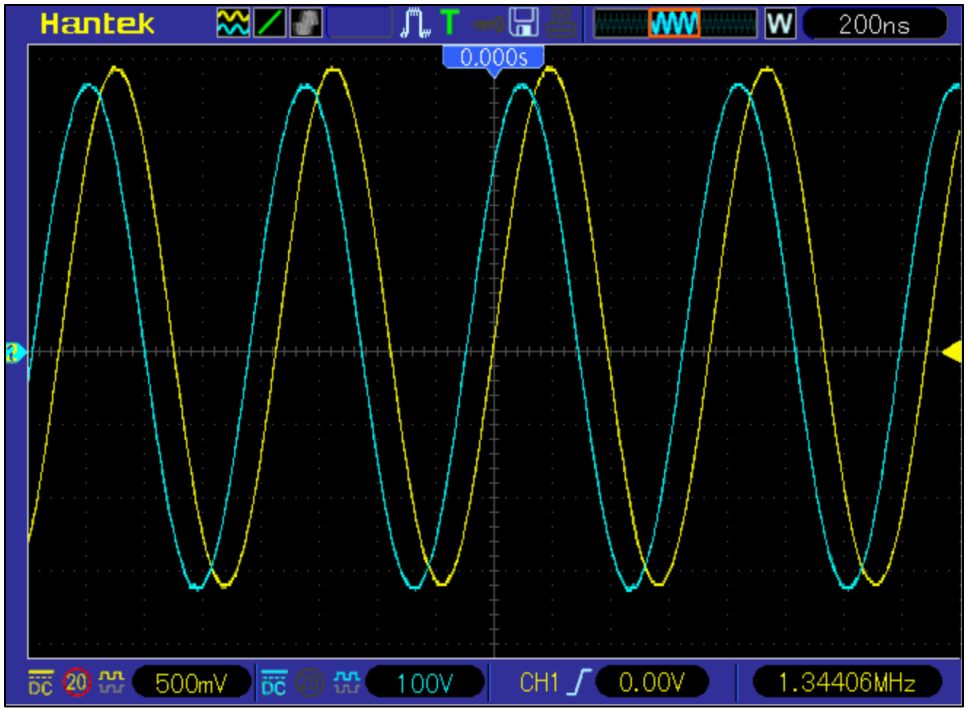

Figure 5.6: Screenshot of measured waveforms from the experimental signal test

5.1.3 The Prototype Inverter and Rectifier Circuitry

The purpose for the NMC power connector prototype is to demonstrate how DC power can be at the input and also arrive at the output, but the plug/receptacle interface is completely contactless. In order for it to be possible for power to transfer over a contactless interface, that DC power must first be converted in AC and then let the principles of Maxwell's equations (1.1-1.4) do the rest. The part of the system that converters DC-to-AC is called the inverter and the part of the system that converts AC-to-DC is called the rectifier. The complete schematic for the NMC power connector is shown in Figure 5.7. Notice that this is a schematic diagram based on the general model for inductive μWPT for NMCs introduced in Chapter 1, Figure 1.11.

The inverter is based off the simple 555 timer circuit and it is configured as an astable multivibrator. It is what takes in the DC power and converts it into a pulsating square wave with a controllable duty cycle with R_1 and R_2. While there are many ICs that are more ideal to function

as an inverter for WPT systems such as the LTC4125 or other high performance monolithic full bridge resonant drivers, the 555 timer is easy to use and perfect for prototype demonstration. As can be seen from the schematic, the topology used is SS-Topology that resonates based on C_1 and L_1 and is designed to operate in accordance with Qi standards that was briefly discussed in Chapter 3, Section 3.1.2.

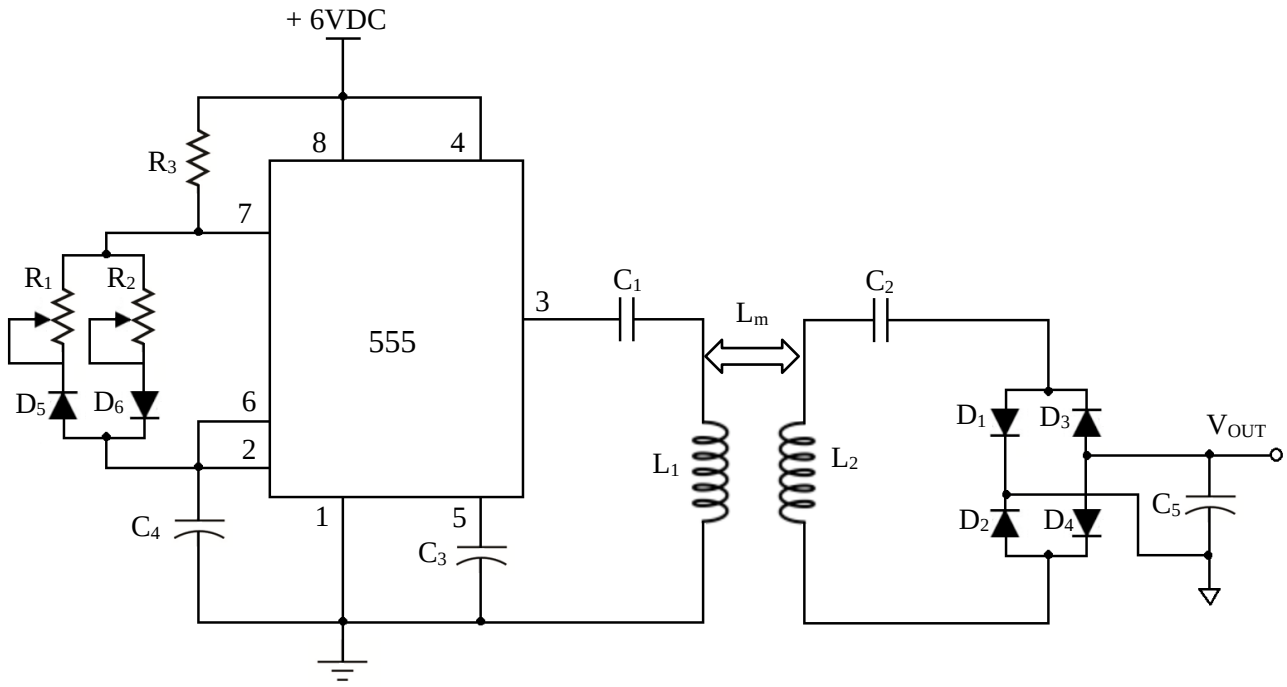

Figure 5.7: Inverter and rectifier circuits for NMC prototype

The rectifier circuit is even more simple than the inverter and is configured as a full bridge rectifier, a very commonly used configuration in power supplies. C_5 is a filter capacitor that helps smooth out the DC signal at V_{OUT}. Figure 5.8 shows what the input waveform as seen by Pin 3 looks like in addition to what the output looks like on the right side of C_2. This would be the output signal waveform before it gets rectified.

The top photo in Figure 5.8 below shows the complete experimental setup based on the

schematic in Figure 5.7. Each part was built separately and tested for functionality.

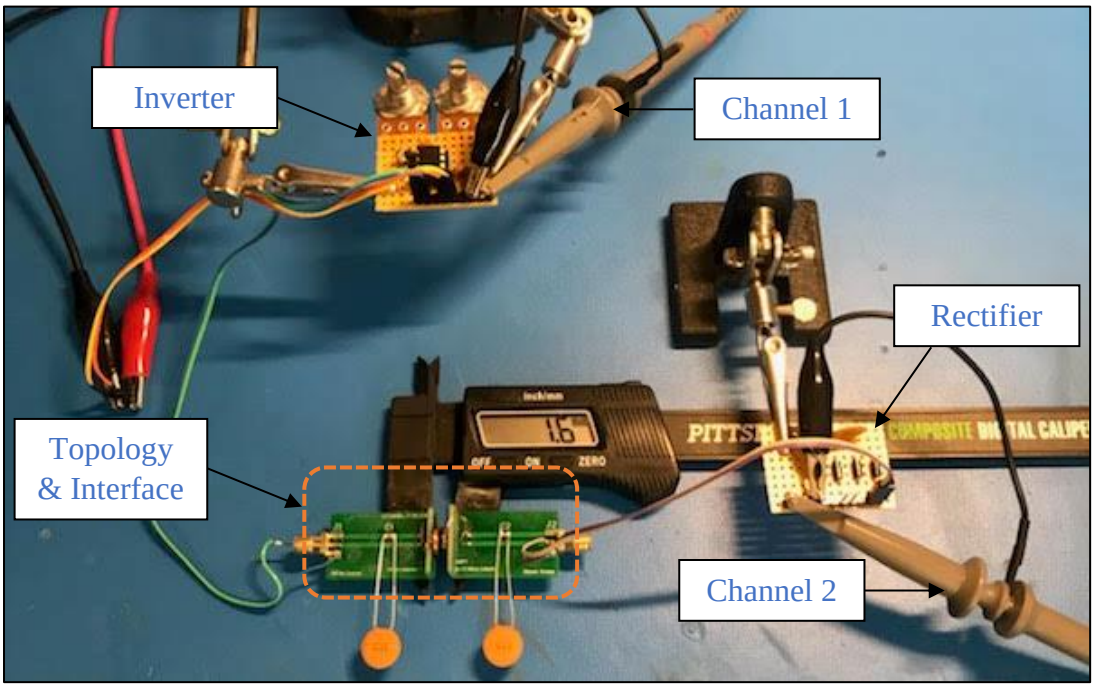

(a)

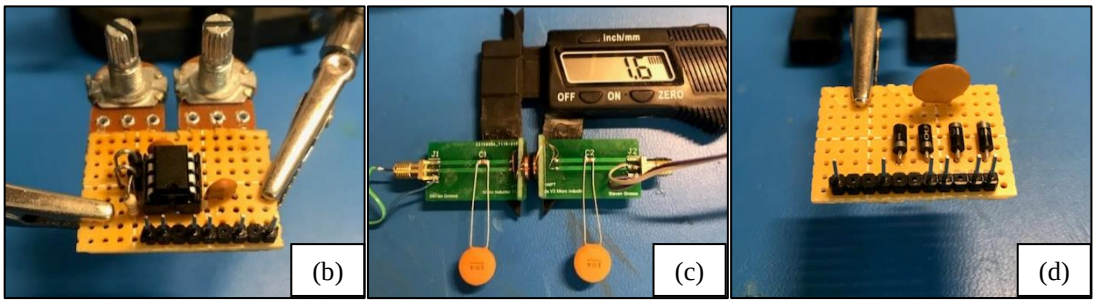

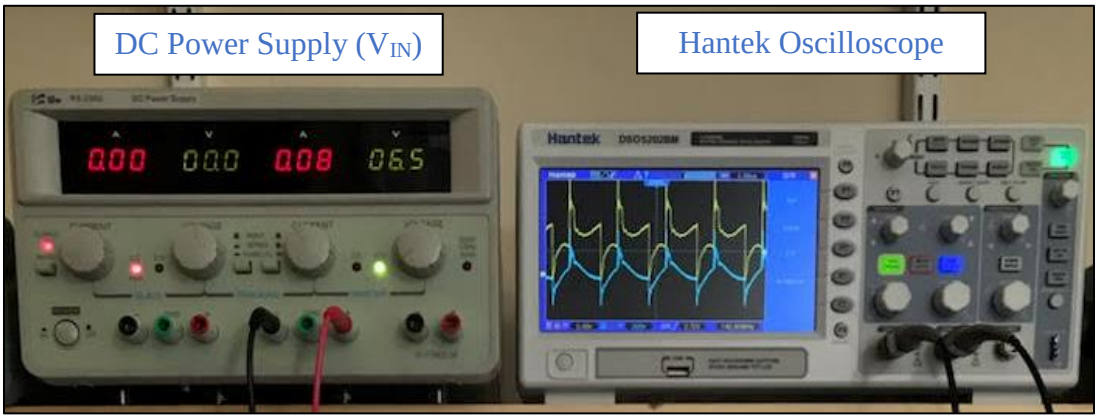

(e)

Figure 5.8: Complete experimental setup (a) showing (b) inverter, (c) topology & NMC interface, (d) rectifier circuits, and (e) the generated input and output waveforms

The input voltage was supplied by the DC Power Supply at 6.5 VDC and was the input to the inverter which was tuned to the frequency that would allow the LC tank based on SS-Topology to resonate at a frequency in accordance with the Qi standard. Specifically, the output frequency measured at Channel 2 on the rectifier output measured $f_0 = 147\ KHz$ which is within the range of that specification. In the setup shown, the separation distance between L_1 and L_2 was $g = 1.6\ mm$. Once the experimental setup was tuned, the oscilloscope was disconnected from the circuit and a Fluke DMM was connected to the rectifier output for a DC voltage measurement as shown in Figure 5.9.

Figure 5.9: Experimental setup connected to a DMM for a DC voltage measurement

This result is slightly off from what would be expected from Figure 4.21 showing the relationship between measured g and power transfer efficiency. According to the plot in Figure 4.21, with a separation distance of $g = 1.6\,mm$ it is expected that the efficiency of real transfer power to be around 73.8%. If we account for the voltage loss over the bridge rectifier circuit of 1.4 VDC and add this to the measured 3.592 VDC that is shown in Figure 5.9 for 4.992 VDC, we find that the power transferred is 76.8%, which is 5.0% greater than expected. To further verify the results from the Chapter 4, the potentiometers were adjusted and the system was fine-tuned even further. As a result, the frequency was increased to $f_0 = 175\,KHz$, and the following experiment was performed. Keeping the input voltage fixed at 6.5 VDC and using the setup in Figure 5.9, the separation distance was changed and the output voltage recorded for each of the 12 data points taken previously in Table 4.7. For each measurement instance, the measured voltage (V_{meas}) values were recorded at each separation distance. Photos of each of these instances are recorded and can be found in Appendix C. The actual voltage (V_{act}) in Table 5.1 is the voltage that is transferred over the air gap before entering the bridge rectifier and realizing the 1.4 VDC loss.

Table 5.1: Measured Output Voltage for Each Distance Point @ $f_0 = 175\,KHz$

g [mm]	V_{meas} [VDC]	V_{act} [VDC]	η_{meas} [%]	η_{exp} [%]	δ [%]
1.2	3.752	5.152	79.26	75.56	-3.70
1.4	3.413	4.813	74.04	74.80	0.76
1.6	3.128	4.528	69.66	73.85	4.19
1.7	3.075	4.475	68.84	72.53	3.69
1.9	2.985	4.385	67.46	70.33	3.07
2.1	2.697	4.097	63.03	66.06	3.03
2.3	2.419	3.819	58.75	64.35	5.60
2.5	2.192	3.592	55.26	59.91	4.65
2.7	2.021	3.421	52.63	56.81	4.18
2.9	1.798	3.198	49.20	52.84	3.64
3.1	1.606	3.006	46.24	50.11	3.87
3.5	1.274	2.673	41.12	43.50	2.38

When calculating the percentage difference (η_{meas}) for each measured data point it was found to be in good agreement with the expected (η_{exp}) power transfer efficiency in Figure 4.21. The difference between expected and measured efficiency ($\boldsymbol{\delta} = \eta_{exp} - \eta_{meas}$) is also quantified in the table. For a visual graph for how this data compares to the data in Figure 4.21, both sets of data are plotted in Figure 5.10.

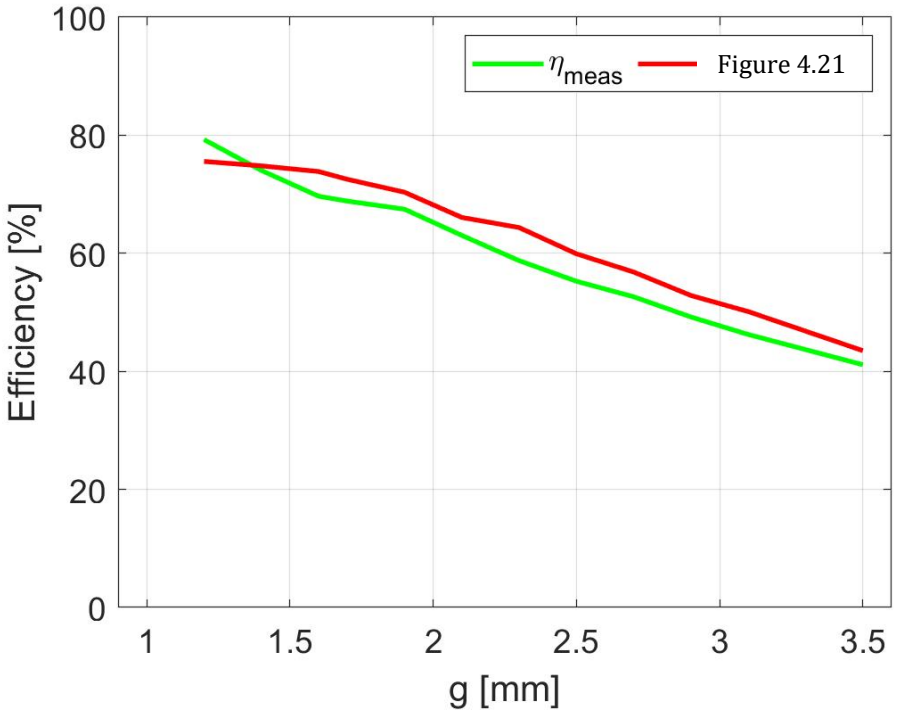

Figure 5.10: Comparison between η_{meas} and Figure 4.21 data

As can be seen from Table 5.1 and Figure 5.10, the $\boldsymbol{\delta}$ difference between expected and measured efficiency was not off by very much. On average, the difference was 2.94 percentage points with a standard deviation of 2.41. Knowing what to reasonably expect in terms of performance, it is now time to integrate/embed the inverter, topology, and rectifier into the 3D printed prototype model designed in Figures 5.1-3 and test it.

5.1.4 The Prototype Final Test and Demonstration

The NMC prototype in Figure 5.1 has a cylindrical geometry and was chosen for ease of assembly with the inductors which was in this case Archimedean spiral. Note that in practice, this typically would be the other way around where a customer would require all components be fitted within certain geometric constraints. But for now, that matters not for the purpose of this demonstration. Figure 5.11 shows the actual 3D printed power NMC. This prototype has all the components outlined in Figure 5.8 miniaturized and fitted inside the housings and then potted so that both receptable and plug are hermetically sealed just as desired. Both $L1$ and $L2$ are positioned in the front according to the model in Figures 5.2 and 5.3 so that when mated, the two inductors are axially aligned just as was designed. Notice that there are no mechanical latches to hold the plug and receptacle together; they are replaced instead by magnets as discussed previously.

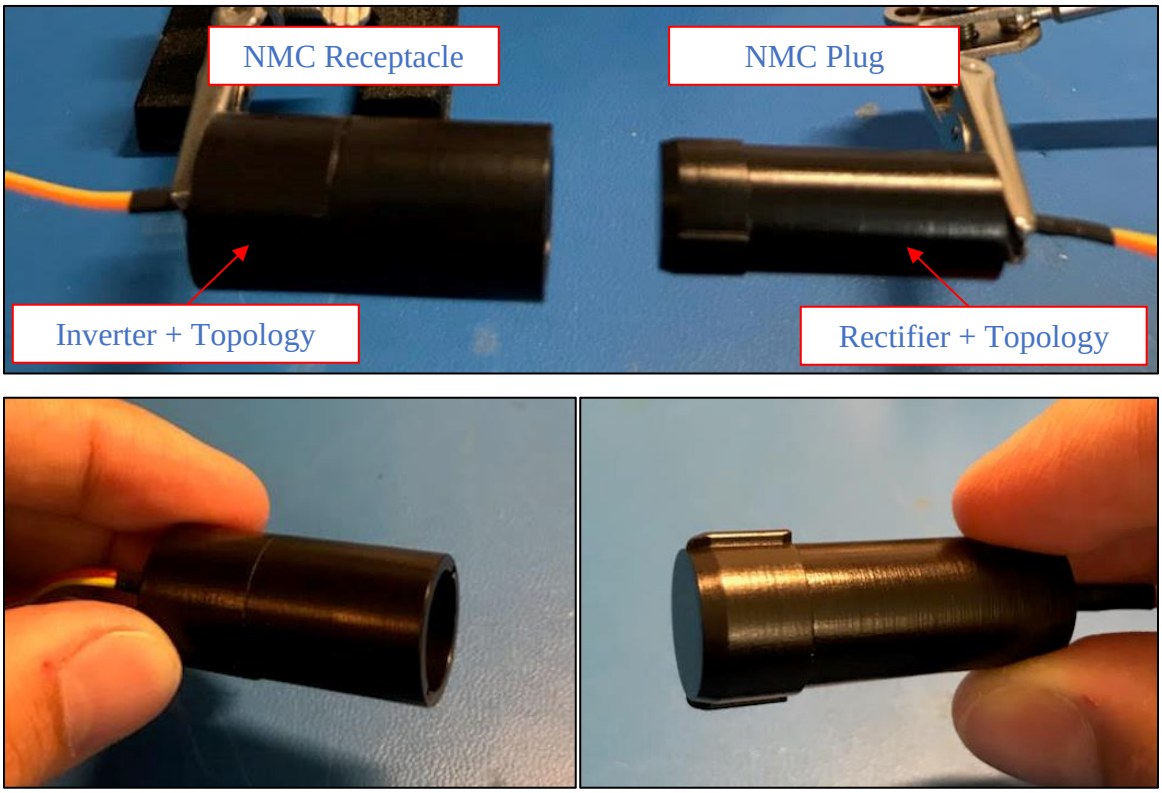

Figure 5.11: Actual 3D printed NMC prototype

(a)

(b)

Figure 5.12: NMC prototype (a) unmated showing no power and (b) mated showing power flow

As for a demonstration of functionality, Figure 5.12 above shows the NMC prototype with the receptacle connected to a power source supplying 6.5VDC and a DMM connected to the plug measuring the final output. As can be seen in Figure 5.12a, no power obviously will flow when the connector is not in a matted condition, and in 5.12b power begins to flow when they are mated thus the proof-of-concept demonstration is complete.

Because this connector is an NMC, it does not have electrical contacts or mechanical contacts. Therefore, all the common problems with standard connectors that was briefly discussed in Section 1.2.1 do not apply here. They are eliminated and thus are better suited for applications in harsh environments or in places where water and moisture are prevalent. In addition, due to the usage of magnets that can be designed to simulate or obtain any required retention force, there are unlimited insertion/durability cycles this connector can withstand do to the fact that there are no mechanical latches. As a demonstration of these points, Figure 5.13 shows the NMC prototype completely submerged under water while fully electrified. The prototype can be left in this condition indefinitely, undergo repeated insertion cycles while submerged and still show no signs of water ingress with no observed signs of performance loss.

Figure 5.13: NMC prototype submerged under water with no water contamination

5.2 Other NMC Applications Using µWPT

5.2.1 The NMC USB Flash Drive

This chapter demonstrated a very basic NMC concept to show how the concepts of WPT can be applied and integrated into a connector application. However, it did not even touch on the topic of signal transfer which is just as important as power transfer. The demand for higher data rates in the consumer electronics industry continues to increase and so does the need to improve and maintain power and signal integrity in the connecting mechanism between two subsystems of an electrical device. An example of another NMC application that does both power and signal transfer is applied to USB and the model is presented below in Figure 5.14 for an NMC flash drive [40]. The application transfers power and signal over the same contactless inductive interface. The problems this application would solve for the end user would be zero risk of device failure and loss of data due to exposure to water, one of the primary concerns for consumers for such a device. With the benefits the NMC brings, this concern is eliminated. USB C, Lightening Bolt, HDMI, etc. are other connector examples in the consumer electronics industry that NMC technology would benefit. Applications such as iPhones and tablets are examples NMCs could find relevance.

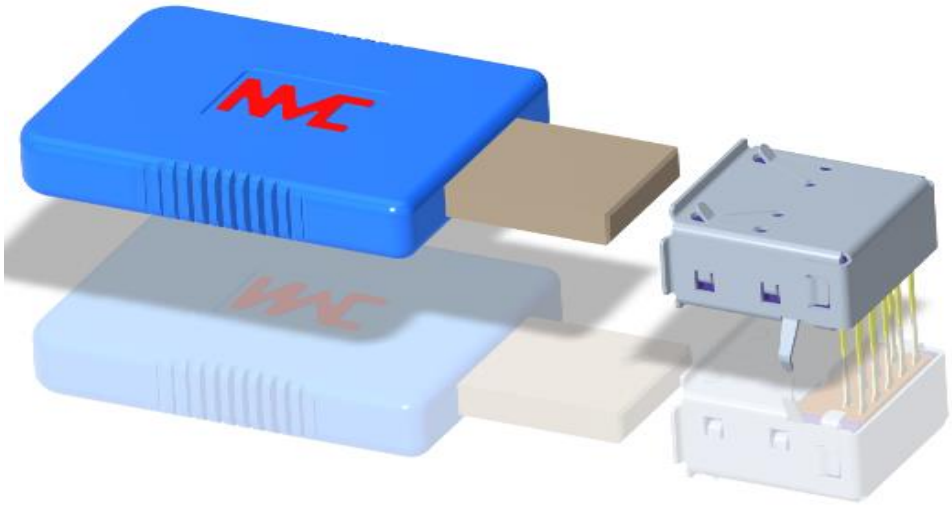

Figure 5.14: NMC USB flash drive with power and signal transfer

5.2.2 The NMC Light Bulb and Socket

Another NMC example application is the NMC light bulb and socket [41] shown in Figure 5.15 and the idea behind the design is for it to have the same form, fit, and function as standard light bulbs and sockets do without the problems. This prototype delivers the same light output as standard LED light bulbs do, but simply operates on different physics. The benefits the NMC brings to this industry and to the end user is a waterproof light bulb and socket – making it more sustainable for outdoor use – that is shock free. In addition, all the "smart" capabilities found in the smart bulbs selling on the market today can be integrated with the NMC socket. Rather than having the smart capability that allows the user to control the device with a smartphone be contained in the bulb that lasts only 7 years before the LED array burns out, that same capability is now embedded in the NMC light socket that will outlast the light bulb.

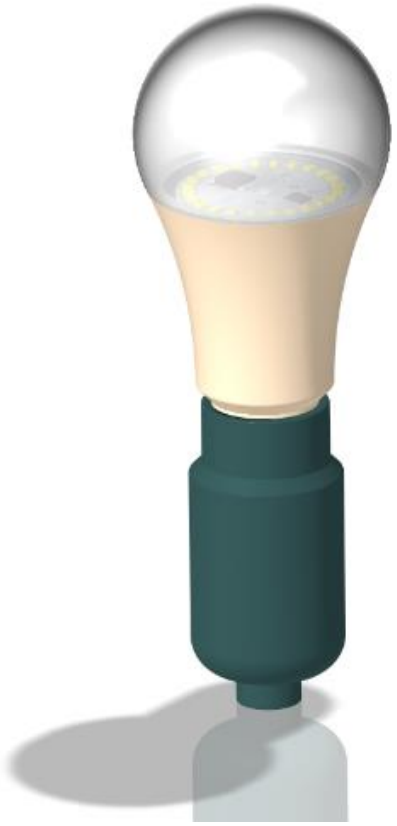

Figure 5.15: NMC light bulb and socket based off inductive power transfer

5.3 The Larger Vision for NMC and µWPT

The potential for µWPT and the NMC concept is enormous. Consider the proposition of this thesis that was later demonstrated in the form of a functional NMC prototype along with the two other NMC applications just introduced. Consider also that in the development/engineering of any new concept there will be problems that pose challenges in the process of implementation. The NMC is no different. There will be challenges in its implementation too, but the benefits that it brings could be worth it.

Let us consider an application that operates in harsh environments, that are difficult to service, and are subject to the effects of standard electrical contacts as discussed in the opening chapter. One of those applications are solar panels. The solar power industry is exploding with demand as a renewable energy source which has formed a major bulk of the developed world's infrastructure that continues to expand in the developing world. Yet, there is one downfall that all solar panels share: exposed metal contacts. The problems for solar and photovoltaic cells become amplified in extreme environmental conditions as typical polymeric coating found on solar panels are significantly degraded by UV and acidic rain that impacts sustainability. The solar power industry is constantly looking for new ways to improve reliability. Many academic journals are saturated with papers that attempt new ways of improving these problems. One of the areas of improvement for sustainability reside in the types of materials used to plate the electrical contacts on solar panels; these also have limitations and at best can achieve a lifespan of 25 years [42] before corrosion and other environmental factors takes its toll. As argued in [20] and [29], the best way to eliminate the problems associated with electrical contacts is to eliminate them completely. The solar power industry needs the NMC.

While the solar power industry can certainly benefit from the corrosion problem being

solved here on Earth in the more than 2,500 utility-scale solar farms, the space industry can also benefit. Consider the harsh environments in space and the thousands of satellites in orbit around the Earth. Satellites are critical for military use, for predicting weather, and for communication systems back on Earth; suffice it to say satellites are extremely important in helping humanity advance and maintain the modern standard of living that we do. The primary source of power generation used on satellites are solar panels and they must be able to withstand some harsh environmental extremes. Temperature extremes in low orbit can fluctuate anywhere between subzero temperatures and reach well over 125 ºC depending on where a satellite is in orbit. In addition to temperature fluctuations there also is corrosion in space caused by UV and X-rays or other high energy charged particles that impact electrical contacts. Many sources point to links between such corrosion and the risk of arc faults in PV systems' electrical connections and new nanocomposite films are being developed to help reduce these impacts and improve reliability [43], [44]. This is the current state of the art with no end in site because there currently exists no other alternative or mechanism besides electrical contacts for allowing current flow from the solar panel and to the satellite system it powers. The NMC can be an alternative mechanism and a possible solution.

Currently, there are about 6,000 satellites orbiting the earth (illustrated in Figure 5.16) [45], [46] and 60% of those are defective and no longer work. Satellites will be launched at a rate of more than 1000 each year which means over the next 10 years there will be as estimated by Euroconsult 16,000 of them in orbit by 2030. As mentioned earlier, solar panels are the only source of power generation and supply for satellites and the corrosion that builds up on solar panel contacts in space are often the root cause of failure. The best way to solve this problem in sustainability is not to replace the expensive solar panels once every 25 years but to instead apply

another mechanism that would eliminate this concern entirely. By applying methods of coupling as that principle mechanism of power transfer rather than relying on metal-to-metal electrical contacts this could be achieved. The coupling method that is the most feasible for solar applications would be capacitive coupling and would be based off the model illustrations in Figures 1.8 and 1.9. To implement this, there are a few modifications that must be made to solar panel structure in order to integrate NMC technology onto it.

Figure 5.16: Satellites in orbit [45]

Figure 5.17 shows a version of the basic internal structure for a solar panel and where the modifications on it would be if the NMC were to be used. Looking down at the panel, the first two layers are the frame and glass which provide the main protection for the overall structure. The individual solar cells as can be seen from the Figure are sandwiched between two encapsulants (Encapsulant 1 and Encapsulant 2) followed by a durable back sheet or substrate. In order for the capacitive NMC model to work and provide all the insulating properties to solar panels that is desired, the DC power that is generated by the silicon-based solar cells must first be converted into

AC power in order for that power to propagate through the insulating dielectric that is layered over the solar panel metallic sheets.

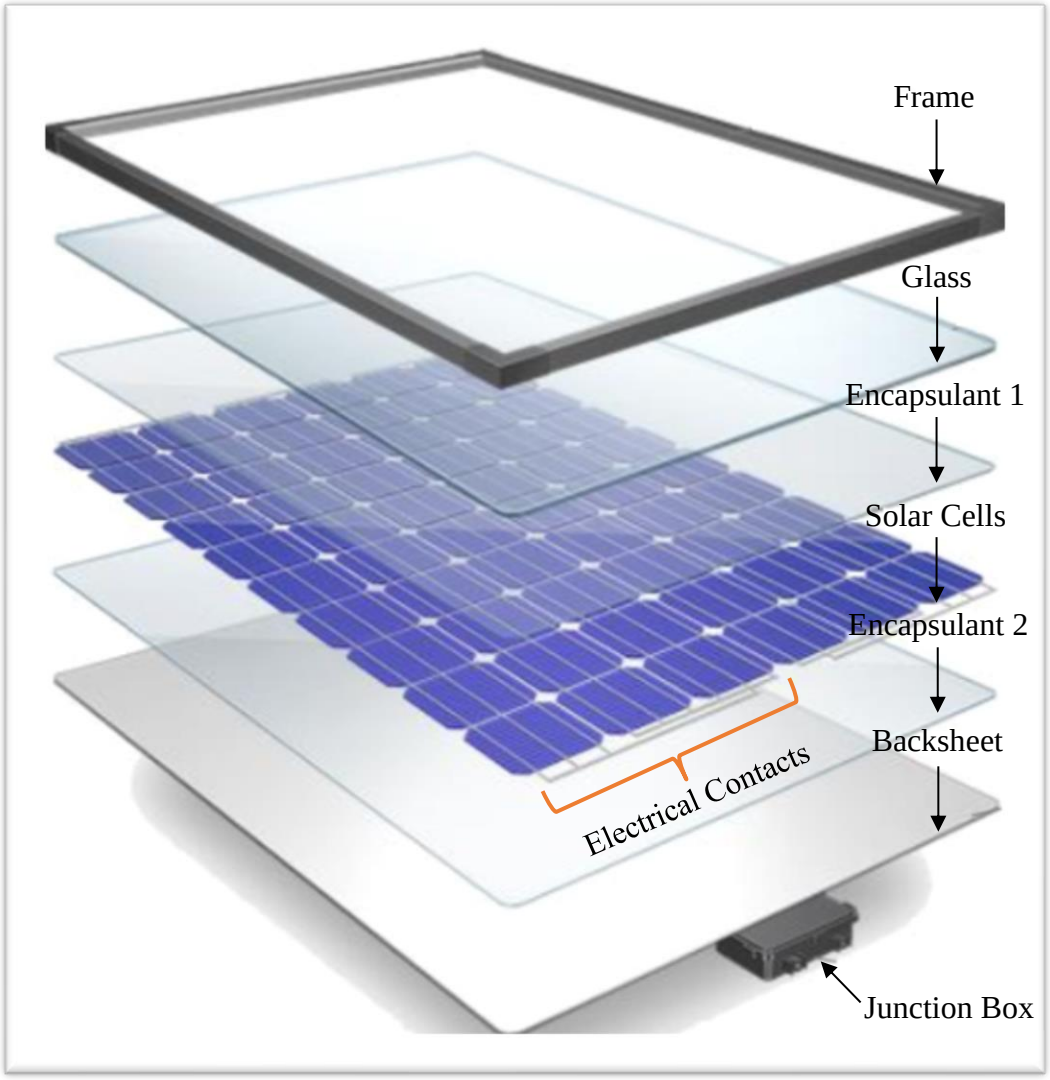

Figure 5.17: Internal structure of solar panel [43]

As the high-level NMC model for capacitive coupling in Figure 1.8 shows, and in order to apply that model to this application, there needs to be both a T_X and R_X metallic plate that makes electrical contact as the common nodes for individual solar cells with T_X and R_X dielectric material deposited over them, thus insulating them completely.

The vision for this new solar panel works something like the following. The DC power that

is natually generated by each individual cell inside the panel must be converted into AC by an inverter/multivibrator or ocsillator circuit that would be fabricated into the silicon of each solar cell. The intention would be to make it a part of it. That is, each solar cell would have its own inverter that when connected or dazy chained in some configuration with N number of solar cells, the total AC power ouput would be the sum of the individual cells. The inverter outputs would all rout to a common node plate that is metallic (following the model in Figure 1.9) that will be located on the edges of the panel itself for dielectric material to completely embed the node plates. When the solar panel is mated with a power cable, that power cable will be the reverse image of the node plate and also incapsulated in the same dielectric material. After being mated and connected to the solar panel, charge can flow from one side to the other as governed by Gauss's Law.

The AC solar panel makes NMC necessary. Without it, the AC solar panel would not otherwise work if the power ouput were DC power and therefore the NMC solar panel would always be an AC solar panel. It is also imporatnat to observe that an AC solar panel would eliminate the need for the junction box since the purpose of it is to do exactly what the individual inverters built into each solar cell do. New metamaterials likely would need to be developed as part of this implementation. This is only a concept to be explored in detail in later papers.

CHAPTER 6
Conclusion and Future Work on µWPT

In this thesis, the concept of µWPT was introduced, classified on the WPT hierarchy, and condensed in size to the point where inductive coils are small enough to be used in connector applications. Important parameters that are crucial to power transfer efficiency were identified and related to separation distance utilizing the Neumann formula followed by extensive mathematical derivations of inductor geometry and it was investigated how different inductor geometries impact those critical parameters. This was followed by yet more exhaustive mathematical derivations on the four basic circuit topologies for WPT systems and ADS simulations of both. It was identified that the best topology that gives rise to the greatest margin of power transfer efficiency is SS-Topology. Identifying this topology was made while comparisons were also made to the benefits and disadvantages of the other three topologies. And finally, SS-Topology was tested with measurements using a VNA and compared to ADS simulations over different separation distance points. In the process of doing this, an important realization was made in that there was no way to simulate g while it was possible to simulate for k in ADS. The reverse was also observed in that there was no way to measure k with a VNA while it was possible to measure g. In this thesis, a method for doing both was presented showing how accurate derivations for L_m is critical for a particular inductor geometry using the Neumann formula which was used to connect k and g in both cases. Lastly, the contribution that provides the motivation for µWPT in the first place was how it can be applied to the connector industry which ultimately opens the door to a new generation of connectors and connector concepts called the NMC. An example NMC protype was designed and tested which validated the feasibility of µWPT and how it can be applied to connectors.

This research has opened the door for a lot of immediate future work. One of those

continuing topics that is worth investing more research into is how Q-factor (equation 4.3) improves power transfer efficiency. During the process of conducting this research, several Archimedean spiral inductors were tested and studied that had different parameter values for parasitic resistance, R. The lower resistive values showed better results in power transfer efficiency which theoretically would make sense given the inverse relationship between parasitic resistance and Q-factor. The future research in this area would be to investigate and compare different inductors of the same geometry with different resistance values. For connector applications, inductor size matters and to that end it would be good to also investigate how small inductors can be made and still give rise to pragmatic separation distance margins. This distance margin is critical for NMC applications since it would give designers the ability to know how much separation distance is possible without sacrificing too much efficiency to meet a customer's needs. As we have seen, inductor geometry is critical to determining L_m, but there is an open question about the radius of the inductor that could benefit from some additional research. In the Archimedean setup in Figure 2.4, the question is how the specific parameters for inner radius ($\boldsymbol{R_i}$) and screw pitch ($\boldsymbol{s}$) impact power transfer efficiency for the same outer diameters ($\boldsymbol{R_o}$). The inductors in this thesis were procured from suppliers that specialize in inductor coil applications.

Increasing the operating frequency also is a critical parameter that impacts Q-factor positively and would be a part of this future research. The open question to be answered with future research in this area is how a performance plot such as Figure 4.21 change at different frequency values. It is postulated that there would be an increase in power transfer efficiency at higher frequencies per equation (4.3), but by how much is the open question. Analysis is needed to adequately answer how much it would. Along these same lines, it would also be beneficial to investigate other core materials besides an air core. In this thesis, only inductors with an air core

were investigated and since the self-inductance is one of the critical parameters that directly impact separation distance margin, core materials that increase the self-inductance should also be looked at closely. It is possible that in order to obtain certain performance characteristics for a given application that a metamaterial may need to be created in order to give rise to the performance required for that application. Finding that metamaterial could open up a new research frontier all on its own.

In this thesis, only SS-Topology was investigated with experimental measurements and compared with ADS simulations. Future research work on this topic would certainly be to investigate the other three topologies in the same way with measurements and validate simulations. Further research in applying techniques of impedance re-normalization, briefly mentioned in Section 4.2.2, for each topology would be instrumental in helping to improve the correlation between measurement and simulation even more.

There is a new area of research that investigates 3D printing microelectronic components on a substrate including inductors. Another area of expanding this research would certainly be in the area of looking into utilizing this new technology and testing them in μWPT systems and NMCs.

Another topic for future work in this area is how small variations in connector housings and tolerance impact power transfer efficiency. While the connector housings fixture the two inductors to be axially aligned that eliminates the standard WPT concerns of lateral and angular misalignment concerns, it turns out that those concerns may not be completely eliminated and this is especially true if one of the other three topologies is used that is more volatile than SS-Topology. During manufacturing of these housings there will be tolerance variation between them as they come out of the mold. This variation therefore would be random or stochastic, but the question

again becomes how that variation in connector housing tolerance derives or translates into power transfer efficiency, the most critical parameter for any μWPT system or application. The problem then becomes relating a stochastic process in housing tolerance to power transfer efficiency.

For connector applications specifically, it is often the case that signal and power operate within the same package. This thesis focused on μWPT for power applications only. Future work would investigate how power and signal can operate together over a single inductive interface, a single capacitive interface, or some hybrid combination of them with optical signal transfer. This would introduce a new term similar to micro-Wireless Power Transfer and become micro-Wireless Signal Transfer (μWST) and for hybrid applications that utilize both, micro-Wireless Power-Signal Transfer, or μWPST. Capacitive coupling can also be used as an interface for both power and signal. For connector applications that require multiple insertion cycles, the wear properties on the insulating dielectric material would need to be of a certain order to withstand a high number of insertion cycles and still be able to perform well by not degrading other critical material properties. A new class of metamaterials needs to be developed for this as well and tested.

Appendix A – Biot-Savart Law Square and Hexagonal Mathematical Analysis

A.1 Square Loop

The same approach for obtaining an expression for magnetic field strength for a circular loop can also be applied to a square loop since the physics is the same as shown in Figure A.1.

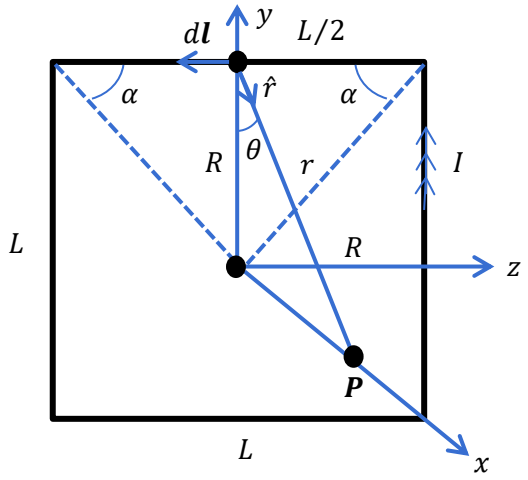

Figure A.1: Square current path setup for Biot-Savart Law derivation

There are four identical wires to consider and each one has the same impact at the origin. So, we write:

$$\tan(45°) = \frac{R}{(L/2)} = \frac{2R}{L} = 1 \tag{A.1}$$

$$L = 2R \tag{A.2}$$

The square loop lays in the yz-plane, is centered at x, and has a point $\boldsymbol{P}$ extending out of the page. It is well established that the current I traveling around a conductive wire loop has a corresponding B-field that is perpendicular to its flow. In looking at a small section of that wire, $\boldsymbol{dl}$, which I is flowing through, an expression for the magnetic field intensity generated by dl can be defined as: $d\boldsymbol{B} \perp |d\boldsymbol{l} \times \hat{r}|$ and means the magnetic field is perpendicular to both that small section of wire and the unit vector pointing towards point $\boldsymbol{P}$. In all three geometries being compared (circular, square,

and hexagonal), r is the same in all cases: $r^2 = x^2 + R^2$ where r is the distance from point $\boldsymbol{P}$, $\hat{r}$ is the unit vector pointing towards it and R is the square length of each side.

$$d\boldsymbol{B}_X = \frac{\mu_0 I}{4\pi} \cdot \frac{|d\boldsymbol{l} \times \hat{r}|}{r^2} = \frac{\mu_0 I}{4\pi} \cdot \frac{|d\boldsymbol{l} \times \hat{r}|}{x^2 + R^2} \tag{A.3}$$

We can now integrate around the square loop to find the total impact of the enclosed circuit about point $\boldsymbol{P}$:

$$\begin{aligned} \boldsymbol{B_X} = \oint d\boldsymbol{B_X} &= \frac{\mu_0 I}{4\pi} \oint \frac{|d\boldsymbol{l} \times \hat{r}|}{x^2 + R^2} \\ &= \frac{\mu_0 I}{4\pi(x^2 + R^2)} \cdot \oint cos\theta d\boldsymbol{l} \\ &= \frac{\mu_0 I}{4\pi(x^2 + R^2)} \cdot \oint \frac{R}{(x^2 + R^2)^{1/2}} d\boldsymbol{l} \\ &= \frac{\mu_0 IR}{4\pi(x^2 + R^2)^{3/2}} \cdot \oint d\boldsymbol{l} \\ &= \frac{\mu_0 IR}{4\pi(x^2 + R^2)^{3/2}} \cdot 8R \\ &= \frac{2\mu_0 IR^2}{\pi(x^2 + R^2)^{3/2}} \end{aligned} \tag{A.4}$$

At $x = 0$, equation (A.4) becomes:

$$\boldsymbol{B_{X\_S}} = \frac{2\mu_0 I}{\pi R} \tag{A.5}$$

And finally, we once more apply the same analysis to the hexagonal loop for obtaining an expression for magnetic field strength. The geometric setup is presented in Figure A.2.

A.2 Hexagonal Loop

Once again, the reasoning is the same here like in the previous two cases. In this case, the hexagon is divided up for simplicity in the calculation. Not that the x-axis is pointing out of the page and that at $x = 0$, the $\vec{\boldsymbol{B}}$-field represents the magnitude at the shape center.

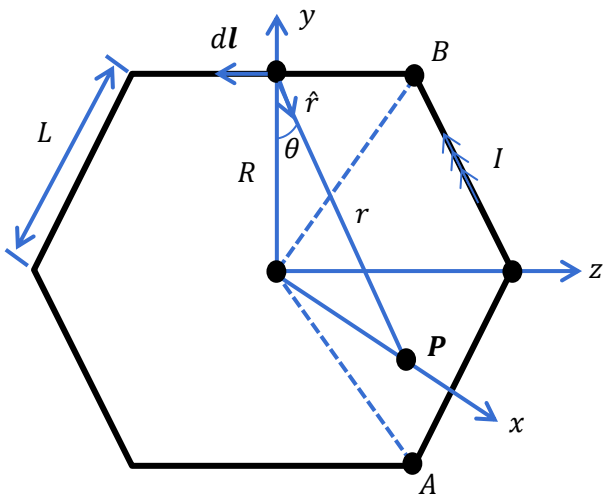

Figure A.2: Hexagonal current path setup for Biot-Savart Law derivation

We need to look at the hexagon geometry a little differently due to the nature of this shape which is obviously unlike the other. Consider the dotted lines from the origin to points A and B. They will geometrically help establish an expression for the field influence at each of the six points More specifically:

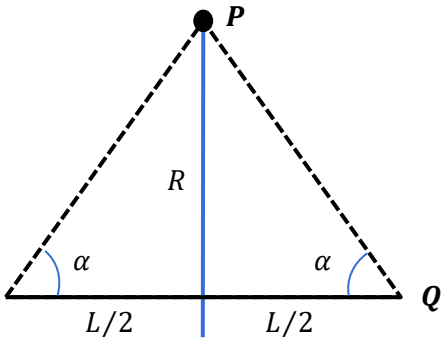

Figure A.3: Equilateral triangle within hexagonal loop

For a hexagon, $\alpha = 60°$. When $\alpha = 0°$, $B = \frac{\mu_0 I}{4\pi}$ and for $\alpha > 0$, $\boldsymbol{B} = \frac{\mu_0 I}{4\pi} cos\alpha$. We are specifically concerned with the end point, $\boldsymbol{Q}$. This is a 30-60 triangle where $R = \frac{\sqrt{3}}{2} L$, and $\overrightarrow{PQ} = L$. This makes sense geometrically in light of the fact a hexagon can be thought of as placing six equilateral triangles together.

As before, $d\boldsymbol{B_X} \perp |d\boldsymbol{l} \times \hat{r}|$ and $r^2 = x^2 + R^2$ so that:

$$d\boldsymbol{B_X} = \frac{\mu_0 I}{4\pi} \cdot \frac{|d\boldsymbol{l} \times \hat{r}|}{r^2} = \frac{\mu_0 I}{4\pi} \cdot \frac{d\boldsymbol{l}}{(x^2 + R^2)} = \frac{\mu_0 I d\boldsymbol{l}}{4\pi(x^2 + R^2)} \tag{A.6}$$

Therefore:

$$\begin{aligned} \boldsymbol{B_X} = \oint d\boldsymbol{B_X} &= \oint \frac{\mu_0 I d\boldsymbol{l}}{4\pi(x^2 + R^2)} \\ &= \frac{\mu_0 I}{4\pi(x^2 + R^2)} \cdot \oint d\boldsymbol{l} \\ &= \frac{6\mu_0 IL}{4\pi(x^2 + R^2)} \\ &= \frac{\sqrt{3}\mu_0 IR}{\pi(x^2 + R^2)} \end{aligned} \tag{A.7}$$

It is interesting to observe when $x = 0$ that this will be the magnitude of $\boldsymbol{B}$ at the center of the hexagonal loop. In this case, we have:

$$\boldsymbol{B_{X\_H}} = \frac{\sqrt{3}\mu_0 I}{\pi R} \tag{A.8}$$

Appendix B – MATLAB Code

B.1 Code for comparing three geometries for magnetic field intensity

```
close all
clear all
% Define all fixed parameter values
mu0 = (4*pi*(1e-7));
I = 3; % This is the current in the loop
R = (30*(1e-2)); % This is the radius or midpoint
x=-2:0.001:2;
% Insert the equation for a Archemedian circle loop
C = (mu0*I*(R.^2))./(2*(((x.^2)+(R.^2)).^(3/2)));
C = (C)*100000;
% Insert the equation for a Square loop
S = (2*mu0*I*(R.^2))./(pi*(((x.^2)+(R.^2)).^(3/2)));
S = (S)*100000;
% Insert the equation for a Hexagonal loop
H = (sqrt(3)*mu0*I*R)./(pi*(((x.^2)+(R.^2))));
H = (H)*100000;
% Plot all three graphs together
a=plot(x,C,x,S,x,H);grid on
a(1).LineWidth = 2;
a(2).LineWidth = 2;
a(3).LineWidth = 2;
xlabel('x [cm]', 'FontSize', 18);
xlim([-1 1]);
ylabel('Bx [uT]', 'FontSize', 18);
ylim([0 1]);
set(gca, 'FontSize', 18);
legend('Circular', 'Square', 'Hexagonal');
```

B.2 Archimedean Spiral System for Figure 2.5

```
% EE600 - Thesis Research - 02/07/2021
% uWPT system simulation with two Archimedean spiral inductors
% Set design frequency and system parameters:
fc=30e6;
fcmin = 28e6;
fcmax = 31e6;
fband1 = 27e6:1e6:fcmin;
fband2 = fcmin:0.25e6:fcmax;
fband3 = fcmax:1e6:32e6;
freq = unique([fband1 fband2 fband3]);
pt=linspace(-0.3,0.3,61);
[X,Y,Z]=meshgrid(pt,0,pt);
field_p=[X(:)';Y(:)';Z(:)'];
% Create spiral geometry defined by the inner and outer
% radius and the number of turns, N.
Rin=0.05;
Rout=0.15;
N=6.25;
spiralobj = spiralArchimedean('NumArms', 1, 'Turns', N,              ...
    'InnerRadius', Rin, 'OuterRadius', Rout, 'Tilt', 90, 'TiltAxis', 'Y');
% Plot the system impedance to understand the resonant frequency of
% the spiral geometry.
figure;
impedance(spiralobj,freq);
% Plot the near field in order to see the dominant field component
% of the resonance.
figure;
EHfields(spiralobj,fc,field_p,'ViewField','H','ScaleFields',[0 5]);
% Create the actual Archemedean spiral system with both Tx and Rx.
wptsys=linearArray('Element',[spiralobj spiralobj]);
wptsys.ElementSpacing=Rout*2;
figure;
show(wptsys);
% Calculate the system efficiency S21 with with separation distance.
sparam = sparameters(wptsys, freq);
figure;
rfplot(sparam,2,1,'abs');
% Perform a parametric study of the system s-parameters as a function of
% the transfer distance in order to understand the critical coupled point.
freq=(25:0.1:36)*1e6;
dist=Rout*2*(0.5:0.1:1.5);
load('wptData.mat');
s21_dist=zeros(length(dist),length(freq));
for i=1:length(dist)
    s21_dist(i,:)=rfparam(sparam_dist(i),2,1);
end
figure;
[X,Y]=meshgrid(freq/1e6,dist);
surf(X,Y,abs(s21_dist),'EdgeColor','none');
view(150,20);
shading(gca,'interp');
axis tight;
xlabel('Frequency [MHz]');
ylabel('Distance [m]');
```

```
zlabel('S_{21} Magnitude');

% Plot the coupling mode between two spiral resonators in order to
% understand the dominant energy exchange between the two resonators
% which is always through the magnetic field. Strong magnetic fields
% are present between the two spirals at resonant frequency.
wptsys.ElementSpacing=Rout*2;
figure;
EHfields(wptsys,fc,field_p,'ViewField','H','ScaleFields',[0 5]);
view(0,0);
```

B.3 Neumann Formula for Equation 2.30

```
% EE600 - Thesis Research - 02/08/2021
% Neumann formula numerically plotted for two identical spiral inductors
% that each have a self-inductance of 18µH with and inner and outer radius
% of Ri = 4mm and Ro = 8.3mm, respectively. Screw pitch is 0.3215mm and
% the simulation is run from 0 to 20mm separation distance. This simulation
% is based off Wurth Elektronik WE-WPCC Wireless Power Transfer Tx and Rx
% coil Part No. 760308101208A.

close all
clear all
mu0 = (4*pi*(1e-7));
mur = 1;
mu = mu0*mur;
g=0:0.1:20; % Let the separation distance, g, sweep from 0 to 3 mm.
g=g/1000;
% Define the screw pitch which is the same for both inductors. Therefore,
% this means s = s1 = s2.
s=0.3215/1000;
% Define the inner and outter radius of the spirals. Again, since both
% inductors are the same, Ri = Ri1 = Ri2 and Ro = Ro1 = Ro2. Ri and Ro are
% set for 2mm and 6mm, respectively.
Ri=0.004;
Ro=0.0083;
% Define parameters a = a1 = a2.
a=(s./(2*pi));
% Define angles phi_i = phi_i1 = phi_i2 and phi_o = phi_o1 = phi_o2
phi_i=(Ri/a);
phi_o=(Ro/a);
N=4; % Number of inductor turns, N
% Simulation of the Neumann Formula begins here.
lgap=length(g);
Lm=zeros(1,lgap);
for l=1:lgap
    Lm(l)=0;
    k=1;
    % Set the limits of integration from phi_i to phi_o
    for theta1=phi_i:0.1:phi_o
        theta2=phi_i:0.1:phi_o;
        num=((1+(theta2*theta1)).*cos(theta2-theta1)-((theta2-
theta1).*sin(theta2-theta1)));
        den=sqrt(g(l)^2+((a^2)*(((theta1.^2)+(theta2.^2))-
((2*theta1*theta2).*(cos(theta2-theta1))))));
        inner=num./den;
        myinnint(k)=trapz(theta2,inner);
        k=k+1;
    end
    theta1=phi_i:0.1:phi_o;
    % Neumann final result
    L(l)=N*((a^2)*(mu/(4*pi))*trapz(theta1, myinnint));
end
% Plot Lm (in uH) vs. g (in mm)
x=g*1000;
y=L/1e-6;
p=plot(x,y);grid on
```

```
p(1).LineWidth = 2;
xlabel('g [mm]', 'FontSize', 18);
xlim([0 20]);
ylabel('Lm [uH]', 'FontSize', 18);
ylim([0 18]);
set(gca, 'FontSize', 18);
figure
% Plot coupling coefficient k vs. g (in mm)
w=y/(18);
q=plot(x,w);grid on
q(1).LineWidth = 2;
xlabel('g [mm]', 'FontSize', 18);
xlim([0 20]);
ylabel('k', 'FontSize', 18);
ylim([0 1]);
set(gca, 'FontSize', 18);
```

B.4 Data Processing MATLAB Script

```
% EE600 - Data processing script for topologies
% Joshua Benjestorf, Spring 2021, Penn State Harrisburg
% This script imports and processes data from Excel on
% four compensation topologies for uWPT systems. Plots for all four
% are presented individually and collectively for efficiency vs.
% coupling coefficient, k. The data is subsequently rescaled for
% mutual inductance vs. efficiency which can then be cross referenced
% with the Neumann formula for any inductor geometry to establish a
% relationship between separation distance, g, between two mutually
% coupled inductors vs efficiency.

%Read the Excel raw data files using readtable function
rawTableSS = readtable('dataSS.xlsx','Sheet','Sheet1');
rawTableSP = readtable('dataSP.xlsx','Sheet','Sheet1');
rawTablePS = readtable('dataPS.xlsx','Sheet','Sheet1');
rawTablePP = readtable('dataPP.xlsx','Sheet','Sheet1');

%Get the Excel column Header1 and Header2 from each table
x_SS = rawTableSS.Header1;
y_SS = rawTableSS.Header2;
x_SP = rawTableSP.Header1;
y_SP = rawTableSP.Header2;
x_PS = rawTablePS.Header1;
y_PS = rawTablePS.Header2;
x_PP = rawTablePP.Header1;
y_PP = rawTablePP.Header2;

%Plot the data for SS-Topology
a=plot(x_SS,y_SS);grid on
a(1).LineWidth = 2;
xlabel('k', 'FontSize', 14);
xlim([0 1]);
ylabel('Efficiency [%]', 'FontSize', 14);
ylim([50 100]);
set(gca, 'FontSize', 14);
figure;

%Plot the data for SP-Topology
b=plot(x_SP,y_SP);grid on
b(1).LineWidth = 2;
xlabel('k', 'FontSize', 14);
xlim([0 1]);
ylabel('Efficiency [%]', 'FontSize', 14);
ylim([50 100]);
set(gca, 'FontSize', 14);
figure;

%Plot the data for PS-Topology
c=plot(x_PS,y_PS);grid on
c(1).LineWidth = 2;
xlabel('k', 'FontSize', 14);
xlim([0 1]);
ylabel('Efficiency [%]', 'FontSize', 14);
```

```
ylim([50 100]);
set(gca, 'FontSize', 14);
figure;

%Plot the data for PP-Topology
d=plot(x_PP,y_PP);grid on
d(1).LineWidth = 2;
xlabel('k', 'FontSize', 14);
xlim([0 1]);
ylabel('Efficiency [%]', 'FontSize', 14);
ylim([50 100]);
set(gca, 'FontSize', 14);
figure;

%Plot all data on the same graph
e=plot(x_SS,y_SS,x_SP,y_SP,x_PS,y_PS,x_PP,y_PP);grid on
legend({'SS','SP','PS','PP'},'Location','northwest','NumColumns',4);
e(1).LineWidth = 2;
e(2).LineWidth = 2;
e(3).LineWidth = 2;
e(4).LineWidth = 2;
xlabel('k', 'FontSize', 14);
xlim([0 1]);
ylabel('Efficiency [%]', 'FontSize', 14);
ylim([50 100]);
set(gca, 'FontSize', 14);
figure;

%Plot mutual inductance, Lm, vs. efficiency
f=plot(x_SS*24,y_SS,x_SP*24,y_SP,x_PS*24,y_PS,x_PP*24,y_PP);grid on
legend({'SS','SP','PS','PP'},'Location','northwest','NumColumns',4);
f(1).LineWidth = 2;
f(2).LineWidth = 2;
f(3).LineWidth = 2;
f(4).LineWidth = 2;
xlabel('Lm [uH]', 'FontSize', 14);
xlim([0 24]);
ylabel('Efficiency [%]', 'FontSize', 14);
ylim([50 100]);
set(gca, 'FontSize', 14);
```

B.5 Data Processing MATLAB Script for ADS and VNA

```
% EE600 - Data processing script for both ADS simulations and
% VNA measurements. Both simulations and measurements were taken in
% the Spring 2021 semester at Penn State Harrisburg

%Read Excel raw data file using readtable function for Measured Data
rawTableS11_VNA = readtable('dataS11_VNA.xlsx','Sheet','Sheet1');
rawTableS21_VNA = readtable('dataS21_VNA.xlsx','Sheet','Sheet1');
%Read Excel raw data file using readtable function for Simulated Data
rawTableS11_ADS = readtable('dataS11_ADS.xlsx','Sheet','Sheet1');
rawTableS21_ADS = readtable('dataS21_ADS.xlsx','Sheet','Sheet1');

%Get the Excel column Header1 and Header2 from Measured data
x_S11_VNA = rawTableS11_VNA.Header1;
y_S11_VNA = rawTableS11_VNA.Header2;
x_S21_VNA = rawTableS21_VNA.Header1;
y_S21_VNA = rawTableS21_VNA.Header2;
%Get the Excel column Header1 and Header2 from Simulated data
x_S11_ADS = rawTableS11_ADS.Header1;
y_S11_ADS = rawTableS11_ADS.Header2;
x_S21_ADS = rawTableS21_ADS.Header1;
y_S21_ADS = rawTableS21_ADS.Header2;

%Plot the data for S11 Measured with VNA
g=plot(x_S11_VNA*1e-6,y_S11_VNA);grid on
g(1).LineWidth = 2;
xlabel('Frequency', 'FontSize', 14);
%xlim([0 1]);
ylabel('S_1_1 VNA [dB]', 'FontSize', 14);
ylim([-55 0]);
set(gca, 'FontSize', 14);
figure;

%Plot the data for S21 Measured with VNA
g=plot(x_S21_VNA*1e-6,y_S21_VNA);grid on
g(1).LineWidth = 2;
xlabel('Frequency', 'FontSize', 14);
%xlim([0 1]);
ylabel('S_2_1 VNA [dB]', 'FontSize', 14);
ylim([-40 0]);
set(gca, 'FontSize', 14);
figure;

%Plot the data for S11 Measured with VNA
h=plot(x_S11_ADS*1e-6, y_S11_ADS);grid on
h(1).LineWidth = 2;
xlabel('Frequency', 'FontSize', 14);
%xlim([0 1]);
ylabel('S_1_1 ADS [dB]', 'FontSize', 14);
ylim([-55 0]);
set(gca, 'FontSize', 14);
figure;

%Plot the data for S21 Measured with VNA
```

```
h=plot(x_S21_ADS*1e-6,y_S21_ADS);grid on
h(1).LineWidth = 2;
xlabel('Frequency', 'FontSize', 14);
%xlim([0 1]);
ylabel('S_2_1 ADS [dB]', 'FontSize', 14);
ylim([-40 0]);
set(gca, 'FontSize', 14);
figure;

%Plot both Simulated and Measured data S11 vs. frequency
i=plot(x_S11_VNA*1e-6,y_S11_VNA,x_S11_ADS*1e-6,y_S11_ADS);grid on
legend({'Measured','Simulated'},'Location','southeast','NumColumns',2);
i(1).LineWidth = 2;
i(2).LineWidth = 2;
xlabel('Frequency [MHz]', 'FontSize', 14);
%xlim([0 24]);
ylabel('S_1_1 [dB]', 'FontSize', 14);
ylim([-55 0]);
set(gca, 'FontSize', 14);
figure;

%Plot both Simulated and Measured data S21 vs. frequency
j=plot(x_S21_VNA*1e-6,y_S21_VNA,x_S21_ADS*1e-6,y_S21_ADS);grid on
legend({'Measured','Simulated'},'Location','southeast','NumColumns',2);
j(1).LineWidth = 2;
j(2).LineWidth = 2;
xlabel('Frequency [MHz]', 'FontSize', 14);
%xlim([0 24]);
ylabel('S_2_1 [dB]', 'FontSize', 14);
ylim([-40 0]);
set(gca, 'FontSize', 14);
```

B.6 Data Processing MATLAB Script for Comparing g vs k

```
% EE600 - Data processing script for comparing k-to-g and g-to-k

%Read Excel raw data file using readtable function for Measured Data
dataMeasured_VNA = readtable('CompareMeas.xlsx','Sheet','Sheet1');
%Read Excel raw data file using readtable function for Simulated Data
dataSimulated_ADS = readtable('CompareSimu.xlsx','Sheet','Sheet1');

%Get the Excel column Header1 and Header2 from Measured data
x_g_VNA = dataMeasured_VNA.Header1;
y_g_VNA = dataMeasured_VNA.Header2;
%Get the Excel column Header1 and Header2 from Simulated data
x_k_ADS = dataSimulated_ADS.Header1;
y_k_ADS = dataSimulated_ADS.Header2;

%Plot both Simulated and Measured data g vs k
i=plot(x_g_VNA,y_g_VNA,'b--o',x_k_ADS,y_k_ADS,'g');grid on
legend({'Measured','Simulated'},'Location','northeast','NumColumns',2);
i(1).LineWidth = 2;
i(2).LineWidth = 2;
xlabel('g [mm]', 'FontSize', 14);
%xlim([0.5 3.5]);
ylabel('k', 'FontSize', 14);
%ylim([0 0.45]);
set(gca, 'FontSize', 14);
figure;

%Plot both Simulated and Measured data g vs Lm
i=plot(x_g_VNA,y_g_VNA*18,'b--o',x_k_ADS,y_k_ADS*18,'g');grid on
legend({'Measured','Simulated'},'Location','northeast','NumColumns',2);
i(1).LineWidth = 2;
i(2).LineWidth = 2;
xlabel('g [mm]', 'FontSize', 14);
%xlim([0.5 3.5]);
ylabel('L_m [uH]', 'FontSize', 14);
%ylim([0 0.45]);
set(gca, 'FontSize', 14);
figure;
```

B.7 Data Processing MATLAB Script for Figures 4.20 and 4.21

```
% EE600 - Data processing script for comparing the separation distance g
% to the power transfer Efficiency [%] of both simulated and measured
% values. The script processes the data in Tables 4.1 and 4.3 for g and
% then for S21. Following this the S21 data is converted from dB to
% magnitude and scaled for efficiency. In addition to this, this script
% also compares the Loss [%] of both simulated and measured values from the
% insertion loss parameter, S11 over separation distance.

%Read Excel files using readtable function for simulated and measured
%S-parameters vs g.
dataMeasured_S21 = readtable('measured_S21.xlsx','Sheet','Sheet1');
dataMeasured_Lm = readtable('measured_Lm.xlsx','Sheet','Sheet1');

%Get the Excel column Header1 and Header2 from measured S21 and g
mea = dataMeasured_S21.Header1;
g_mea = dataMeasured_S21.Header2;
mea2 = dataMeasured_Lm.Header1;
Lm = dataMeasured_Lm.Header2;

%Convert from dB to magnitude then from magnitude to Efficiency
mag_mea = db2mag(mea);
Efficiency_mea = mag_mea*100;
mag_mea2 = db2mag(mea2);
Efficiency_Lm = mag_mea2*100;

%Plot both Simulated and Measured data for g vs power transfer Efficiency
s=plot(g_mea,Efficiency_mea,'r');grid on
%legend({'Measured'},'Location','northeast','NumColumns',2);
s(1).LineWidth = 2;
xlabel('g [mm]', 'FontSize', 14);
xlim([0.9 3.6]);
ylabel('Efficiency [%]', 'FontSize', 14);
ylim([0 100]);
set(gca, 'FontSize', 14);
figure;

s=plot(Lm,Efficiency_Lm,'b');grid on
%legend({'Measured'},'Location','northeast','NumColumns',2);
s(1).LineWidth = 2;
xlabel('L_m [\muH]', 'FontSize', 14);
xlim([3.5 7.5]);
ylabel('Efficiency [%]', 'FontSize', 14);
ylim([0 100]);
set(gca, 'FontSize', 14);
```

Appendix C – Distance & DC Voltage Measurements


1.798
PITTSBURGH

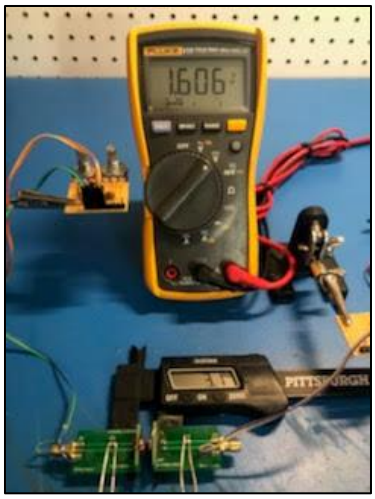
1.606
PITTSBURGH


1.274
PITTSBURGH

REFERENCES

[1] Chopra, Swagat, “Contactless Power Transfer for Electric Vehicle Charging Application”, Master of Science Thesis, Delft University of Technology, August 2011.

[2] Jawad AM, Nordin R, Gharghan SK, Jawad HM, Ismail M. Opportunities and Challenges for Near-Field Wireless Power Transfer: A Review. *Energies*. 2017; 10(7):1022. https://doi.org/10.3390/en10071022

[3] N Tesla. “Apparatus for transmitting electrical energy.” Ed: Goodle Patents. 1914.

[4] M. Rehman, Z. Baharudin, P. Nallagownden, B. J. I. J. o. E. E. Islam, and C. Science, "Modelling and EfficiencyAnalysis of Wireless Power Transfer using Magnetic Resonance Coupling," vol. 6, no. 3, pp. 563-571, 2017.

[5] (a) For iPhone 7 QI Wireless Charger Phone Case for iPhone 6s 6 Wireless Charging Receiver Back lip Protection Shell Case only Opp Bag. 2021 For IPhone 7 QI Wireless Charger Phone Case For IPhone 6s 6 Wireless Charging Receiver Back Lip Protection Shell Case Only Opp Bag From Soundmae, $6.27 | DHgate.Com**.** (b) Apple Watch Magnetic Charging Dock. Apple Watch Magnetic Charging Dock - Education - Apple (AU)**.** (c) Naztech Freedom+ TWS True Wireless Earbuds with Wireless Charging Pad – White, SKU: 1A-NAZTECH-FREEDOM-WHITE-46237. Naztech Freedom+ TWS True Wireless Earbuds with Wireless Charging Pad - White - HD Accessory

[6] S. Cem, M.A. de Rooij. *Trilogy of Wireless Power Transfer: Basic Principles, WPT Systems and Application*, Belmont, CA: Wadsworth, 1993 Swiridoff Verlag, Germany: Swiridoff Verlag, ISBN: 978-3-89929-371-5, 2019.

[7] (a) Wireless Car Charging Images, Stock Photos & Vectors | Shutterstock. (b) White electric car on EV wireless charging lane. The in-road wireless Stock Photo - Alamy

[8] A. K. Swain, M. J. Neath, U. K. Madawala and D. J. Thrimawithana, "A dynamic model for bi-directional Inductive Power Transfer systems," *IECON 2011 - 37th Annual Conference of the IEEE Industrial Electronics Society*, Melbourne, VIC, Australia, 2011, pp. 1024-1029, doi: 10.1109/IECON.2011.6119336.

[9] A. K. Swain, M. J. Neath, U. K. Madawala and D. J. Thrimawithana, "A Dynamic Multivariable State-Space Model for Bidirectional Inductive Power Transfer Systems," in *IEEE Transactions on Power Electronics*, vol. 27, no. 11, pp. 4772-4780, Nov. 2012, doi: 10.1109/TPEL.2012.2185712.

[10] L. Shi, Z. Yin, L. Jiang and Y. Li, "Advances in inductively coupled power transfer technology for rail transit," in *CES Transactions on Electrical Machines and Systems*, vol. 1, no. 4, pp. 383-396, December 2017, doi: 10.23919/TEMS.2017.8241360.

[11] T. Imura and Y. Hori, "Maximizing Air Gap and Efficiency of Magnetic Resonant Coupling for Wireless Power Transfer Using Equivalent Circuit and Neumann Formula," in *IEEE Transactions on Industrial Electronics*, vol. 58, no. 10, pp. 4746-4752, Oct. 2011, doi: 10.1109/TIE.2011.2112317.

[12] Rahman, Syed. (2014). Design and Construction of Wireless Power Transfer System Using Magnetic Resonant Coupling. American Journal of Electromagnetics and Applications. 2.11. 10.11648/j.ajea.20140202.11.

[13] S. Cheon, Y. Kim, S. Kang, M. L. Lee, J. Lee and T. Zyung, "Circuit-Model-Based Analysis of a Wireless Energy-Transfer System via Coupled Magnetic Resonances," in *IEEE Transactions on Industrial Electronics*, vol. 58, no. 7, pp. 2906-2914, July 2011, doi: 10.1109/TIE.2010.2072893.

[14] Jie Cheng, Dongqing Wang, "Research and analysis of frequency effect in magnetic resonance", *Chinese Automation Congress (CAC) 2017*, pp. 2579-2582, 2017.

[15] Mingbo Yang, Guodong Yang, En. Li, Zize Liang, Bo Zhai, "Topology and inductance analysis for wireless power transmission system", *Control and Decision Conference (CCDC) 2013 25th Chinese*, pp. 2052-2056, 2013.

[16] Wertheimer N, Leeper E. Electrical wiring configurations and childhood cancer. *American Journal of Epidemiology* 1979; 109(3):273-284.

[17] International Agency for Research on Cancer, World Health Organization. *IARC Classifies Radiofrequency Electromagnetic Fields as Possibly Carcinogenic to Humans*, May 31, 2011.

[18] Mohanty Satyajit, Regd. No-0901106207, www.slideshare.net

[19] Mroczkowski, Robert S, Electrical Connector Handbook, McGraw-Hill Professional, 1997, ISBN 13: 9780070414013.

[20] J. S. Benjestorf and X. Liu, "Non-mating connector for USB a quality waterproof connection," *2013 IEEE International Conference on Consumer Electronics (ICCE)*, Las Vegas, NV, 2013, pp. 560-563, doi: 10.1109/ICCE.2013.6487018.

[21] Triple Outlet Grounded Cub Electric Wall Power Adapter. https://www.alibaba.com/product-detail/TRIPLE-OUTLET-GROUNDED-CUBE-ELECTRIC-WALL_60408484226.html

[22] Apple Thunderbolt Cable (0.5 m) Part No. MD862ZM/A. https://cvp.com/product/apple_thunderbolt_cable-0.5m

[23] 30 cm PWM pin Y Splitter Computer PC Fan Power Cable, CakeYCN Part No. 10025 https://www.newegg.com/p/1B4-038E-00085

[24] USB 3.0 shielded I/O Receptacle Type-A, Molex Part No. 482580001.

[25] M. Braunovic, V.V. Konchits, N.K. Myshkin, “Introduction to Electrical Contacts,” in Electrical Contacts: *Fundamentals, Applications, and Technology*, 1st ed. Boca Raton, FL, USA: CRC Press, 2007, ch. 1, pp. 6.

[26] F. Zhang and G. T. Flowers, "Fretting corrosion in electric connectors induced by axial vibration," *2014 IEEE 60th Holm Conference on Electrical Contacts (Holm)*, New Orleans, LA, 2014, pp. 1-8.

[27] Fuxi Zhang, George T. Flowers, Robert N. Dean, Jeffrey Suhling, Jinchun Gao, "A study on axial vibration-induced fretting corrosion in electrical connector pair", *Electrical Contacts (Holm) 2016 IEEE 62nd Holm Conference on*, pp. 146-151, 2016.

[28] M. D. Bryant, "Resistance buildup in electrical connectors due to fretting corrosion of rough surfaces," *Proceedings of IEEE Holm Conference on Electrical Contacts*, Pittsburgh, PA, USA, 1993, pp. 178-190.

[29] J. Benjestorf, "A New Trend In Connectivity: Sharing content over multiple channels.," in *IEEE Consumer Electronics Magazine*, vol. 3, no. 1, pp. 25-31, Jan. 2014, doi: 10.1109/MCE.2013.2284938.

[30] J. S. Benjestorf, A. W. Morales and S. S. Agili, "Design and Analysis of Wireless Power Transfer for Non-Metallic USB Connector," *2020 IEEE International Conference on Consumer Electronics (ICCE)*, Las Vegas, NV, USA, 2020, pp. 1-6, doi: 10.1109/ICCE46568.2020.9042993.

[31] J.S. Benjestorf, “Non-Mating Connector,” U.S. Patent 9 197 292 B2, November 24, 2015.

[32] K. Wang and S. Sanders, "Contactless USB — A capacitive power and bidirectional data transfer system," *2014 IEEE Applied Power Electronics Conference and Exposition - APEC 2014*, Fort Worth, TX, USA, 2014, pp. 1342-1347, doi: 10.1109/APEC.2014.6803481.

[33] N. Zannat and P. D. Franzon, "Asymmetric Transformer Design With Multiband Frequency Response for Simultaneous Power and Data Transfer," in *IEEE Transactions on Components, Packaging and Manufacturing Technology*, vol. 10, no. 4, pp. 644-653, April 2020, doi: 10.1109/TCPMT.2020.2977045.

[34] Yu-Gang Su, Shi-Yun Xie, Aiguo Patrick Hu, Chun-Sen Tang, Wei Zhou, Liang Huang, "Capacitive Power Transfer System With a Mixed-Resonant Topology for Constant-Current Multiple-Pickup Applications", *Power Electronics IEEE Transactions on*, vol. 32, no. 11, pp. 8778-8786, 2017.

[35] E. Abramov, I. Zeltser and M. M. Peretz, "A network-based approach for modeling resonant capacitive wireless power transfer systems," in *CPSS Transactions on Power Electronics and Applications*, vol. 4, no. 1, pp. 19-29, March 2019, doi: 10.24295/CPSSTPEA.2019.00003.

[36] D.J. Griffiths, “Introduction to Electrodynamics,” in Electrical Contacts, 4th ed. Cambridge, UK: Cambridge University Press, 2017, ch. 7, pp. 322.

[37] Liu, Shuo; Su, Jianhui; Lai, Jidong. 2019. "Accurate Expressions of Mutual Inductance and Their Calculation of Archimedean Spiral Coils" *Energies* 12, no. 10: 2017. https://doi.org/10.3390/en12102017

[38] J.i. AAgbinya – Editor, Wireless Power Transfer, River Publishers Series in Communications, 9000 Aalborg Denemark (2021).

[39] A. Karalis, J. D. Joannopoulos, M. Soljacic “Efficient Wireless Non-Radiative Mid-Range Energy Transfer”, MIT (2006).

[40] J.S. Benjestorf, “Non-Metallic Connector for USB Receptacle Type-A and Flash Drive,” U.S. Patent Application No. 63/090,422 (Pending), October 12, 2020

[41] J.S. Benjestorf, “Non-Metallic Connection Light Bulb and Socket,” U.S. Patent Application No. 63/038,988 (Pending), June 15, 2020

[42] https://phys.org/news/2017-02-corrosion-solar-panels.html

[43] Karthikeyan, Prabhakar & Sanjeevikumar, P. & Blaabjerg, F. & Holm-Nielsen, Jens & Bhattacharya, Supratik. (2019). “A Review for Assessment on Solar Panel Degradation”.

[44] Chengqing Yuan, Conglin Dong, Liangliang Zhao and X. Yan, "Marine environmental damage effects of solar cell panel," *2010 Prognostics and System Health Management Conference*, 2010, pp. 1-5, doi: 10.1109/PHM.2010.5413495

[45] “How many satellites orbit Earth and why space traffic management is crucial”. [Online]. Available: https://www.geospatialworld.net/blogs/how-many-satellites-orbit-earth-and-why-space-traffic management-is-crucial/. [Published: 23-Aug-2020]

[46] “Important Facts about EVA (ethylene vinyl acetate) Film for Solar PV Panels - Power From Sunlight.” [Online]. Available: https://www.powerfromsunlight.com/important-facts-about-eva-ethylene-vinyl-acetate-film-for-solar-pvpanels/. [Accessed: 03-Mar-2019].

[47] H. Votsi, C. Matei, S. Iezekiel and P. H. Aaen, "Active Interferometry-Based Vector Network Analyzer Reference Impedance Renormalization," *2020 95th ARFTG Microwave Measurement Conference (ARFTG)*, 2020, pp. 1-3, doi: 10.1109/ARFTG47271.2020.9241364.

[48] H. Happy, K. Haddadi, D. Theron, T. Lasri and G. Dambrine, "Measurement techniques for RF nanoelectronic devices: new equipment to overcome the problems of impedance and scale mismatch", *IEEE Microw. Mag.*, vol. 15, no. 1, pp. 30-39, Jan. 2014.

[49] F. Mubarak, R. Romano and M. Spirito, "Evaluation and modeling of measurement resolution of a vector network analyzer for extreme impedance measurements," *2015 86th ARFTG Microwave Measurement Conference*, 2015, pp. 1-3, doi: 10.1109/ARFTG.2015.7381475.